Design, Construction, and Validation of an In-Cylinder Pressure Recording System for Internal Combustion Engine Analysis

By

Michael Dewaine Mangus

Submitted to the graduate degree program in Mechanical Engineering and the Graduate Faculty of the University of Kansas in partial fulfillment of the requirements for the degree of Master of Science.

Chair: Dr. Christopher Depcik

Dr. Bedru Yimer

Dr. Edward Peltier

Defended: March 1st, 2012

The Thesis Committee for Michael Mangus certifies that this is the approved version of the following thesis:

Design, Construction, and Validation of an In-Cylinder Pressure Recording System for Internal Combustion Engine Analysis

By

Michael Dewaine Mangus

_____

Chair: Dr. Christopher Depcik

_____

Acceptance Date

Abstract

Due to an increased global interest in sustainable energy sources, it is imperative that the transportation sector find substitutes for the limited petroleum supply, such as biodiesel. This thesis contains three sections detailing the construction of a biodiesel engine testing system intended for biodiesel and engine technology research. Chapter one details the initial construction of the biodiesel test cell. In addition, the limitations of the system are individually pointed out, with solutions to these limitations discussed. Finally, the focus of this thesis is included to set the scope of the work discussed in chapters two and three.

In chapter two, a biodiesel study was completed in order to investigate changes in engine performance because of the differences in fuel properties derived from various feedstock oils. The goal of this investigation was to determine which biodiesel fuel properties impact engine emissions and fuel consumption in comparison to petroleum-based diesel. The findings indicate good agreement with published works and resulted in correlations for fuel properties that were not discussed in literature.

In chapter three, the design, construction, and validation of an engine cylinder pressure recording system are covered. In particular, the discussion includes the equipment selection, machining of the engine head and encoder adapter, writing of a LabVIEW program to record pressure and crank angle data, and the validation of this system. Validation was accomplished by testing three different fuels with very different combustion characteristics and directly comparing the results to literature trends and fundamental engine performance characteristics.

Table of Contents

Table of Figures

Table of Tables

Nomenclature

Variable	Description	Units
B	Engine Cylinder Bore	(m)
$IMEP_g$	Gross Indicated Mean Effective Pressure	(bar)
l_{cr}	Engine Connecting Rod Length	(m)
m_f	Mass of Fuel Injected	(g)
$\dot{m}$	Mass Flow Rate	(g/s)
N	Engine Speed	(rotations/minute)
n	Polytropic Index	(-)
n_r	Crank Revolutions per Power Stroke	2 (4-stroke)
P	Engine Brake Power	(kW)
$P_{i,g}$	Gross Indicated Power	(kW)
p	Pressure	(bar)
p_1	Pressure at a known crank angle	(bar)
p_2	Pressure at a different crank angle later in cycle than p_1	(bar)
p_{off}	Offset Pressure	(bar)
$pmep$	Pumping Mean Effective Pressure	(bar)
Q_{ch}	Gross Heat-Release	(kJ)
Q_{lhv}	Fuel Lower Heating Value	(kJ/kg)
Q_n	Net Heat-Release	(kJ)
r_c	Engine Crank Radius	(m)
T	Engine Torque	(N-m)
V	Cylinder Volume	(m^3)
V_c	Engine Cylinder Clearance Volume	(m^3)
V_d	Engine Displacement Volume	(m^3)
W_b	Engine Brake Work	(kJ/cycle)

$W_{i,g}$	Indicated Gross Work	(kJ/cycle)
$W_{i,n}$	Indicated Net Work	(kJ/cycle)
W_p	Indicated Pumping Work	(kJ/cycle)
γ	Ratio of Specific Heats	(-)
θ	Engine Crank Angle	(º)
η_c	Combustion Efficiency	(%)
η_f	Fuel Conversion Efficiency	(%)
η_m	Mechanical Efficiency	(%)
η_t	Thermal Conversion Efficiency	(%)
Subscripts		
$_f$	Fuel	
$_j$	Exhaust Species	

1.1 Introduction

Due to an increased global interest in sustainable energy sources, it is imperative that the transportation sector find substitutes for the limited petroleum supply. This will likely come in several forms, one of which is biofuels. Specifically, research involving biodiesel is especially promising. Biodiesel can be created from many different sources and can be engineered to provide similar performance to petroleum-based diesel. In addition, engines currently produced to run on petroleum-based diesel have the ability to operate using biodiesel without any modification to the engine design. Furthermore, biodiesel transportation and storage is possible using existing technologies like rail, truck and barges. However, special considerations must be made to do so as biodiesel is hydrophilic; meaning that water readily mixes with it. With winterization to prevent solidification in cold temperatures, users in many different climates are currently using biodiesel [6, 7]. The use of biodiesel for transportation presents a sustainable solution that has many advantages over other energy sources. However, like many of the other future energy sources, biodiesel has its own obstacles to overcome. Specifically, the biodiesel industry must ensure availability for an ever-increasing demand, not compete with food supply or production, and meet stringent economic and environmental requirements.

Currently, the global oil consumption is about 86 million barrels per day with predicted increases of up to 110.6 million barrels per day in 2035 [8]. Of this usage, the Unites States accounts for approximately 25%, or about 22 million barrels per day [9]. This energy usage will eventually need to be replaced with sustainable sources. In 2009, only about 104 million barrels total of biodiesel were produced, up 9% from the previous year [10]. As biodiesel production continues to grow, the land area used to grow biodiesel feedstocks must also increase. This leads a competition for available acreage with food production. Due to this relationship, it is necessary for biodiesel energy production to be relatively dense on a per-acre basis in order to leave adequate opportunity to grow food crops. Currently, first generation biodiesel feedstocks such as soybean oil, rapeseed oil, palm seed oil, and

canola oil can only generate between 50-600 gallons (1-2 barrels) per acre annually, depending on the feedstock [11]. The total global vegetable oil production (including food usage) is estimated to be about 27 billion gallons annually, or roughly 81% of U.S. on-highway diesel fuel use [9]. Due to this finding, the next generation of biodiesels, such as biodiesel created from algae, must produce more biodiesel per acre. Preliminary estimates for algal biodiesel indicate a production of 9,600 barrels per acre annually, greatly reducing the required land area needed to effectively supply energy on a large scale [11].

Along with the economic and ethical requirements for biodiesel, environmental obstacles are present [9, 12, 13]. Biodiesel is inherently non-toxic and biodegradable as a liquid. However, engines running this fuel have to adhere to the same emissions requirements as any other diesel engine in use. In particular, biodiesel engines must have low emissions of nitrogen oxides (NO_x) among other chemical species such as carbon monoxide (CO) and Particulate Matter (PM). Regulation of these emissions began in 1968 with gradual lowering of emissions until the institution of Tier 0 regulations, where emissions were lowered for all engines built from 1988-1993. For example, light-duty truck (up to 3750 pounds when loaded) NO_x emissions were lowered from 3.6 grams per mile (pre-1968 levels) to 1.2 grams per mile. For all vehicles built between 1994 and 2003, Tier 1 regulations further lowered NO_x, CO, and PM emissions. Finally, vehicles produced after 2004 are subject to Tier 2 regulations that limit NO_x emissions to their current levels. The NO_x emissions for all vehicles now built must be lower than 0.2 grams per mile, indicating a significant reduction in emissions compared to pre-regulated levels [14]. Currently, these harmful gas species are controlled using various engine operation techniques, as well as sophisticated exhaust aftertreatment devices. As engine manufacturers meet ever-lowering emission regulations, biodiesel must not interfere with the current and future exhaust control methods. Due to the potential of biodiesel and the advancements yet to be made in both production and operation, it is worthwhile for universities to devote resources to this field. For the Mechanical Engineering

department at the University of Kansas (KU), this required the construction of a biodiesel test cell in order to examine the biodiesel produced by the chemical and petroleum engineering department.

1.2 Single Cylinder Engine Test Cell and Prior Efforts

The engine selected for biodiesel testing at KU is a Yanmar L100V single-cylinder, direct-injection diesel engine originally packaged with an Alternating Current (AC) electric generator. The engine is connected by driveshaft to a NorthStar AC electric generator and to provide load (energy draw) on the engine, resistance through heating elements occurs through the generator outlets. As load is added, the resulting torque is measured using a Futek (model #TRS605) transducer connected to the driveshaft between the engine and generator. Since fuel flow is a critical parameter for determining engine fuel consumption and because this component is significantly important for biodiesel research, high accuracy is preferred. As a result, a Micro-Motion Coriolis fuel flow meter (model #CMF010M) is used to measure the Yanmar fuel consumption. To measure the engine intake airflow, a laminar flow element (model #50MW20) is located in-line with the intake stream. Measuring the pressure drop across the element yields the volumetric flow rate of the engine. The aforementioned sensors, along with ambient, intake, and exhaust temperatures and pressures are indicated and recorded using a National Instruments (NI) compact-Reconfigurable Input/Output (cRIO) device (model #cRIO-9014) operating in conjunction with a LabVIEW program designed and coded in-house. This system is simple and robust while offering the ability to make modifications quickly with subsequent straightforward control. As an added benefit, use of a single cylinder engine allows for testing smaller biodiesel batches in comparison to a multi-cylinder counterpart making the system more economical to operate. In addition, the trends observed during testing of this single cylinder engine are directly scalable to larger engines, but do not have the complex characteristics and fluid dynamics variability of multi-cylinder engines.

This single cylinder test cell is currently being used for several research endeavors. Specifically, the first study performed using the test cell injected hydrogen and carbon monoxide into the intake air

stream of the diesel engine in order to enhance biodiesel combustion [15]. This research was intended to augment other engine research at KU using the co-product glycerin from the KU Biodiesel Institute as a potential fuel for electrical generation by first reforming the liquid into a gaseous mixture of hydrogen and carbon monoxide. Results indicated improved thermal efficiency during combustion with reduced biodiesel fuel consumption. Another topic currently being studied is the impact of injecting ozone into the intake air stream of a diesel engine with results pending. Moreover, in line with this thesis, the first experiments with different biodiesel fuels investigating how varying feedstock properties affect the performance and emissions of the engine have been completed. In this study, seven different vegetable oils with different degrees of molecular saturation, density, and viscosity were directly compared with Ultra-Low-Sulfur-Diesel (ULSD) in order to examine how these properties altered fuel consumption and exhaust emissions. It was found that strong correlations between molecular structure and fuel performance do exist. This finding is helpful in the search for a biodiesel that performs similarly to ULSD while paving the way for additional biodiesel research involving new fuels and associated blends. This biodiesel study is the focus of the second chapter of this work.

1.3 Yanmar Limitations

It is important to note that the Yanmar engine does include limitations that currently make direct comparison with larger production engines more difficult. Multiple mechanical engineering graduate students, in the order of potential impact on research, are individually addressing each limitation. These restrictions will be discussed in the next few paragraphs in order to provide context for the reader. This will lead into the efforts of the author building on the past biodiesel research in order to obtain a better understanding moving forward.

First, the Yanmar's direct injection system is currently controlled by a mechanical fuel pump and governor, rather than by an electronic system. This limits the operating speed at 3600 rotations per minute (RPM) in order to match the intended 60 Hz electricity generation of the NorthStar AC

generator. Moreover, this injection system feeds diesel into the engine at 2850psi; a much lower pressure than production systems that can be in excess of 20,000 psi. Due to this limitation, researchers cannot control the speed or injection characteristics of the engine, removing the opportunity to study engine performance at multiple speeds and injection strategies. Dr. Christopher Depcik, the advisor of the author, is currently addressing this issue through communications with a pump and injector supplier in order to upgrade the system to a modern rail pressure system.

Furthermore, production engines utilize Exhaust Gas Recirculation (EGR) in order to partially mitigate NO_x emissions. This occurs through recycling the inert exhaust gas that acts as a heat sink during combustion reducing the temperatures and pressures seen within the cylinder. This effectively lowers the amount of NO_x that forms via dissociation under high temperatures [1]. While the stock Yanmar does have an EGR passage in its cylinder head, this system is not dynamically adjustable like its larger production engine counterparts. This limitation again hinders the current research opportunities at KU. To improve testing accuracy, the Yanmar engine's EGR port has been blocked in order to allow an external EGR system to be installed. In the planned system, exhaust will be plumbed through a cooler and control valve to the intake tube. This improved apparatus will provide tremendous flexibility as both EGR flow rate and temperature will be controllable, providing the opportunity for future engine performance studies.

Other differences between the Yanmar engine and current on-highway diesel engines are that the Yanmar is naturally aspirated and air-cooled, rather than turbocharged and liquid-cooled. Because of these differences, the Yanmar will operate differently than a production engine with lower efficiencies due to its natural aspiration intake (a turbocharger uses waste exhaust energy to increase intake pressures) and lack of a cooling jacket to modulate heat loss from the cylinder. Though it is not feasible to upgrade to a liquid-cooling system, plans are in place to install a turbocharger following completion of the installation of the new engine dynamometer as discussed in the next paragraph. A

turbocharger company has been located that has provided the appropriate turbocharger for the Yanmar engine. Following installation and subsequent testing, data recorded with regards to turbocharger performance will be shared with this local company.

As mentioned prior, the engine is loaded using electrical resistance connected to an AC generator. This is a non-traditional engine testing method necessary due to initial facility limitations at KU. As such, it is possible to achieve steady-state loading that is repeatable, but it is difficult to perform transient loading that is critical in gaining a complete understanding of engine performance. To solve this problem, a dynamometer is being installed to improve engine loading capabilities. The chosen dynamometer is an alternating current dynamometer and will allow dynamic control of load and speed. The dynamometer is a DyneSystems, Inc. Dymond Series 12 horsepower air cooled regenerative AC dynamometer with a maximum speed and torque of 7500 RPM and 28.6 N-m, respectively. The dynamometer is controlled by a DyneSystems, Inc. Inter-Loc V OCS. Finally, to aid in combustion studies, the dynamometer will be able to both motor and load the engine. Motoring the engine means that the dynamometer applies power to the engine to turn it without fuel or combustion taking place in the engine. Data taken during this type of operation yields information regarding the energy needed to move gasses into and out of the engine cylinder and the frictional losses that the engine must be overcome to create power. Loading the engine simulates additional power requirements of a mechanical load being applied to the engine during normal operation in a real-world environment, such as powering a generator, transferring power to the wheels of a vehicle, etc. Changing engine loading drastically affects engine power, efficiency, fuel consumption, and emissions and therefore must be changed to get a full understanding of engine operation.

Research on engine performance is greatly enhanced with a more-complete understanding of the combustion process. This is accomplished by using an in-cylinder pressure transducer synchronized to a crankshaft-angle encoder installed on the engine [1, 16-18]. The encoder and transducer system

allows researchers to monitor the change in cylinder pressures with respect to other phases in the engine cycle or changes in operation according to load or fuel type. In particular, a pressure trace can be used to determine the start of fuel injection, the delay from injection to the start of combustion, and the rate of heat release as combustion occurs [18]. The design, installation, and initial testing of this transducer/encoder system is the focus of the third chapter of this work.

1.4 Thesis Focus

As briefly discussed, a biodiesel fuel study was completed in order to investigate changes in engine performance because of the difference in the fuel properties derived from various feedstock oils. The goal of this investigation was to determine which biodiesel fuel properties impact engine emissions and fuel consumption in comparison to petroleum-based diesel. This study was first discussed in the thesis by Cecrle where the automation of the diesel engine test cell was also described [15]. This automation proved to be vital to the completion of the biodiesel performance and emission testing. Chapter 2 contains the completed version of the biodiesel study as submitted for publication. Multiple authors were involved in the completion of this paper, and each contributed critical efforts that ensured the project's success. Specifically, Eric Cecrle installed and tested the data collection and controls system. Dr. Christopher Depcik helped determine the biodiesel test strategy, secured project funding while reviewing and editing versions of the paper. Andrew Duncan produced each biodiesel batch and provided critical measurements of each biodiesel's property. Jing Guo and Yue Zhong performed measurement of gas and particulate matter emissions. Dr. Edward Peltier explained emission results, provided the emissions analysis equipment, and performed significant editing and reorganizing of the abstract, introduction, and discussion section of the paper preceding the resubmission of this paper. Dr. Susan Stagg-Williams reviewed the paper and oversaw production of the biodiesel batches. Michael Mangus completed the performance testing of all biodiesel fuels in the test cell, analyzed and compiled

the fuel consumption and emissions data while researching the literature and writing the majority of the paper.

During the biodiesel testing and subsequent writing of the findings, it was determined that the instrumentation installed in the biodiesel test cell only can provide insight into the effects of macroscopic trends, such as increases and decreases in fuel consumption and gas emissions. However, it was not possible to describe how some fuel properties were directly contributing to these effects. Specifically, the impacts of the fuel on injection timing and ignition delay cannot be determined without an understanding of the combustion process inside the engine cylinder. In order to obtain this knowledge, it is necessary to measure the engine cylinder pressure while simultaneously measuring the engine crank angle. With this data, it is possible to determine when the injection of fuel occurs, how long it takes the fuel to ignite following injection (ignition delay), and when the fuel chemical energy is released during combustion.

In chapter three, the design, construction, and validation of the system are covered. In particular, the discussion includes the equipment selection based on expected demands, machining of the engine head and encoder adapter, writing of a LabVIEW program to record pressure and crank angle data, and the validation of this system. Validation was accomplished by testing three different fuels that have different combustion characteristics. Machining of the engine head and encoder were completed by the KU Mechanical Engineering machine shop based on designs by Michael Mangus. Measurement of the engine emissions was performed with the help of Yue Zhong, who calibrated and set up the emissions analysis equipment prior to fuel testing.

CHAPTER 2: An Investigation of the Effects of Biodiesel Feedstock on the Performance and Emissions of a Single-Cylinder Diesel Engine

Eric Cecrle[1], Christopher Depcik[1], Andrew Duncan[2], Jing Guo[3], Michael Mangus*[1], Edward Peltier[3], Susan Stagg-Williams[2], Yue Zhong[3]

[1] University of Kansas, Department of Mechanical Engineering

[2] University of Kansas, Department of Chemical and Petroleum Engineering

[3] University of Kansas, Department of Civil, Environmental and Architectural Engineering

1530 W. 15th Street, Lawrence, KS 66045-4709

* Corresponding author: mmangus@ku.edu

2.1 Abstract

Biodiesel fuels may serve as a partial solution in the search for sustainable energy sources for the transportation sector. However, increased nitrogen oxide (NO_x) emissions are a potentially significant drawback to the use of biodiesel fuels that must be addressed if biodiesel is to gain widespread acceptance. One approach is to identify specific biodiesel fuel properties that minimize NO_x formation and use these to produce lower NO_x fuel blends. In this work, seven biodiesel fuels were produced from high-erucic rapeseed, olive, palm, coconut, soybean, and fresh and used canola oils with their chemical composition determined using Gas Chromatography–Mass Spectrometry (GC-MS). The fuels were then burned in a single-cylinder direct-injection diesel engine and evaluated for both fuel consumption and exhaust emissions of nitrogen oxides, carbon monoxide (CO), unburned hydrocarbons and particulate matter. While all biodiesels had higher brake-specific nitric oxide (NO) emissions than ultra-low sulfur diesel (ULSD) at low engine loads, olive, palm, coconut and canola biodiesels performed better than ULSD at 50% loading and above. Nitrogen dioxide (NO_2), CO and unburned hydrocarbon emissions were generally lower from the biodiesel fuels than ULSD. Palm biodiesel consistently generated the lowest brake-specific NO_x levels of all tested fuels. Statistical analysis of the results

showed that higher fuel hydrogen:carbon molar ratios, low poly-unsaturation levels, and lower fuel density were all significantly associated with reduced NO emissions in the tested biodiesel fuels, but no clear trends were observed for NO_2. The results suggest that pathways exist for tailoring the fuel properties of biodiesel blends to reduce nitrogen oxide emission as compared to current fuels.

2.2 Introduction

Most of the energy used in the transportation sector is in the form of liquid fuels, primarily gasoline and diesel[7]. Current estimates indicate that the world liquid fuel consumption will increase from 86.1 million barrels per day to 110.6 million barrels per day in 2035[7]. At this rate, the transportation sector is projected to account for more than 60% of total liquid fuel usage in 2035, up from its current level of 46%[7]. This will increasingly strain the available sources of petroleum. In order to address this issue, the transportation sector requires practical and sustainable sources of renewable supplies that can supplement or replace today's petroleum-based fuels.

Researchers have shown that compression ignition engines that burn diesel fuel can be operated successfully using fuels derived from renewable sources, or biodiesel[17, 19]. Biodiesel production typically occurs through the conversion of feedstocks, such as vegetable oils or animal fats, into mono-alkyl esters of long chain fatty acids using methanol or ethanol catalysis. Biodiesel fuels derived in this manner show significant promise as replacement fuels because they do not require any engine hardware modifications while retaining similar energy content to diesel[19-21]. However, these fuels must still demonstrate similar performance in engines as petroleum-based diesel with respect to engine power, fuel consumption, and emissions of regulated pollutants if they are to achieve widespread acceptance as substitute fuels.

The use of biodiesel typically results in decreased emissions of unburned hydrocarbons (HC), carbon monoxide (CO), and particulate matter (PM), but nitrogen oxide (NO_x) emissions often increase with biodiesel usage[2, 9, 12, 17, 19, 21-27]. In a comprehensive study of published research on

biodiesel emissions, the U.S. EPA estimated an average 10% increase in NO_x emissions for a pure (100%) biodiesel fuel compared to conventional diesel fuels[28]. This increase is a significant limitation from an air quality standpoint, as nitrogen oxides have noteworthy negative environmental and health effects, including contributing to the creation of photochemical smog and acid rain[29]. Previous research on biodiesel combustion has suggested that there may not be a single culprit for this increase, but rather several factors that contribute to improved conditions for formation of nitrogen oxide species [4, 17, 30]. The most likely major contributors to biodiesel NO_x increases are advanced injection timing, prompt NO_x formation, and changes in fuel composition that affect fuel spray or ignition patterns within the combustion chamber. Another possible factor is that the lower rate of particulate matter formation from biodiesel can reduce radiant heat losses in the cylinder and potentially increase flame temperature and thermal NO production [4, 17]. However, as discussed by Graboski and McCormick, particulate matter reductions and NO_x increase are not coupled for all fuels, so this mechanism is considered less likely [4].

In addition, biodiesel can affect combustion performance in pump-line-nozzle systems due to changes in fuel injection timing. Biodiesel fuel has a higher bulk modulus of compressibility than diesel fuel. This causes pressure waves in an engine's fuel line to move more rapidly in biodiesel[3, 17, 21, 24, 31]. Therefore, the fuel injector will open earlier in the engine cycle when it is injecting biodiesel, with an injection advance of 1-3 crank angle degrees for pure biodiesel fuels[24, 30]. This injection advance leads to earlier combustion and subsequent longer residence time at high temperatures, thereby increasing thermal NO formation[3, 17, 24]. Several studies have directly linked increased NO_x emissions to earlier injection times [31, 32]. Work by Ye and Boehman indicates that when injection timing is similar between ULSD and biodiesel, comparable combustion phasing and residence time occurs between the fuels[27]. To note, high-pressure common rail injection systems do not see an

injection timing advance when biodiesel is used, while some NO_x increase still occurs in these systems[24, 30].

The increase in biodiesel NO_x emissions may also be directly related to the fuel's chemical structure. In particular, McCormick et al. found that increasing the number of double bonds increased NO_x emissions across a range of biodiesel fuels[2]. Moreover, while thermal NO formation is not strongly affected by fuel chemistry, prompt NO formation may be sensitive to the formation of hydrocarbon radicals from unsaturated hydrocarbon compounds during combustion[4]. In several studies of biodiesel surrogate compounds[33, 34], Garner and co-workers observed increased levels of acetylene from the combustion of unsaturated hydrocarbon compounds, consistent with increased prompt NO formation. The chemical composition of the fuel will also directly affect properties such as fuel density, viscosity and cetane number (CN) that can have a range of effects on NO_x formation.

While engine power generated during the combustion of biodiesel remains comparable to that of diesel operation in most cases, published research has demonstrated that fuel consumption of pure biodiesel tends to increase by up to 12% due to biodiesel's lower energy content and higher density[25, 27]. This fuel consumption penalty is partially offset by biodiesel's often higher cetane number [9, 35]. The cetane number is a dimensionless number that defines the ignition delay of a particular fuel; e.g., a fuel with a high CN will have a shorter ignition delay than a fuel with a lower CN[36]. The higher CN of biodiesel fuels will result in earlier ignition, higher in-cylinder temperatures, and improved combustion efficiency, as long as the CN is not excessively high[9]. Hence, a higher cetane number can move forward the start of combustion for biodiesel fuels in both pump-line nozzle and common-rail systems[3], allowing for increased thermal NO formation[1]. However, additional research has found that, when separating out combustion timing effects, an increased CN can actually cause a decrease in NO_x emissions[2, 4, 5]. This phenomenon is likely a result of the inverse relationship between cetane number and unsaturation, with the latter being shown to increase NO_x [2]. Finally, the presence of

oxygen in biodiesel fuels results in greater heat release during the premixed phase of combustion, as the extra oxygen helps the higher hydrocarbons break down faster promoting mixtures that are closer to stoichiometric in auto-ignition zones[17, 27]. This leads to a hotter combustion process and is considered to be the major contribution to increased biodiesel NO_x by Ye and Boehman[27].

Research by McCormick et al. indicates that cetane number and unsaturation extent are critical properties that change engine emission levels when compared to conventional diesel through their modification to the specific amounts of premixed and diffusion burn phases. In particular, their results show that increasing biodiesel CN and saturation levels leads to lower NO_x emissions when injection timing is not impacted[2]. The unique characteristics of the individual fatty acid chains making up a given biodiesel fuel, particularly their saturation, branching, and chain length, will affect the fuel's CN[2, 23]. However, these parameters do not appear to affect other factors such as PM emissions and fuel consumption[2, 12].

While it is possible to mitigate NO_x emissions in a diesel engine using aftertreatment devices and the addition of Exhaust Gas Recirculation (EGR), these efforts are costly and require precise engine control to be successful[13, 37]. Similarly, while changing engine timing can reduce or eliminate the effect of biodiesel on NO_x emissions, this option is not practical for conditions where consumers are alternating between different fuel blends in the same engine. One alternative approach is to determine the fuel properties that will help reduce or eliminate increased NO_x emissions and then attempt to produce biodiesel fuels or fuel blends with these characteristics. In this work, we examine the chemical composition and combustion performance of biodiesel fuels produced from seven different feedstocks in order to better understand the relationship between fuel composition and nitrogen oxide emissions. In particular, we investigate the direct effect of varying degrees of mono and poly-unsaturation, as well as total unsaturation level, to determine whether the presence of multiple double bonds have an increased effect on emissions levels.

2.3 Experimental Section

The feedstock oils used for biodiesel production in this experiment were high-erucic acid rapeseed, olive, palm, coconut, and soybean oils, as well as both fresh and used canola oil. The used canola oil was waste cooking oil recovered from the University of Kansas dining facilities. These feedstocks were chosen to represent a range of fuel compositions with respect to ratios of saturated to unsaturated and mono-unsaturated to poly-unsaturated fats. Each vegetable-oil-feedstock was mixed with a 6:1 molar ratio of methanol to oil with a 1% by mass sodium methoxide catalyst. The oil, methanol, and catalyst were reacted for four hours with mechanical stirring in a batch reactor with an initial temperature of 333.15K. The resulting biodiesel and glycerol mixture was allowed to separate for a minimum of 12 hours, after which the denser glycerol layer was removed. The biodiesel was then washed three times in order to remove soaps, methanol, and impurities. Finally, water was removed by spray drying the fuel for a period of four hours. Approximately eight gallons of biodiesel were produced in each batch run.

The composition of each biodiesel fuel was determined using an Agilent 6890 Series GC system and a 5973 Network Mass Selective Detector and with MSD ChemStation Data Analysis Application software. The GC was equipped with an Agilent (model 19091N-231 HP-INNOWax) polyethylene glycol capillary column, capable of separating out methyl esters ranging from methyl hexanoate (C6:0) to lignoceric methyl ester (C24:0). Peaks were confirmed by comparison with FAME C6 standard (PN#21599-1mL-F from Sigma-Aldrich), and FAME C8-C24 standards (#18918-1AMP, from Supelco). Ethyl stearate (PN# S8269-56 from Sigma-Aldrich) was used as an internal standard for quantifying the methyl ester composition. The resulting composition data, including saturation and mono to poly-unsaturation percentages are all depicted in Table 1. All relative standard deviations were less than 4%, giving an error of $\pm$ 0.4% for a component comprising 10% of the total mass.

Table 2. Biodiesel fatty acid component mass fractions

Component	Used Cooking Oil	Rapeseed Oil[1]	Olive Oil	Palm Oil	Coconut Oil	Soybean Oil	Canola Oil
C6:0	-	-	-	-	1.8%	-	-
C8:0	-	-	-	-	9.2%	-	-
C10:0	0.7%	0.9%	0.5%	0.7%	6.5%	-	-
C12:0	-	-	-	0.8%	50.0%	-	-
C14:0	-	-	-	1.2%	18.5%	-	-
C16:0	6.8%	3.0%	8.7%	44.0%	7.5%	10.4%	4.1%
C18:0	1.6%	0.7%	2.5%	2.9%	1.1%	3.9%	1.6%
C18:1	57.7%	14.5%	73.6%	42.7%	5.2%	22.8%	60.6%
C18:1 trans	-	1.5%	-	-	-	1.6%	3.9%
C18:2	27.2%	11.8%	14.4%	7.6%	-	54.3%	21.2%
C18:3	5.8%	10.2%	-	-	-	6.5%	8.1%
C20:1	-	6.3%	-	-	-	-	-
C22:1	-	51.2%	-	-	-	-	-
Unsaturation	90.9%	95.4%	88.3%	50.4%	5.2%	85.3%	93.9%
Mono-Unsaturation	57.9%	73.4%	73.9%	42.7%	5.2%	24.5%	64.6%
Poly-Unsaturation	33.0%	22.0%	14.4%	7.6%	0.0%	60.8%	29.3%

Physical and chemical properties of the seven biodiesel fuels and the ULSD fuel used in the emissions tests can be found in Table 2. A sample of each fuel was sent to an external testing laboratory for elemental analysis of carbon, hydrogen and nitrogen content, and the oxygen content of each fuel determined by difference. Molar hydrogen:carbon (H:C) ratios were calculated from the fatty acid mass fractions in Table 1, while the cetane number was determined for each biodiesel using a weighted average of the individual fatty acid CNs found in the biodiesel[36, 38-40]. Since it was not possible to obtain the CN for ULSD used in this study, the ASTM International standard for diesel was used instead[41]. It is important to note that the rapeseed oil biodiesel did not pass ASTM D6584-10a used to measure glycerol content in the fuel. As a result, this fuel was not included in the analysis described in the discussion section.

[1] Note that the rapeseed oil biodiesel did not pass ASTM D6584-10a used to measure glycerol content in the fuel. As a result, this fuel was not included in the analysis described in the discussion section; however, it does provide some insight into energy content and viscosity that are observed to be important factors of fuel performance.

Table 2. Properties of produced biodiesels and ULSD

	ULSD	Used Cooking Oil	Rapeseed Oil	Olive Oil	Palm Oil	Coconut Oil	Soybean Oil	Canola Oil
Cetane Number	40.0	52.8±4.1	77.4±4.6	58.2 ±3.3	65.2 ±4.9	59.3±6.9	48.1±4.7	52.9±3.8
Energy Content (kJ/kg)	45494 ±44	39663 ±44	40352 ±44	39550 ±44	39825 ±44	38228 ±44	39880 ±44	39869 ±44
Density (298.15K) (kg/m^3)	839.60 ±0.01	882.69 ±0.01	877.43 ±0.01	870.03 ±0.01	866.26 ±0.01	865.52 ±0.01	875.58 ±0.01	874.08 ±0.01
Kinematic Viscosity (cSt)	2.481 ±0.001	6.560 ±0.001	8.189 ±0.013	4.644 ±0.002	4.643 ±0.001	2.720 ±0.002	4.218 ±0.001	4.625 ±0.002
Dynamic Viscosity (cP)	2.083 ±0.001	5.790 ±0.001	7.185 ±0.012	4.040 ±0.002	4.022 ±0.001	2.354 ±0.002	3.693 ±0.001	4.042 ±0.002
Oxygen Content (%wt.)	0.9% ±0.3%	10.5% ±0.3%	9.4% ±0.3%	10.4% ±0.3%	11.1% ±0.3%	14.4% ±0.3%	9.9% ±0.3%	9.6% ±0.3%
H:C Molar Ratio	1.80 ±0.04	1.84 ±0.04	1.89 ±0.04	1.88 ±0.04	1.96 ±0.04	2.01 ±0.04	1.87 ±0.04	1.87 ±0.04

However, the rapeseed biodiesel's emissions and performance parameters are displayed in order to indicate how an engine performs when a fuel with excess glycerol is used. Investigation of the rapeseed biodiesel properties indicates a difference in energy content and viscosity that are observed to be important factors of fuel performance and are discussed later in this work.

2.4 Combustion and Emissions Testing

The performance and exhaust emissions of the seven biodiesel fuels, along with Ultra Low Sulfur Diesel (ULSD) were examined in a single-cylinder diesel engine located at the University of Kansas. The engine was a Yanmar L100V direct-injected diesel engine (see Table 3) that uses a mechanical fuel pump-line-injector in order to maintain a constant engine speed of 3600 rotations per minute (RPM) similar to the engines used by Szybist[31] and by Boehman[3].

Table 3. Engine and Generator Specifications

Engine	Value
Manufacturer and Model	Yanmar L100V
Type	Vertical Direct-Injection Compression Ignition
Engine Intake	Naturally Aspirated
Cooling	Air-Cooled
Cycle	4-Stroke
Displacement	435 cc
Number of Cylinders	1
Number of Valves	1 Intake, 1 Exhaust
Bore	86mm
Stroke	75mm
Compression Ratio	21.2
Injection Timing	15.5 (+/- 0.5) degrees BTDC
Continuous Rated Output	8.3 hp SAE
	6.2 kW
Rated Speed	3600 RPM
Injector Pressure	19.6 MPa
Aftertreatment	None
Engine Oil Used	Shell 15W-40
Generator	
Manufacturer and Model	NorthStar 5500BDG
Maximum Output	5500 W
Continuous Output	5000 W
Voltage	120/240 V
Phase	Single-phase (4-wire)
Frequency	59.0-62.0 Hz
Power Factor	100%
Allowable Current (120V/240V)	2@20 Amp/ 1@20 Amp

For the L100V, injection occurs at 15.5±0.5º before piston top-dead-center with a pressure of 19.6MPa. In order to provide load on the engine, the setup employs a NorthStar electric generator coupled to the crankshaft (Table 3). Resistance heaters supplied variable electrical loading during the combustion tests. This setup provides a repeatable, economic alternative to a full-scale engine dynamometer while using relatively small batches of each fuel. The single-cylinder configuration removed the non-linearity of fluid dynamics and heat transfer that occurs within multi-cylinder engines while allowing better identification of trends related directly to combustion. However, this mechanical

fuel system does have a physical limitation as it is not feasible to normalize the engine to expected advances in injection timing from the biodiesel fuels[3, 17, 21, 24].

The engine was equipped with sensors to monitor ambient air temperature, pressure, and relative humidity, engine air mass flow, engine intake air temperature and pressure, fuel mass flow, fuel density, engine torque, exhaust port temperature, downstream exhaust temperature and pressure, and generator load. The researchers employed a Micro-Motion Coriolis flow meter (model #CMF010M) for fuel flow and density measurements. The system includes a FUTEK rotary torque-sensor (model #TRS-705) connected between the engine and generator shafts in order to provide accurate torque values. Engine intake airflow measurements used a Merriam laminar flow element (model #50MW20-2) and an Omega differential pressure transducer (model #PX277-30D5V). The remaining parameters were acquired using appropriate Omega sensors.

A Semtech-DS Mobile Emissions Analyzer (Sensors, Inc.) was used to measure carbon monoxide (CO), carbon dioxide (CO_2), oxygen (O_2), nitrogen oxide (NO), nitrogen dioxide (NO_2), and total hydrocarbon (HC) concentrations in the engine exhaust during the combustion tests. Engine exhaust was transferred to the analyzer through a heated sample line (192°C) connected to a flow straightener installed immediately downstream of the engine muffler at a rate of 8 mL/min. The Semtech-DS utilizes a heated flame ionization detector to measure HCs, a non-dispersive infrared analyzer to measure CO and CO_2 and a non-dispersive ultraviolet analyzer in order to independently measure NO and NO_2. In addition to the gas emissions, particulate matter was captured using a Dekati PM10 low-pressure cascade impactor with 25mm polycarbonate filters collecting particles in 13 stages in a size range of 0.031 to 30 micrometers. A Sogevac Leybold vacuum pump collected exhaust at a flow rate of 10 Liters/minute through the collection system, which consisted of a 4mm inner-diameter sampling line connecting the impactor to a port in the stainless-steel exhaust pipe. Filter masses for each stage were measured before and after PM collection in a controlled-temperature and humidity environment.

Each fuel was tested at five different engine loadings, corresponding to approximately 0%, 25%, 50%, 75%, and 100% of the NorthStar generator rated output (the rated continuous generator power was 80% of the engine's rated continuous power). For each test, emissions and performance data were collected under steady-state operation, as determined by monitoring the change in the engine exhaust temperature 892mm downstream of the exhaust port. When the change in exhaust temperature was less than one percent per minute, the engine was considered to be at steady-state operation. Emissions data was collected for ten minutes at a rate of one sample per second. Engine performance data was recorded at a rate of ten samples per second for two minutes during the emissions data collection period. Following the completion of the data collection at all generator loads, a particulate matter collection test was conducted follows with the engine run for one hour at 25% of generator rating. This extended collection time was required to obtain adequate particulate matter for accurate measurements. Previous work with this engine had demonstrated that a 25% load produces the highest PM levels. At no-load conditions, a lean fuel-to-air mixture in the engine does not permit excessive PM creation. At loads above 25% of generator rating, high in-cylinder pressures and temperatures lead to better combustion and lower PM emissions.

Following data collection, the gas-phase emissions data were averaged over ten second intervals in order to reduce background noise. Raw gas-phase emissions data was converted into fuel specific mass emissions using the Semtech analytical software, as modified for the oxygen content of the biodiesel fuels. Brake specific emissions data were calculated by using the average fuel use and power output recorded during each test.

2.5 Results

Upon completion of the biodiesel tests, the steady-state data for each fuel was analyzed in order to yield emission and fuel consumption levels at each load for direct comparison with ULSD. First, the brake-specific emissions of NO, NO_2, NO_x, CO, CO_2, and HC's from 0% to 100% of generator loading

are shown in Figures 1 through 5, and Figure 7. The brake-specific fuel consumption (BSFC) for each fuel from 0% to 100% generator loading are indicated in Figure 6 and the PM test results are shown in Figure 8. Brake-specific emissions of all constituents were highest at zero loading and decreased as generator load increased, regardless of fuel.

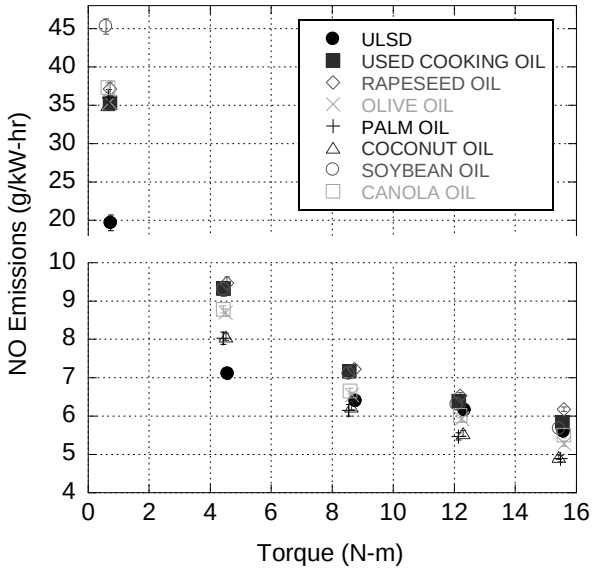

Figure 1. NO emissions for biodiesels and ULSD

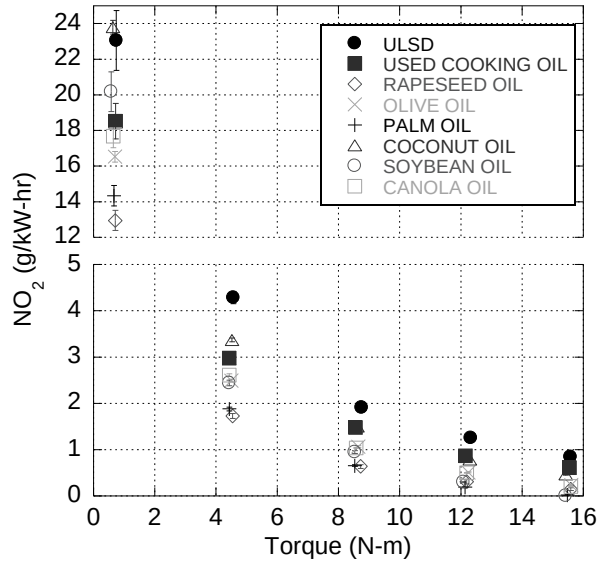

Figure 2. NO_2 emissions for biodiesels and ULSD

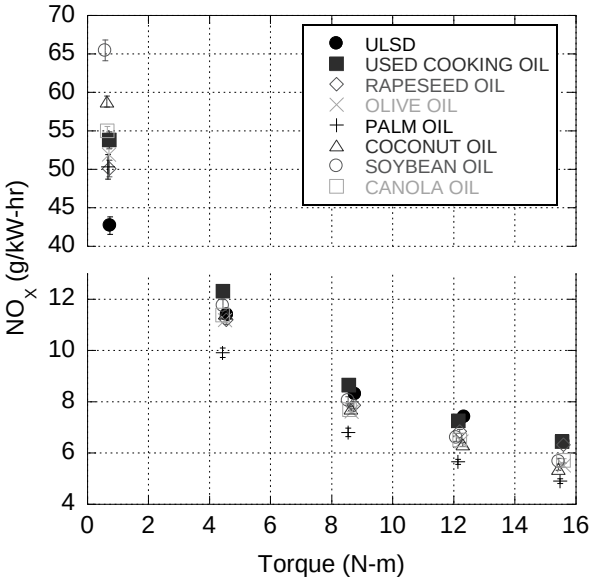

Figure 3. NO_x emissions for biodiesels and ULSD

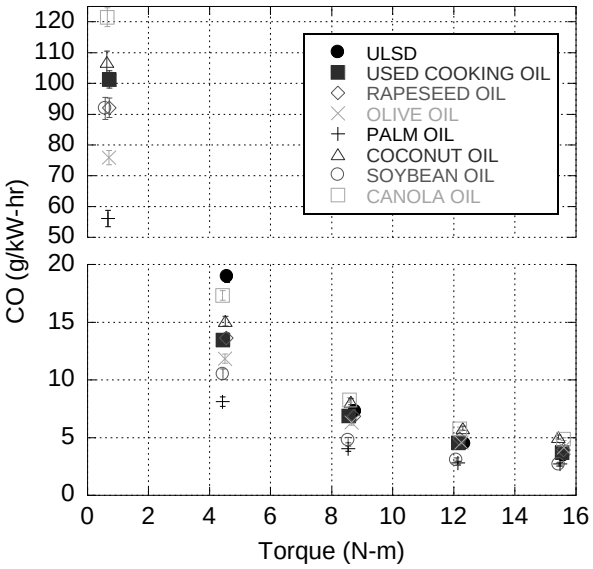

Figure 4. CO emissions for biodiesels and ULSD

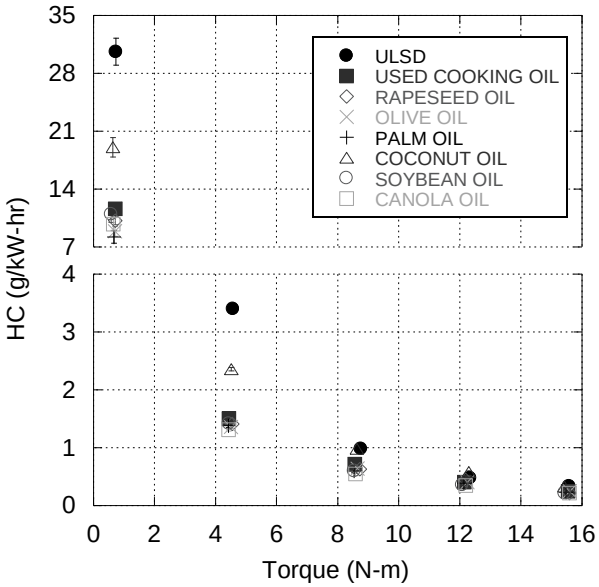

Figure 5. HC emissions for biodiesels and ULSD

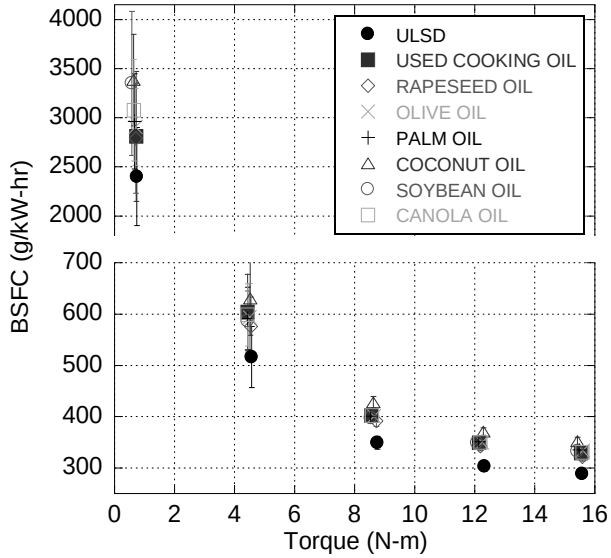

Figure 6. Brake-specific fuel consumption (g/kW-hr) for biodiesels and ULSD

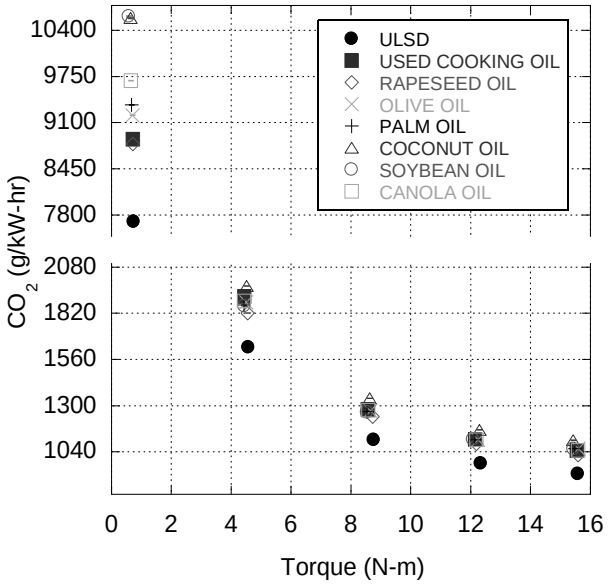

Figure 7. CO_2 emissions for biodiesels and ULSD

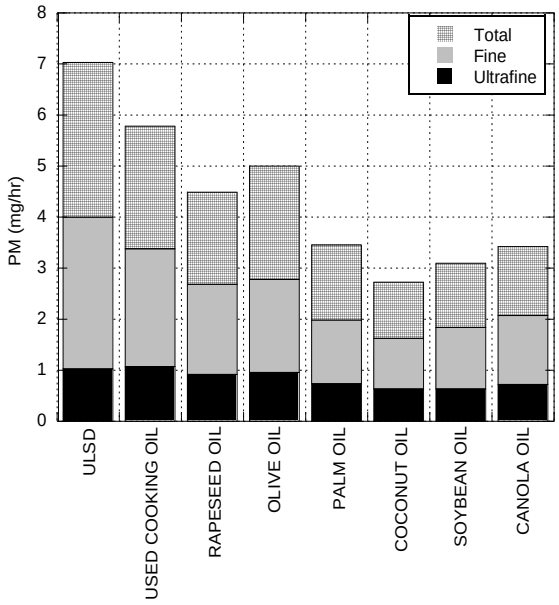

Figure 8. PM emissions results for biodiesels and ULSD (Fine <=10 µm, Ultrafine <=2.5µm)

Inspection of the nitric oxide emission results in Figure 1 indicates that ULSD operation produces lower levels of brake-specific NO than the biodiesels tested at low loads. However, at loads approximately 50% and higher of generator rating, the brake-specific NO emissions of several of the

biodiesels (olive, palm, coconut and canola) are lower than those of ULSD. The trend changes when considering NO_2 emissions. From Figure 2, it is apparent that ULSD produces significantly more NO_2 than any of the biodiesels tested. The biodiesels themselves can be split into several groups, with palm and rapeseed biodiesel generally producing the lowest NO_2 emissions and coconut and used cooking oil producing the highest. With respect to overall NO_x levels (Figure 3), the results indicate that palm oil biodiesel consistently generated the lowest brake-specific NO_x levels of the fuels tested at all engine loadings, while used cooking oil generally produced the highest.

Carbon monoxide and hydrocarbon emissions are generally lower from the biodiesel fuels than from ULSD (Figures 4 and 5), in agreement with previously reported trends. Differences between the biodiesels and ULSD are much more pronounced at lower loading for both compounds. For CO, the greatest reduction was achieved with palm and soy based biodiesel, while the canola and coconut oil based fuels had greater emissions than ULSD at higher loadings. With respect to HC emissions (Figure 5), performance of all fuels except for coconut oil biodiesel was relatively similar. The coconut oil emitted more HC than other biodiesels at all loadings below 100%, and was similar to or worse than ULSD at 50% loading and above.

Brake-specific fuel consumption results (Figure 6) indicate that ULSD consistently has lower fuel consumption than the biodiesels tested. This is expected due to the greater energy content of ULSD and is in agreement with literature findings[25]. Of the biodiesels tested, there was consistent grouping throughout all loads above 0% at an average consumption of 15% more fuel consumed than ULSD. The only major outlier of the biodiesels tested was coconut biodiesel, with an increase in fuel consumption of approximately 22% when compared to ULSD, or 7% more than the other biodiesels. While carbon dioxide is not a regulated air pollutant, it is of significant concern from a greenhouse gas perspective. Raw CO_2 emission levels in the exhaust gas were generally similar for the different fuels. However, as fuel consumption with the biodiesels is increased, brake-specific CO_2 emissions also increased compared

to those of ULSD, as indicated in Figure 7. For example, while the fuel-specific CO_2 emissions of ULSD and canola at 75% generator load are nearly identical (with 3170 g CO_2 emitted per kg fuel from ULSD and 3167 kg CO_2/kg fuel from the canola fuel) the ULSD fuel consumption is about 15% less than that of canola. As a result, brake-specific CO_2 emissions for the biodiesel fuels follow the same trend as fuel consumption, and are around 15% higher than those for ULSD.

The results for the hour-long impactor PM collections are shown in Figure 8. They represent total particulate masses for the one-hour test, as well as the mass of particulates in the ultra-fine (0.1 micron nominal diameter) and fine (< 2.5 micron diameter) particulate classifications. As expected, PM emissions from all of the biodiesel fuels were lower than those observed from the ULSD test. The total particulate emissions from the used cooking oil, which had the highest PM emissions of the seven biodiesels, were approximately 80% of the ULSD emission level. In comparison, the lowest source, coconut oil biodiesel, produced just 36% of the ULSD particulate emissions. For all fuels except for the olive and palm biodiesel, fine particulates were greater than or equal to 90% of total particulate mass. In the palm and olive biodiesel cases, they were 82% and 85% respectively. However, ultrafine particulates were a much more significant portion of the total biodiesel emissions. Ultrafine particulate masses ranged from 45 to 58% of total particulate emissions from the biodiesel fuels, as compared to only 34% of the ULSD total particulates. Thus, the greatest effect of biodiesel on PM emission reductions appears to in reducing emissions of particulates between 0.1 and 2.5 microns in diameter.

2.6 Discussion

A regression analysis was performed on the data using Minitab 15's regression tool in order to further investigate the relationships between fuel properties and exhaust constituents. Results from the rapeseed biodiesel tests were not used in this analysis since the relatively high glycerol content resulted in this fuel exceeded the associated ASTM standard. Hence, this may have affected the fuel's chemical and physical properties. The influence of molar percent unsaturation, molar percent mono-

unsaturation, molar percent poly-unsaturation, poly-unsaturation/mono-unsaturation molar ratio, and H:C molar ratio were examined using only the data from the remaining six biodiesel fuels, as chemical composition data was not available for the ULSD fuel. However, analysis of the CN, density, energy content, oxygen content, kinematic viscosity, and dynamic viscosity effects on engine exhaust emissions did include data from the ULSD tests. A resulting p-value of less than 0.05 across multiple generator loads was assumed to indicate a strong correlation between the independent fuel properties and measured data. All of the fuel properties are independently compared to engine brake-specific fuel consumption, along with brake-specific NO, NO_2, NO_x, CO, CO_2, HC, and PM emissions. The resulting trends are summarized in Table 4 indicating the effects expected from changing only one property at a time based on literature (arrows and references of interest) and experimental results (+ or -). Since the kinematic and dynamic viscosities of a biodiesel fuel are related by its density, the trends observed between changing kinematic and dynamic viscosity are similar in behavior and strength and only kinematic viscosity regression results are reported.

Table 4. Estimated influence on performance and emissions based on literature (arrows) and experimental (+ or -) results

Increasing Property	NO	NO_2	NO_x	CO	CO_2	HC	PM	BSFC
Unsaturation[8,17,18,22]	↑+	↑+	↑+	+	-	-	↔	-
Poly-unsaturation/mono-unsaturation	+	+	+	+	+	+	↔	+
Density[11,17,22]	↑ +	↑ +	↑+	+	-	+	↔	-
Hydrogen:Carbon Molar Ratio	↓ -	↓ -	↓ -	-	+	-	-	+
Energy Content[11,22]	↓	↓	↓	↓ -	↓ -	↓ -	↓	↓ -
Oxygen Content[11,13,22]	↑ +	↑ +	↑+	+	+	+	↓	↑ +
Kinematic/Dynamic Viscosity[9,22]	↑ +	↑ +	↑ +	-	-	-	-	↓-
Cetane Number[17,18,22,23]	↓ -	↓ -	↓ -	↓	↓	↓	↔	↓

2.6.1 Nitrogen Oxide Emissions

Results from the ANOVA regression analysis for nitrogen oxide species (NO, NO_2 and total NO_x) are shown in Tables 5 through 7, with significant correlations at or above 95% confidence (p value $\leq$ 0.05) represented in bold highlighting.

Table 5: NO Regression Results

Variable	Generator Load %			
	25	50	75	100
Cetane Number	**0.018**	**0.017**	**0.016**	**0.021**
Saturation %	0.062	0.124	0.070	0.063
Poly-unsaturation %	**0.022**	**0.025**	**0.033**	**0.042**
Mono-unsaturation %	0.530	0.692	0.523	0.479
Density	**0.009**	**0.006**	**0.005**	**0.002**
Energy Content	0.284	0.377	0.325	0.296
Oxygen Content (% wt)	0.141	0.228	0.164	0.151
Molar H:C ratio	**0.012**	**0.034**	**0.013**	**0.010**
Viscosity	0.187	0.205	0.182	0.143

Table 6: NO_2 Regression Results

Variable	Generator Load %			
	25	50	75	100
Cetane Number	0.587	0.596	0.723	0.879
Saturation %	0.487	0.658	0.753	0.774
Poly-unsaturation %	0.785	0.817	0.697	0.608
Mono-unsaturation %	0.484	0.690	0.923	0.969
Density	0.746	0.528	0.486	0.473
Energy Content	0.086	0.166	0.235	0.296
Oxygen Content (% wt)	0.229	0.333	0.405	0.433
Molar H:C ratio	0.796	0.997	0.932	0.930
Viscosity	0.681	0.970	0.771	0.613

Table 7: NO_x Regression Results

Variable	Generator Load %			
	25	50	75	100
Cetane Number	**0.049**	0.069	0.081	0.108
Saturation %	0.518	0.472	0.326	0.273
Poly-unsaturation %	0.278	0.261	0.288	0.300
Mono-unsaturation %	0.997	0.947	0.679	0.576
Density	0.075	**0.038**	**0.021**	**0.009**
Energy Content	0.884	0.954	0.899	0.774
Oxygen Content (% wt)	0.833	0.774	0.615	0.533
Molar H:C ratio	0.248	0.211	0.126	0.098
Viscosity	0.557	0.386	0.264	0.166

Four variables (cetane number, poly-unsaturation %, density, and molar H:C ratio) were significantly correlated with NO emissions, while the overall unsaturation % was also appreciably

correlated at 90% confidence for most loadings. The biodiesels with the lowest levels of unsaturated and poly-unsaturated fatty acid content, such as palm and coconut biodiesel, had the lowest levels of NO emissions. Double carbon (C=C) bonds in an unsaturated biodiesel molecule release more energy when they are broken in comparison to a carbon-hydrogen (C-H) bond [42]. This causes the combustion temperature and pressure to increase relative to less unsaturated fuels, resulting in higher nitric oxide emissions through thermal NO production[12, 36]. Furthermore, unsaturation may also cause increased oxidation of hydrocarbon radicals during the pre-mixed burn phase promoting heat release and subsequent prompt NO formation[4].

Further consideration of biodiesel unsaturation requires the investigation of the degree of unsaturation in the biodiesel molecules, specifically the relative percentages of single (mono) and multiple (poly) double bonds. Poly-unsaturation follows similar trends to unsaturation with respect to NO, but with higher confidence indicating a stronger correlation (Table 5). This denotes that poly-unsaturation plays a more important role in NO emissions than mono-unsaturation. This effect is likely due to the increased number of carbon double bonds in the fuel molecules, which may increase the likelihood of hydrocarbon radical formation and elevated prompt NO formation[2, 4, 42].

Observation of the nitric oxide emissions trends in Figure 1 indicate that as density increases, NO emissions increase as well. Inspection of Tables 1 and 2 shows a general correlation between density and unsaturation percentage for the biodiesel fuels, likely due to the lower hydrogen content in compounds with a greater number of carbon double bonds. Therefore, density serves as a useful indicator of relative unsaturation (e.g. higher unsaturation % equals larger density), and exhibits a similar, albeit weaker, influence on emissions[2, 4]. In addition, work by Boehman et al. indicates that biodiesel density and bulk modulus are directly proportional[3]. In pump-line injection systems such as the Yanmar engine, the increased bulk modulus likely leads to higher NO emissions via advanced injection, as discussed previously.

A higher biodiesel CN is typically assumed to lead to combustion beginning earlier in the engine cycle than for diesel fuel. This will result in a higher in-cylinder pressure and temperature, more complete combustion, and improved fuel economy[2, 9]. However, this combustion timing advance can also lead to higher thermal NO emissions[1]. The ANOVA regression analysis demonstrated that NO emissions decreased with increasing CN number. This finding is consistent with previous work by McCormick indicating that changes in fuel chemistry, such as unsaturation, play a more dominant role in combustion than thermal NO production through advanced timing[2, 4, 5]. This may not always be the case depending on the relative magnitude of the changes in CN, unsaturation, or timing. Therefore, a slight decrease (–) is indicated in Table 4 based on the ANOVA analysis and literature findings. In future tests, combustion timing will be adjusted as the authors upgrade the system to directly investigate the effects of fuel chemistry.

NO_2 emissions, showed no significant correlations with any of the tested variables in the regression analysis (Table 6). However, some general trends can be observed in the emissions results. The two biodiesel fuels with the lowest overall NO_2 emissions, palm and rapeseed biodiesel, have relatively few characteristics in common aside from a high cetane number. For rapeseed biodiesel, this cetane number is due to the high content of longer chain ($\geq$ C20) fatty acids, which may be an indication of the relatively poor glycerol removal with this fuel. When compared to the coconut biodiesel, which had shorter-chain fatty acids and low NO emissions but some of the highest NO_2 emissions, these results suggest that the length of the fatty acid chains may play a role in NO_2 production. The energy content of the fuel has a weak negative correlation with NO_2 production. The effects were largest at 25% loading, where they were significant at 90% confidence, and decreased at higher engine loads. As most of the biodiesel fuels tested had very similar energy contents, the overall trend is strongly dependent on the coconut biodiesel results. (This fuel had the lowest energy content and highest NO_2 emissions). This effect may be due to higher combustion temperatures in the higher energy content fuels favoring NO

over NO_2 formation. There is no relationship between energy content and NO or total NO_x levels, however, suggesting that it is not significant to overall nitrogen oxide production.

Furthermore, with the exception again of the coconut biodiesel, a trend emerges between NO_2 and unsaturation percentage at low loads for the remaining fuels, with higher unsaturation levels corresponding to higher NO_2 emissions. For example, NO_2 emissions from palm biodiesel are lower than those of canola biodiesel. The canola biodiesel has an unsaturation level of about 94% compared to palm biodiesel's 50% unsaturation, while both fuels have similar energy and oxygen content. In addition, increased poly-unsaturation percentage yields a general increase of NO_2 emissions at low loads and can be observed when comparing soybean and olive biodiesels, which contain similar unsaturation percentage, energy content, and oxygen content. These trends can be explained in a manner similar to the NO emissions; e.g., higher in-cylinder temperature from unsaturated biodiesels yields more NO formation, which in turn is converted to more NO_2 in the flame[1]. At high engine loads, most of this NO_2 is converted back to NO. Under low-load conditions, cooler gas regions may exist that inhibit conversion of NO_2 back to NO by quenching of the hot in-cylinder gases, resulting in higher NO_2 emissions[1].

When NO and NO_2 results are combined together, three of the four significant variables for NO (cetane number, density, and H:C ratio) show some correlation with overall NO_x emissions. The cetane number correlation is stronger at lower engine loads, where NO emissions from palm oil, which had the highest cetane number, were lower than those of the other fuels. This is likely a result of lower overall NO production and the influence of increased NO_2 production at low loads. The H:C ratio was significant at 90% confidence only at the highest engine loading, but followed the same trend as for NO.

In addition to any correlations with fuel unsaturation content, density may also play a secondary role in NO_x formation via the mechanical injector used on the Yanmar engine. This is because the engine injects a constant volume of fuel resulting in more mass injected per cycle as density increases, leading

to a lower air-to-fuel ratio. This will create higher combustion temperatures and could result in additional NO_x formation. Moreover, density was weakly correlated with BSFC (although not at significant levels), which provides further justification for this theory. The lack of significance for other variables, such as poly-unsaturation percentage, may suggest that these properties may work at cross-purposes with respect to NO and NO_2 production.

Oxygenated fuels are generally believed to bring fuel-rich zones near the injector closer to stoichiometric combustion ratios, causing hotter combustion and higher pressures that lead to increased NO_x production[17, 27]. However, this work did not observe a correlation between fuel oxygen content and NO_x production. As even the least oxygenated biodiesel fuel (rapeseed oil) had an oxygen content > 9%, it may be that all of the tested fuels were sufficiently oxygenated that any increases had minimal effect on combustion processes.

2.6.2 Partial Combustion Products

No significant correlations were observed between the tested fuel properties and carbon monoxide emissions. The two biodiesel fuels with the lowest CO emissions, palm and soy biodiesels, do have some of the lowest mono-unsaturation levels of the tested biodiesels, but are not otherwise particularly similar. CO emissions generally decrease with higher energy content due to improved BSFC, higher in-cylinder temperatures, and less carbon added to the engine, providing ample opportunity for the CO to oxidize in lean zones[1]. However, the effect of changing oxygen content is important to consider here as a biodiesel injected with higher energy content will generally have lower oxygen content. As a result, the mixture in the engine is slightly richer overall, and is richer near the injector. This may act to raise CO emissions, offsetting any reduction effect from energy content.

Hydrocarbon emissions showed significant correlations to oxygen content, energy content, and unsaturation percentage (Table 8).

Table 8: HC Regression Results

Variable	Generator Load %			
	25	50	75	100
Cetane Number	0.682	0.661	0.475	0.504
Saturation %	**0.023**	**0.051**	**0.026**	**0.042**
Poly-unsaturation %	0.328	0.300	0.176	0.167
Mono-unsaturation %	0.076	0.154	0.180	0.237
Density	0.420	0.539	0.347	0.412
Energy Content	**0.001**	**0.002**	**0.001**	**0.001**
Oxygen Content (% wt)	**0.003**	**0.006**	**0.001**	**0.003**
Molar H:C ratio	0.099	0.160	0.088	0.121
Viscosity	0.171	0.315	0.227	0.281

The canola biodiesel had both the lowest HC emissions and the highest unsaturation percentage of the fuels used in the regression analysis. In general, higher unsaturation levels will reduce HC emissions for the same reason they increase NO: double C=C bonds have greater energy content and lead to both hotter and more complete combustion. In contrast, coconut biodiesel had both a very low unsaturation percentage and the highest HC emission of all the biodiesel fuels. These effects were greatest at low engine loadings, and probably account for the mild correlation with H:C ratio and mono-unsaturation content at 25% load.

More energy in a given mass of fuel will be able to perform more work. Therefore, the self-regulating mechanical fuel pump on the Yanmar engine will lower the fuel flow rate as a more energetic fuel is added; thus, resulting in correspondingly lower fuel consumption. Since there is less fuel used, less carbon is being introduced into the cylinder, resulting in lower HC, CO, and CO_2 emissions from higher energy content fuels. Since engine intake air is nearly constant, but more oxygen is present in the fuel upon injection, the overall mixture in the engine during combustion will become leaner with fuels that have higher oxygen content. This additional oxygen should lead to reduced HC (and CO) emissions as oxidation can occur more readily. However, increasing oxygen content in the fuel also leads to decreased energy content due to the displacement of carbon and hydrogen atoms. The combination of reduced energy content and lean combustion requires that additional fuel be added in

order to maintain the required power output. In our experimental results, this second factor was decisive, as HC emissions increased with rising oxygen content.

2.6.3 Fuel Consumption

Table 9 shows that multiple fuel properties are significantly correlated to brake-specific fuel consumption. Note that the regression results for brake-specific CO_2 emissions are not shown as they follow the same patterns as BSFC due to the relationship between the amount of fuel combusted and CO_2 emissions.

Table 9: BSFC Regression Results

Variable	Generator Load %			
	25	50	75	100
Cetane Number	0.674	0.550	0.513	0.408
Saturation %	0.084	**0.024**	**0.010**	**0.004**
Poly-unsaturation %	0.228	0.192	0.210	0.192
Mono-unsaturation %	0.284	0.161	0.096	0.082
Density	0.576	0.325	0.224	0.114
Energy Content	**0.001**	**0.001**	**0.001**	**0.001**
Oxygen Content (% wt)	**0.001**	**0.001**	**0.001**	**0.001**
Molar H:C ratio	0.203	0.080	**0.039**	**0.016**
Viscosity	0.346	0.152	0.080	**0.036**

As discussed previously, higher fuel energy content allows for reduced fuel consumption given the same amount of work. Moreover, increased oxygen content has the opposite effect due to the corresponding reduction in the mass of carbon per fuel volume and subsequent lower energy content. The fuel with the highest BSFC, coconut biodiesel, had the highest oxygen content and lowest unsaturation percentage, as well as an abundance of short-chain fatty acid molecules. Differences in BSFC between the other biodiesel fuels were much smaller, although all were higher than that of the ULSD.

As biodiesel viscosity increases, BSFC also decreases. This decrease may be due to less-viscous fuels leaking through the clearances of the mechanical fuel pump on the Yanmar engine used in this study, which utilizes a single plunger and barrel configuration more prone to leakage[9]. This leaking of

fuel will cause the fuel pressure to rise more slowly inside the pump, causing the mechanical governor to increase fuel flow to compensate. This increased BSFC leads to correspondingly higher CO_2 emissions as viscosity decreases. In addition, it is reported that longer biodiesel chains lead to an increase in CN[9, 20, 23, 36, 40, 43] and energy content that can both decrease fuel consumption. Attempting to compare ULSD with the biodiesel fuels is not feasible in this study with respect to viscosity. While coconut oil biodiesel and ULSD have similar viscosities, all of their other properties are dissimilar; hence, a trend cannot be inferred based purely on viscosity as other factors add significant non-linearity.

2.6.4 Macroscopic Trends

The regressions analyses shown in Tables 5-9 indicate that several fuel property correlations are strengthened at higher engine loads. In many cases, this series of stronger linear trends can be explained by improved combustion efficiency, higher cylinder pressure, and longer combustion duration. This is because as load increases, larger quantities of fuel are injected by an extended injection event as mechanical pump pressure remains relatively constant (e.g. the fuel injector is opened for longer). This alters the changes observed on BSFC, NO, NO_2, CO, CO_2, and HC emissions. At low loads, where the mixture is especially lean and cool in regions of the cylinder away from the injector, combustion is not as efficient and may be quenched more easily. In addition, PM that forms in fuel-rich zones near the injector may not oxidize as effectively, especially during post-flame oxidation. This permits some CO and HCs to go unburned and promotes the stabilization of NO_2 in the cooler regions of the cylinder. At higher loads, in-cylinder temperatures climb with the injection of additional fuel. The additional fuel causes more CO_2 emissions, but fewer CO and HC emissions due to improved combustion. Fewer cool regions means that less quenching of the combustion gases will occur leading to significantly less NO_2 exiting the engine, but persistent high temperatures and abundant near-stoichiometric regions near the injector will permit additional NO to form. It is noted that as engine load increases, the effects of biodiesel unsaturation and poly-unsaturation on BSFC, NO, and CO_2 become

more apparent. In addition, as engine load increases, biodiesel density appears to play a stronger role in NO emissions. Furthermore, the ratio of hydrogen to carbon molecules and viscosity in biodiesel is a more important factor on BSFC at higher loads. Finally, the strength of the trends between biodiesel viscosity and BSFC, NO, and CO_2 becomes stronger as larger quantities of fuel are injected at high loads. Due to these findings, it is useful to consider more than a single engine loading when studying the complex variability of biodiesel fuels and their influence on engine performance and emissions.

2.7 Conclusion

In order to gain a more complete understanding of the effects that various biodiesel feedstocks have on engine performance and emissions, seven biodiesel fuels were produced using feedstock oils specifically chosen to yield significantly different chemical properties, especially concerning molecular saturation. These biodiesels were tested in a single-cylinder diesel engine test cell where the engine load was changed and fuel consumption was measured. In addition, NO_x, CO, CO_2, HC, and PM emissions were recorded. The resulting performance and emission levels were analyzed in order to observe changes arising from varying biodiesel properties.

Biodiesel use led to higher brake-specific fuel consumption compared to ULSD, while resulting in lower emissions of CO, HC, and PM. All of these trends are consistent with published works on biodiesel combustion[2, 9, 12, 17, 19, 21-27]. Several of the fuels tested produced lower brake-specific NO_x emissions than ULSD, while others showed increased NO_x. Our analysis indicated that biodiesel unsaturation and poly-unsaturation percentages (on a mass basis), density, hydrogen: carbon molar ratio, energy content, oxygen content, and biodiesel viscosity all play significant roles with respect to engine performance and emissions. (The general effects of each fuel property on specific measured performance and emissions parameters are summarized in Table 4). This work confirms trends observed in literature with regards to increasing NO_x emissions as a function of increasing unsaturation or decreasing density [2, 4, 17, 33]. In addition, it suggests that the nature of the fuel unsaturation is a

critical parameter, as fuels with higher poly-unsaturation content had the greatest reduction in NO emissions and did not show consistent increases in NO_2.

While it is possible to mitigate NO_x emissions in a diesel engine, these efforts are costly and require precise engine control to be successful[13, 37]. Therefore, potential use of NO_x reducing fuels makes reaching emission regulations easier, with lower aftertreatment requirements. Using the correlations found in this work, it is now possible to estimate the resulting engine NO_x emissions and fuel consumption for a biodiesel fuel before testing. In addition, these results can be used in an effort to design biodiesel fuels with improved NO_x emissions profiles or that more closely match ULSD with respect to NO_x emissions and fuel consumption. Further research will be required, however, to determine how blending will affect the performance of these biodiesel fuels, as the effects of some fuel compositional properties may be substantially non-linear.

2.8 Acknowledgments

This research was partially funded by the University of Kansas, Transportation Research Institute from Grant # DT0S59-06-G-00047, provided by the US Department of Transportation – Research and Innovative Technology Administration.

CHAPTER 3: Design, Construction, and Validation of the In-cylinder Pressure Recording System

3.1 Introduction

Completion of the first round of biodiesel testing combined with the resulting research and data analysis indicates that it is difficult to draw conclusions about the exact causes of increased NO_x emissions with changes in biodiesel usage. Specifically, it was observed that increasing biodiesel density results in higher NO_x emissions. However, density serves as an indicator of other physical properties, such as cetane number, bulk modulus, and molecular unsaturation. Without the capability within KU laboratories to measure CN and bulk modulus, it was impossible to indicate either of these fuel properties as a direct culprit for the observed changes in emissions because of the uncertainty of what was taking place inside the engine during operation. As a result, a system to monitor and record pressure inside the diesel engine while the engine operates was designed, built, and tested for validation while running dissimilar fuels in the engine. The data recorded by this system allows researchers at KU to observe the effects of injection timing and combustion delay.

Most engine test cells utilize in-cylinder pressure transducers and high-speed encoders in conjunction with data-logging systems in order to record cylinder pressure during engine operation [1, 44, 45]. Real-time data displayed in the form of plots or calculated indicated performance parameters provide useful information for the researchers while the engine undergoes changes in fuel type or operating mode; e.g. low load versus high load. Post-processed data can offer significant insight into the thermodynamic cycle; particularly the injection and combustion processes that help define the difference between unique fuels.

While several useful combustion properties can be determined from the cylinder pressure data, the most important of these is the heat release rate [1, 16, 18]. Heat release rate is defined as the rate at which the chemical energy of a fuel is released during the combustion process [1]. This parameter provides insight into how the chemical energy from the fuel is distributed during the combustion

process. Moreover, it can highlight the effects of different injection profiles or fuel characteristics. Furthermore, the heat release rate can be divided into gross and net heat release rates. The gross heat release rate is the total energy released by fuel combustion, while the net heat release is the difference between the gross heat release rate and the heat loss to the coolant or surroundings in the case of the Yanmar engine. The net heat release rate indicates the work that is applied to the piston and the change in internal energy of the combustion products [1].

Plotting heat release rates for a fuel against engine crank angle, such as in Figure 9 [1], can provide a direct comparison between two fuels with regards to the delay in start of combustion (ignition delay), magnitude of the premixed combustion phase, and mixing-controlled and late combustion phases [1].

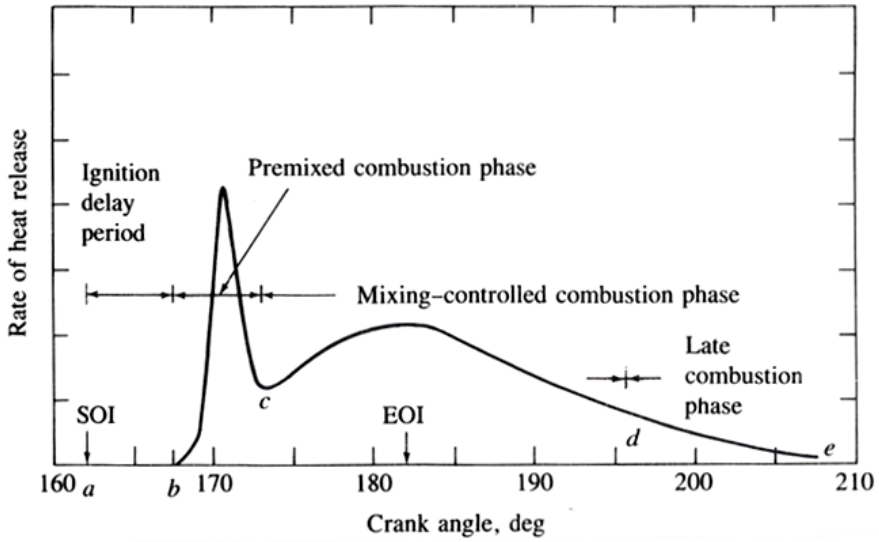

Figure 9. Sample Heat Release Diagram from Heywood [1]

The ignition delay (points *a* to *b* in Figure 9) and magnitude of the premixed combustion phases are particularly important for understanding the formation of NO_x and may help explain the differences between the emissions for biodiesel and ULSD. Ignition delay is the period between the start of fuel injection and the beginning of combustion [1]. It is understood that biodiesel will have an earlier start of combustion than ULSD due to its higher Cetane Number that can potentially result in higher cylinder

pressures even though as a fuel it contains less chemical potential energy [17]. Premixed combustion is the phase where the fuel that has mixed with air (within flammability limits) combusts rapidly, resulting in a rapid release of energy [1]. Since biodiesel is oxygenated, it will burn more rapidly than ULSD once combustion begins resulting in a larger portion of heat release and a higher initial burning rate that further increases cylinder temperatures and NO_x formation due to the thermal NO_x (aka Zeldovich) mechanism [1, 17]. The Zeldovich mechanism characterizes NO_x formation (specifically NO) and is strongly dependent on temperature; in essence, as temperatures increases, NO production increases. The mixing-controlled and late combustion phases occur as injected fuel becomes ready for combustion. In these phases, the heat release rate is diminished and the secondary peak during the mixing-controlled combustion phase may not be present[1].

In addition to an improved understanding of fuel combustion, the recorded cylinder pressure data can also be used to quantify engine performance in the form of Indicated Mean Effective Pressure (IMEP), and indicated work. These parameters are split into gross, pumping, and net portions. Here, gross indicates the work or effective pressure applied to the piston during the compression, combustion and expansion strokes while pumping characterizes the exhaust and intake strokes (aka the breathing process of the engine). The gross work contains the work delivered by the high pressure from combustion and is characterized by a positive magnitude. By contrast, pumping work indicates the amount of work necessary to expel exhaust and bring in fresh intake air and, for naturally aspirated engines such as the Yanmar, is often negative, indicating energy is lost. Finally, net IMEP or net indicated work determines the work or effective pressure applied to the piston throughout the entire four-stroke engine cycle and is the sum of the gross and pumping IMEP and indicated work [1, 16, 18]. Indicated work for gross and pumping cycles are demonstrated in Equations 1 and 2, and related with net indicated work in Equation 3:

Indicated Work (gross) from Intake Valve Closing (IVC) to Exhaust Valve Opening (EVO)	$W_{i,g} = \int_{V_{IVC}}^{V_{EVO}} p \cdot dV$	(1)
Indicated Work (pumping) from Exhaust Valve Opening (EVO) to Intake Valve Closing (IVC)	$W_p = \int_{V_{EVO}}^{V_{IVC}} p \cdot dV$	(2)
Net Indicated Work	$W_{i,n} = W_{i,g} + W_p$	(3)

where $W_{i,g}$ is the gross indicated work, p is the pressure in the engine cylinder, dV is an infinitesimally small change in volume, W_p is pumping indicated work, and $W_{i,n}$ is the net indicated work. The gross IMEP ($imep_g$) and pumping mean effective pressure ($pmep$) are related by the displacement of the engine (V_d) as follows [1]:

Indicated Mean Effective Pressure	$imep_g = \frac{W_{i,g}}{V_d}$	(4)
Pumping Mean Effective Pressure	$pmep = \frac{W_p}{V_d}$	(5)

By observing changes in the resulting mean effective pressure and heat release analysis, a more complete understanding of engine operation is gained. The use of such an analysis would have improved the work discussed in Chapter 2, as it would have reduced the ambiguity of the conclusions regarding the biodiesel characteristics. Specifically, the direct effects of bulk modulus on biodiesel injection could have been investigated as the injection timing and duration relative to the engine cycle can be directly observed. In addition, the effect of varying Cetane Number would have been apparent, as the length of delay from the start of injection to the start of combustion is determined directly from the recorded data.

3.2 System Design and Construction

In order to perform an accurate analysis for calculating injection and combustion timing in a diesel engine, careful consideration must go into the data acquisition system's requirements and overall design. For instance, proper pressure recording resolution is important as poor resolution leads to greater uncertainty concerning both injection timing in the cylinder and the combustion event. Kistler, a

popular sensor manufacturer, recommends a sampling resolution between 0.1° and 1°. However, a high engine speed requires a rapid signal frequency given the short amount of relative time between crank angles. For example, 0.5° resolution at 3600 RPM requires a 43.2 kHz signal. In addition, the pressure in a diesel engine can become relatively high due to its high compression ratio and rapid heat release [1]. For the Yanmar engine at KU, a cylinder pressure up to 70 bar may occur. These stringent requirements can only be met using advanced equipment designed specifically for the high speed and combustion conditions experienced.

3.2.1 Equipment Installation

To meet the need for a robust and compact pressure sensor, a Kistler 6052C piezoelectric transducer is utilized as it is touted for its small, but rugged, design that is suitable for high pressures found in diesel engine studies. It is calibrated to measure from 0 to 250 bar with less than 0.5% error at up to 160 kHz; far exceeding the requirements of this application. In addition, its sensitivity to thermal shock, caused by rapidly changing temperatures, is less than 0.5 bar and it is a convenient size for installation in the relatively small and crowded area of the Yanmar cylinder head. The 6052C transducer works via the piezoelectric effect in which a change in pressure applied to a crystalline solid results in a change in electrical charge [16]. This crystal is built into the transducer and is normally neutral in charge, but becomes more negative as the pressure increases. In the case of the transducer used at KU, an increase in pressure results in a charge that becomes more negative by -20 pC/bar. Using this linear transducer, it is possible to measure and record high pressures with great speed and accuracy.

Installation of the sensor in the head of the Yanmar was relatively straightforward. The transducer is placed in a vacant region of the cylinder head between the injector and valve cover as seen in Figure 10.

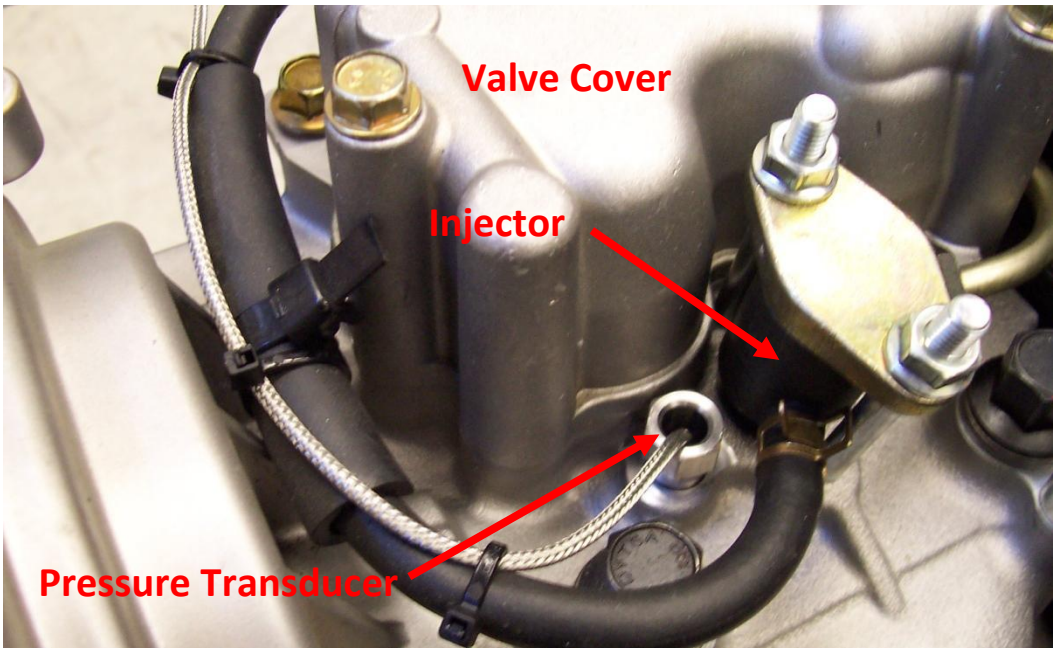

Figure 10. Pressure Transducer Location on Cylinder Head Outside of Engine

This spot places the sensor near the piston bowl per the instructions in the 6052C manual in order to avoid unusual pressure readings in the squish zones of the cylinder. A squish zone is an area on the piston where gases move rapidly across the surface of the piston it approaches Top Dead Center (TDC). The Yanmar's piston is designed with a geometry to improve mixing and, therefore, combustion. The squish zones are indicated in Figure 11.

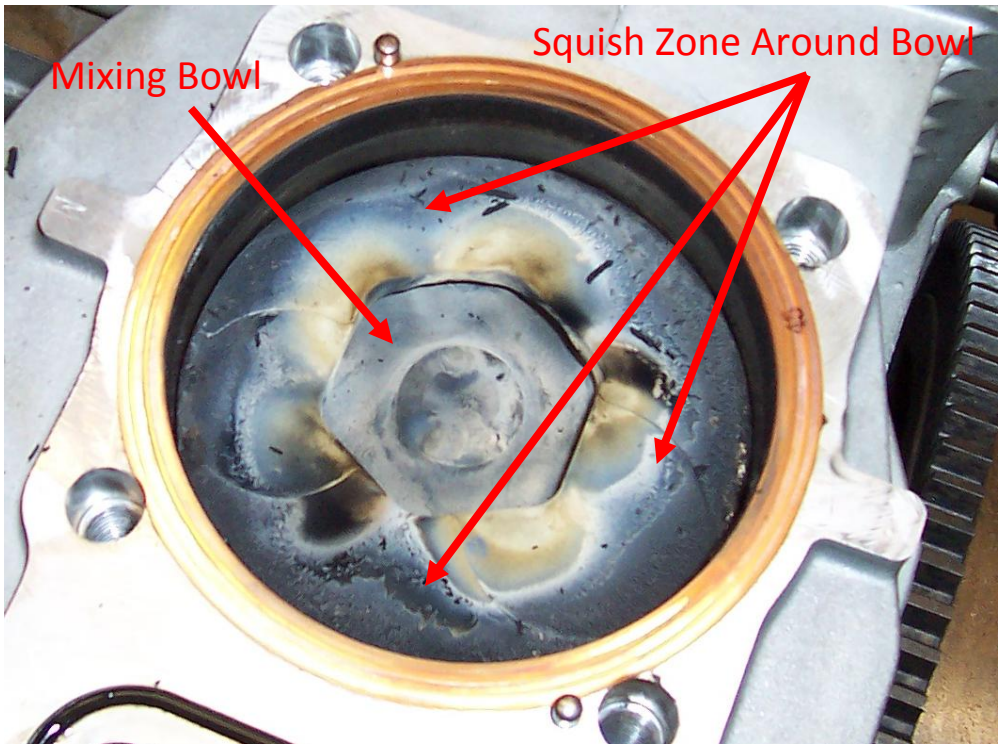

Figure 11. Top Surface of Yanmar Piston

The relative location of the sensor compared to the injector and intake and exhaust ports is shown in Figure 12.

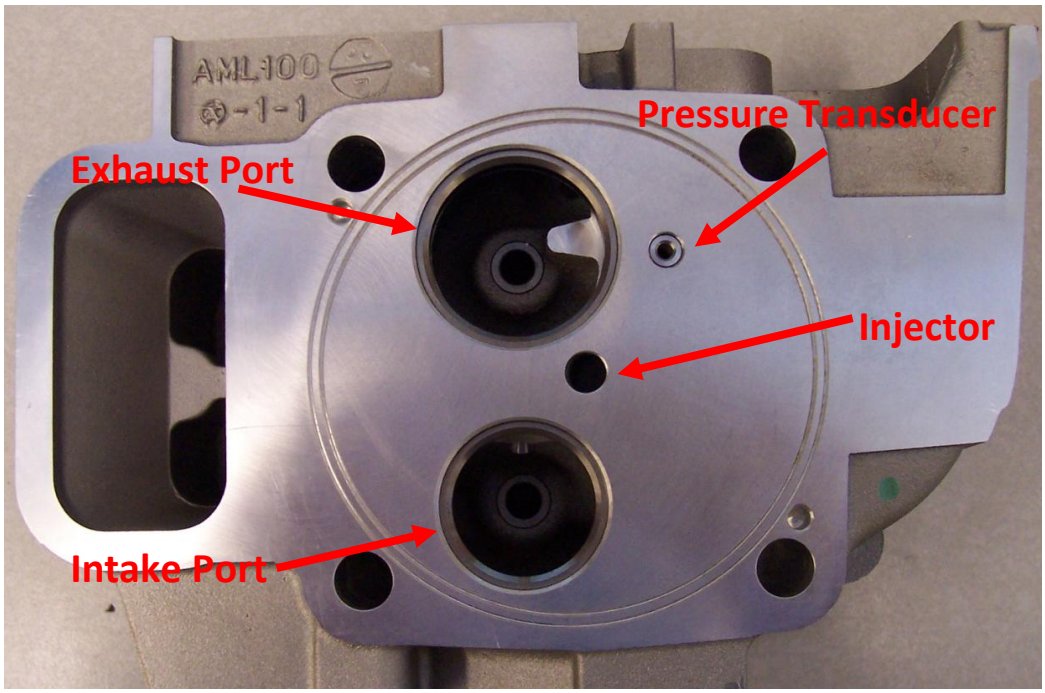

Figure 12. Bottom View of Cylinder Head with Transducer Location (Inside Cylinder)

During the process of drilling out the transducer location, the small EGR passage between the intake and exhaust passages was blocked so that external EGR regulation can be performed in the future, as discussed in the first chapter. Before the external EGR system is installed on the engine, improved performance will be seen as compared to the stock engine configuration. Since exhaust gas is no longer displacing air in the intake charge, the engine brings more air into the cylinder during the intake portion of the thermodynamic cycle. Therefore, fuel oxidation occurs more readily making combustion hotter and more complete. This leads to an improvement in fuel economy; however, higher NO_x emissions will be evident as the re-circulated exhaust gas is not present to act as an inert heat sink [1]. As a result, it will be necessary to repeat some of the efforts of Chapter 2 as it utilized the stock cylinder head including the EGR passageway. The location of the EGR passage is shown in Figure 13.

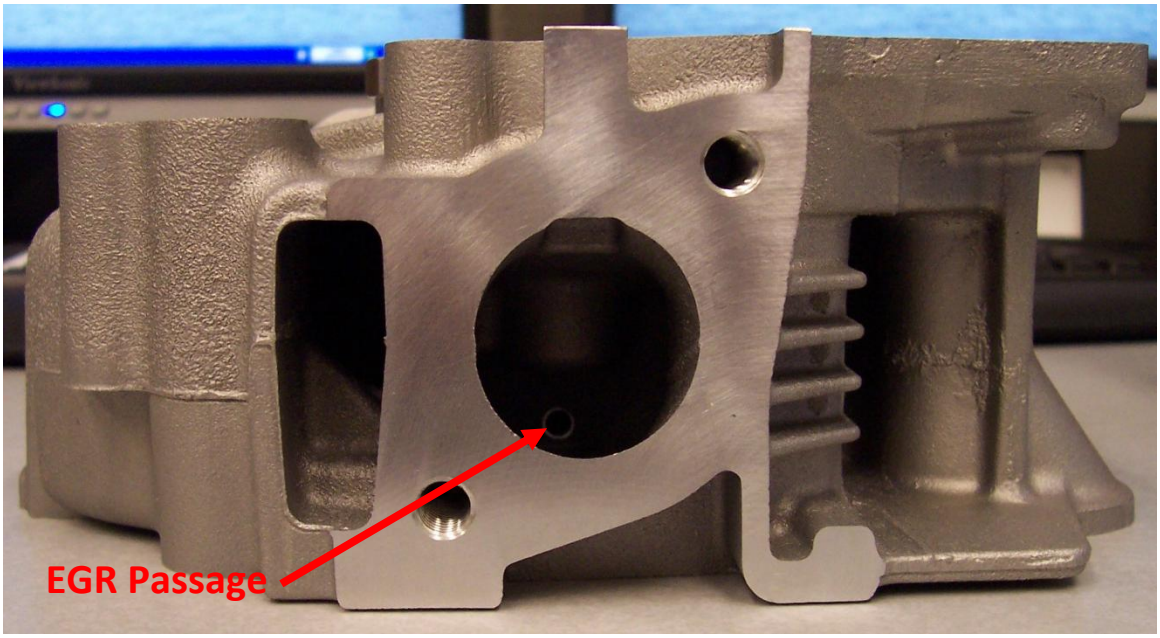

Figure 13. EGR Passage from Exhaust Side to Intake Side

As stated before, the pressure transducer outputs a linear change in voltage as cylinder pressure fluctuates. However, this change is relatively small as compared to the 16-bit, ±10VDC measurement

capabilities of the National Instruments data acquisition systems implemented in the Learned Hall test cell. As a result, Kistler manufactures a charge amplifier that increases the amplitude to a scalable 0-10 VDC signal that can be directly wired into the acquisition circuitry. This charge amplifier, the Kistler 5011B, also utilizes a low-pass filter in order to reduce the noise in the piezoelectric signal aiding in resolution. This amplifier scales the output of one Volt to 10 bars of pressure; hence, a 70-bar pressure would be represented as 7 VDC.

In order to measure representative cylinder pressure versus volume data for combustion analysis, it is imperative to determine the engine crank angle that corresponds to the measured pressure data. This is usually accomplished using an incremental optical encoder that functions using a light source and light receiver separated by a rotating disk with narrow slits cut around its surface in a radial orientation that intermittently allow the emitted light to reach the light receiver. These slits are evenly spaced apart in order for the light receiver to detect and output an analog wave that corresponds to a determined change in angle. In the case of the Kistler 2614B used at KU, a secondary slit on the disk is used to reference piston TDC and a secondary light receiver outputs a voltage when TDC is reached. The correct reference of TDC is also critical as it serves as the starting point for counting increments for every revolution. An error in TDC reference of just 1^{o} can lead to up to a 5% error in the calculation of indicated mean effective pressure (IMEP) [18]. The Kistler encoder features an adjustable flange that allows the encoder to be bolted directly to the flywheel of the Yanmar engine. From the encoder, the analog light receiver signals are wired into a signal converter that converts its value into digital crank angle and TDC signals. From the signal converter, the digital signal is sent to a pulse multiplier (Kister model #2614B4) that can be used to change the encoder angle resolution from a range of 0.1^{o} to 6^{o}. Finally, these digital signals are then connected to the acquisition system and used for crank angle and pressure signal recording.

Installation of the encoder requires attachment to the flywheel of the engine. In the case of the Yanmar engine, this requires removal of the pull-rope starting mechanism (Figures 14 and 15) in order to gain access to the flywheel. Since the engine is also factory-equipped with an electric start system, the pull-rope system is not necessary and can be removed without issue as the electric starter is still in place.

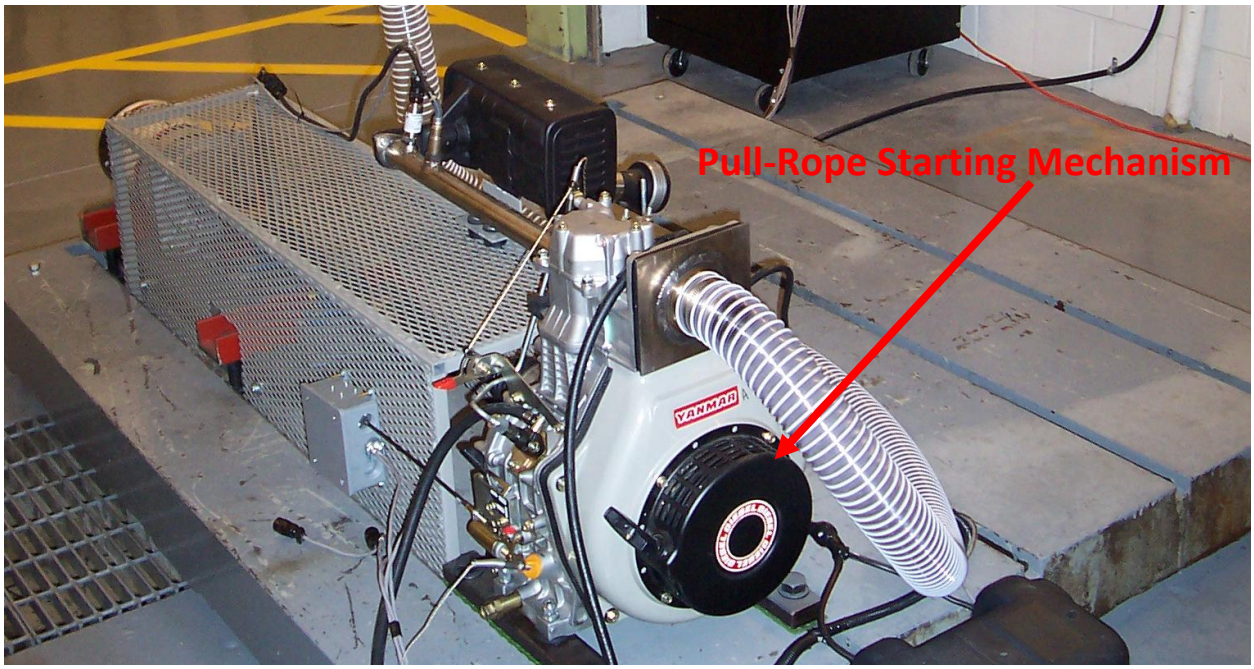

Figure 14. Stock Yanmar Engine in Test Cell with Pull-Start Mechanism Indicated

Figure 15. Yanmar Pull-Rope Starting Mechanism Disassembled from Engine

After the removal of the pull-rope start mechanism, a custom adapter is needed to connect the Kistler encoder to the flywheel. Maintaining precise axial center is critical in order to minimize vibration and forces on the bearings of the encoder. The adapter is designed to fit on the machined surface in the center of the flywheel face with an inside diameter large enough to clear the flywheel retaining nut. Three tapped holes are placed on the face of the adapter in order to bolt the Kistler flange directly to the adapter. The final design was created using Autodesk Inventor and is shown in Figure 16. The completed adapter, built by the KU Mechanical Engineering machine shop, is shown connected in Figure 17 and can be compared to the blank flywheel (Figure 18).

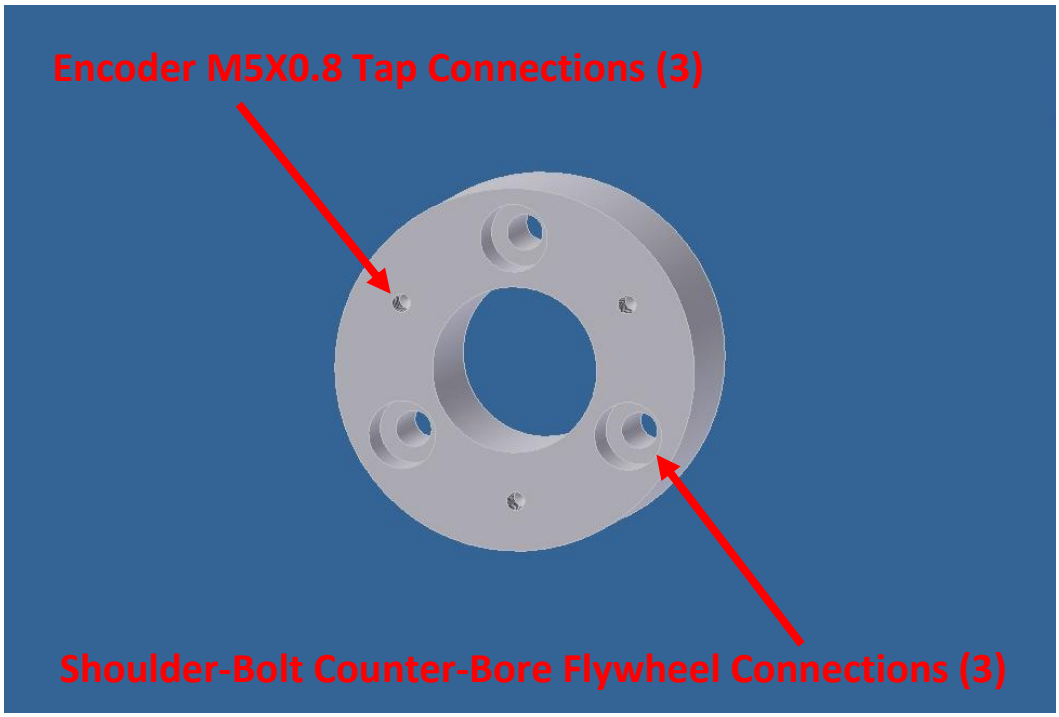

Figure 16. AutoCAD Inventor Flywheel Adapter Rendering

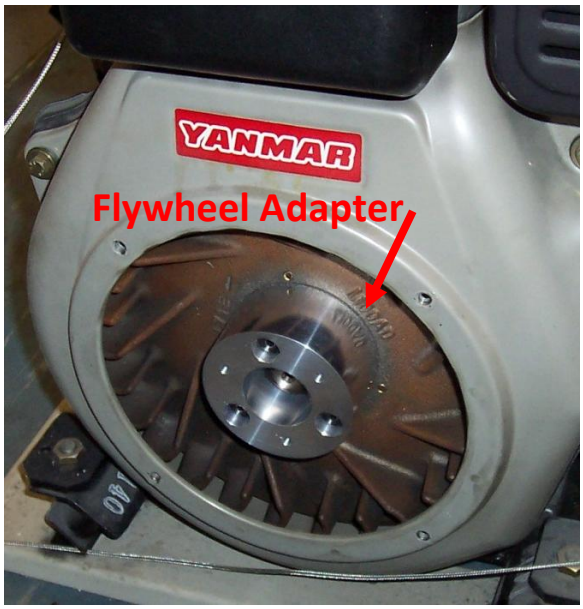

Figure 17. Adapter Mounted on Flywheel

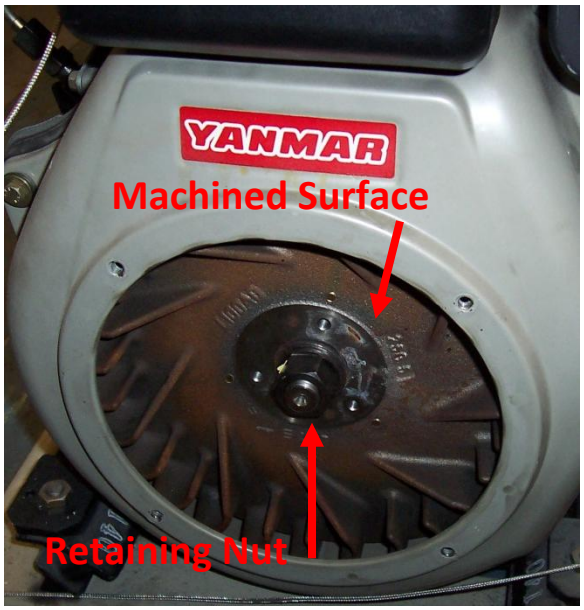

Figure 18. Blank Yanmar Flywheel

Once the adapter is connected, the attachment of the encoder is straightforward. However, the linkage of the encoder requires a stationary connection point in order to keep the main housing of the encoder steady while the engine and encoder flange spin. The length of the linkage is adjustable and is used to set the TDC trigger reference. The linkage connection point is made from a sheet of ¼" PVC that bolts between the flywheel cover and the original pull-rope housing. TDC is found by removing the cylinder head and measuring the distance down from the head gasket surface to the top surface of the piston. TDC is the point when this distance reaches a minimum. Moreover, Yanmar engines are machined with a TDC mark on the flywheel that can be used to verify the measured location.

Figure 19 illustrates the final installation of the encoder on a second Yanmar engine used for initial testing and debugging. This engine is the same model as the engine currently installed in the biodiesel engine test cell. Installing the system on this spare engine meant that while initial system testing was underway, the main engine in the test cell was not affected and could be used for other tests (e.g., the efforts of Chapter 2). Figure 20 shows the installation on the primary Yanmar engine following a swap of cylinder heads between the two engines.

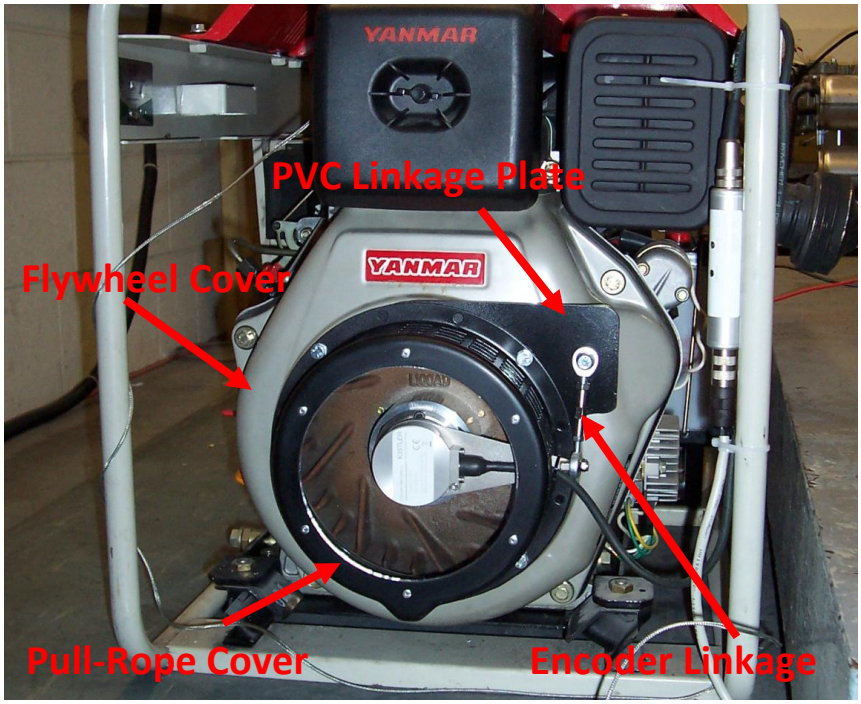

Figure 19. Encoder Linkage and Cover on Back-up Yanmar Engine

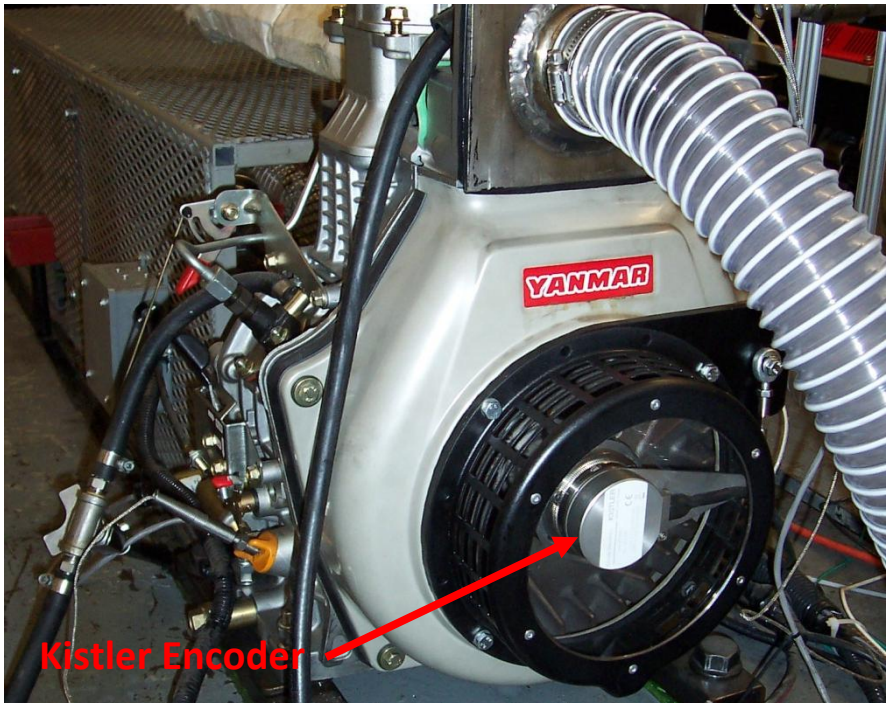

Figure 20. Final Encoder Installation on Primary Yanmar Engine

Due to the speed requirements of the cylinder pressure recording system, the design of the acquisition system required extra attention concerning both sampling rate and storage capacity. For example, since the engine currently runs at 3600 RPM (60 Hz), a sampling resolution of 0.5^{o} dictates that

the system record crank angle and pressure readings at a rate of 43.2 kHz. This rate greatly exceeds the sampling ability of standard National Instruments acquisition systems, such as the first cRIO used to control the test cell. In addition, since data for 40 complete engine revolutions is recorded for averaging purposes, a total of 28800 data points are recorded each time data is taken. To meet these requirements for speed and storage, a dedicated computer with a terra-byte of storage and a National Instruments PCIe-7841R card is used. The PCI card contains a Field-Programmable Gate Array (FPGA) chip that has the capability to perform sampling up to 200 kHz that exceeds the rate of the pressure transducer and will allow the pressure sampling resolution to be increased up to 0.25^{o} at 3600 RPM if desired. Slower engine speeds would allow sampling at even finer resolution (0.1^{o}). In addition, the card has ample space for future analog and digital sensors and 16-bit resolution for high accuracy. The dedicated computer, with internal NI acquisition card, and the Kistler encoder pulse multiplier and charge amplifier are located in the instrumentation cabinet in the Learned Hall test cell and are shown in Figure 21. This marks the completion of equipment installation for the in-cylinder pressure and volume measurement system.

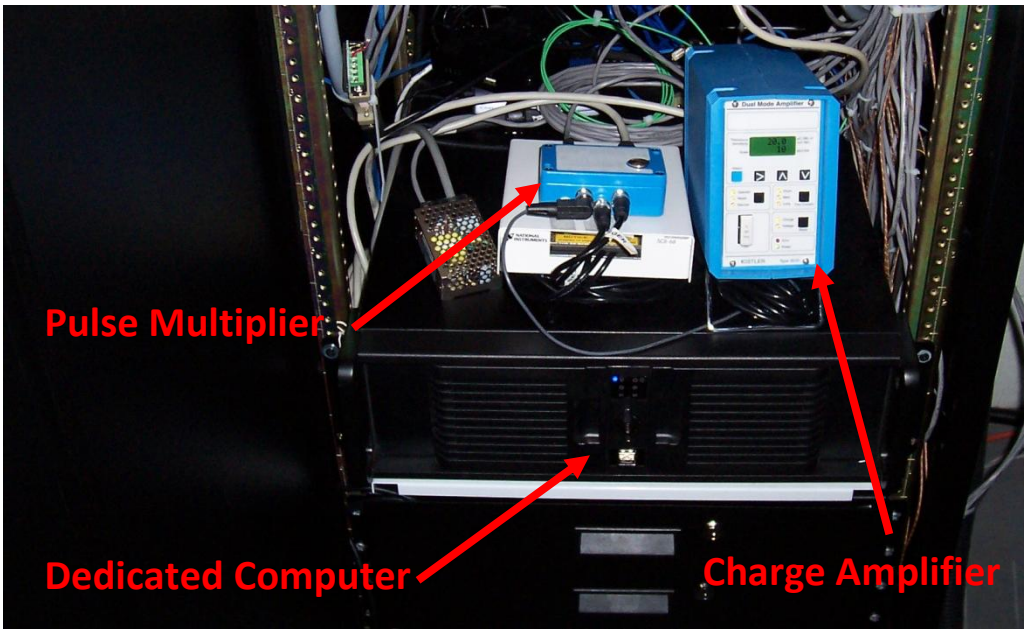

Figure 21. Engine Cylinder Pressure and Encoder Signal Conditioning Electronics in Test Cell Automation Cabinet

3.2.2 Program Design and Operation

Immediately following installation of the encoder and in-cylinder pressure transducer, programming of the software to record the high-speed data began using NI LabVIEW 2010, installed on the dedicated test cell computer and accessed using Microsoft Windows 7's remote desktop application. Each LabVIEW program contains two separate windows that aide in code programming and functionality. In this code, a "block diagram" is a graphical programming suite used to hard-wire program operations in a visual arrangement where signals move left to right and top to bottom. The block diagram is often easier to construct, organize, and troubleshoot than traditional code. The block diagram will be used in this work in order to describe exactly how the cylinder-pressure recording program functions. The "front panel" lets the programmer design the controls, displays what the user will use to run the LabVIEW program, and acts as the program's control panel.

The goal of the custom coded LabVIEW program is to provide the test cell operators with as much useful information as possible and to save the recorded data in a concise manner that streamlines post-processing and analysis. Specifically, the operators are able to observe a plot of in-cylinder pressure as the engine runs in order to view changes in engine operation immediately. In addition, real-time calculation and display of the engine's gross IMEP and gross indicated work provide immediate insight into the performance of both the engine and associated fuel combustion. Furthermore, the data recorded reflects an average of a pre-determined set of cycles of the engine in order to ensure accurate readings and to indicate a representative result. This averaged data is recorded in a format that can be used with Microsoft Excel software for further plotting and analysis.

In order to begin to describe the LabVIEW code, it is critical to explain exactly how it works in a high-level and logical manner. To summarize, the program first waits until the Kistler encoder measures TDC, then it counts crank angles as the engine continues to spin. The encoder outputs a digital signal that mimics a square wave as the engine runs (see Figure 22).

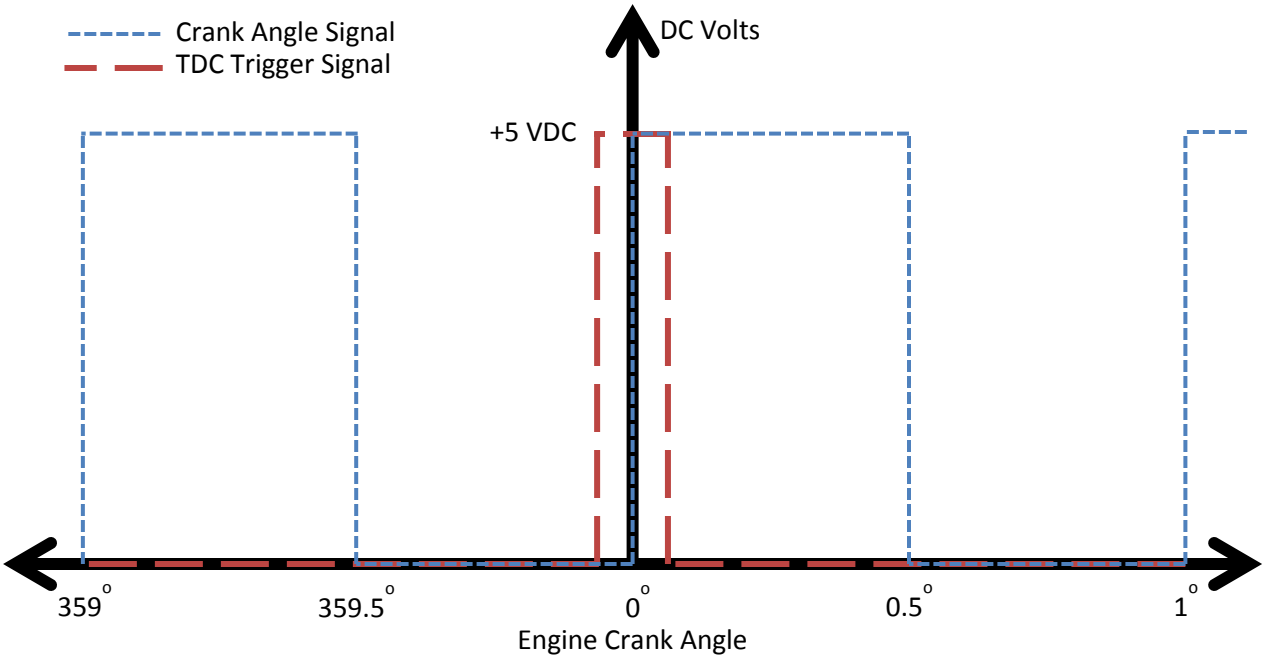

Figure 22. Diagram of Kistler Encoder Signal Sent to LabVIEW

While the code runs, it is recording the in-cylinder pressures at 0.5° angular intervals for multiple engine revolutions. This data is then transformed and scaled for both display and recording.

In reality, the system is separated into two separate codes that must run simultaneously in order for the overall program to function. The first code discussed is programmed to run on the FPGA chip of the NI card of the dedicated test cell computer. As discussed above, this chip has a sample rate of up to 200 kHz and is necessary in order to process the incoming encoder and pressure signals, which reach 43.2 kHz in the current configuration. This is the program used to detect TDC and angular signals from the encoder while using them to trigger measurements of pressure at the appropriate moment. The FPGA code then saves the crank angle and pressure data to specific locations in the computer's memory to be accessed by the real-time LabVIEW code discussed later in this section. To assist in clarity, a flow chart of the FPGA code is shown in Figure 23.

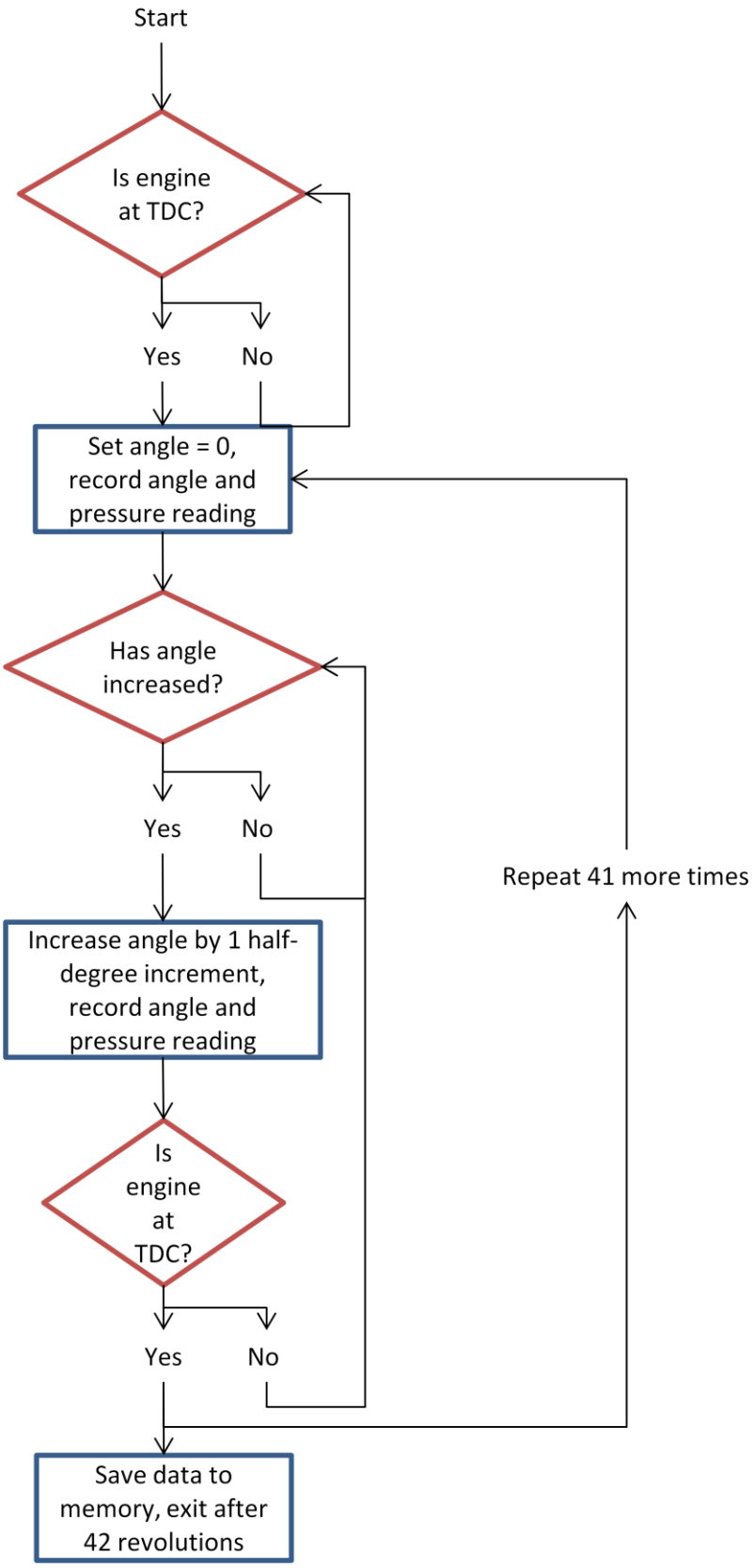

Figure 23. Flowchart of FPGA Code

The block diagram for the FPGA code is displayed in logical segments in Figures 24 though 28. The entire code runs only once, but saves pressure and angle data for 42 engine revolutions to ensure that 20 complete thermodynamic cycles are captured, starting from TDC when the expansion process is beginning. By using 20 averaged cycles, the relative standard error is less than 2% and provides a significantly smoother curve than the data from a single thermodynamic cycle. Use of more than 20 complete cycles does not dramatically decrease the relative standard error, but it rapidly increases program execution time. The two extra revolutions of data are needed as a buffer for the real-time code with the purpose of manipulating the data to always begin 180° before TDC on the compression stroke as explained later.

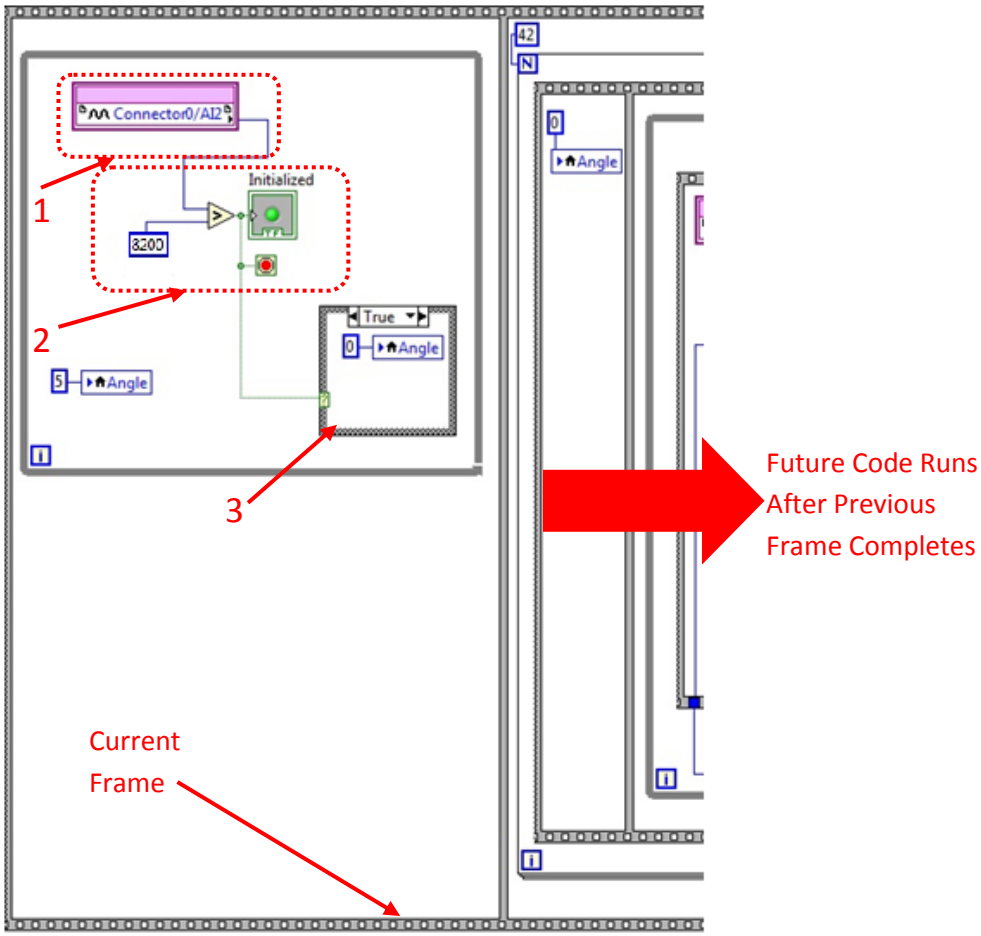

Figure 24. FPGA Block Diagram: Initializing at Engine TDC

The first segment of Figure 24 is a frame of a sequence used to find the first TDC reference after the FPGA code is initialized. A frame is a structure used in LabVIEW to help dictate the order in which events occur and are completed from left to right across the code. All of the actions in a frame (gray box in Figure 24) must occur before the code will move to the next frame. This is crucial as it serves as the starting point for the first revolution of angular counting. The first frame works by:

1. Reading in the pre-determined channel on the NI card, in this case Analog Input 2, to which the encoder's 5VDC TDC signal is wired. This channel sends out a bit value that corresponds to that voltage (3277 bits/volt).
2. The segment will continually loop until the voltage coming in from the encoder exceeds a cutoff voltage (8200(bits)/3277(bits/volt) ≈ 2.5VDC) to indicate that TDC has been reached. This voltage was chosen as a voltage halfway between the low and high signals of the trigger's square wave. This threshold prevents noise in the signal from causing a false trigger in the code.
3. If the encoder outputs the 5VDC signal, the appropriate angle of 0^o is set to the local variable called *Angle*, used later in the program in order to count to 720 half-degrees per revolution.

Following the completion of the first frame of the code (Figure 24), the next frame to the right (Figure 25) will begin to execute.

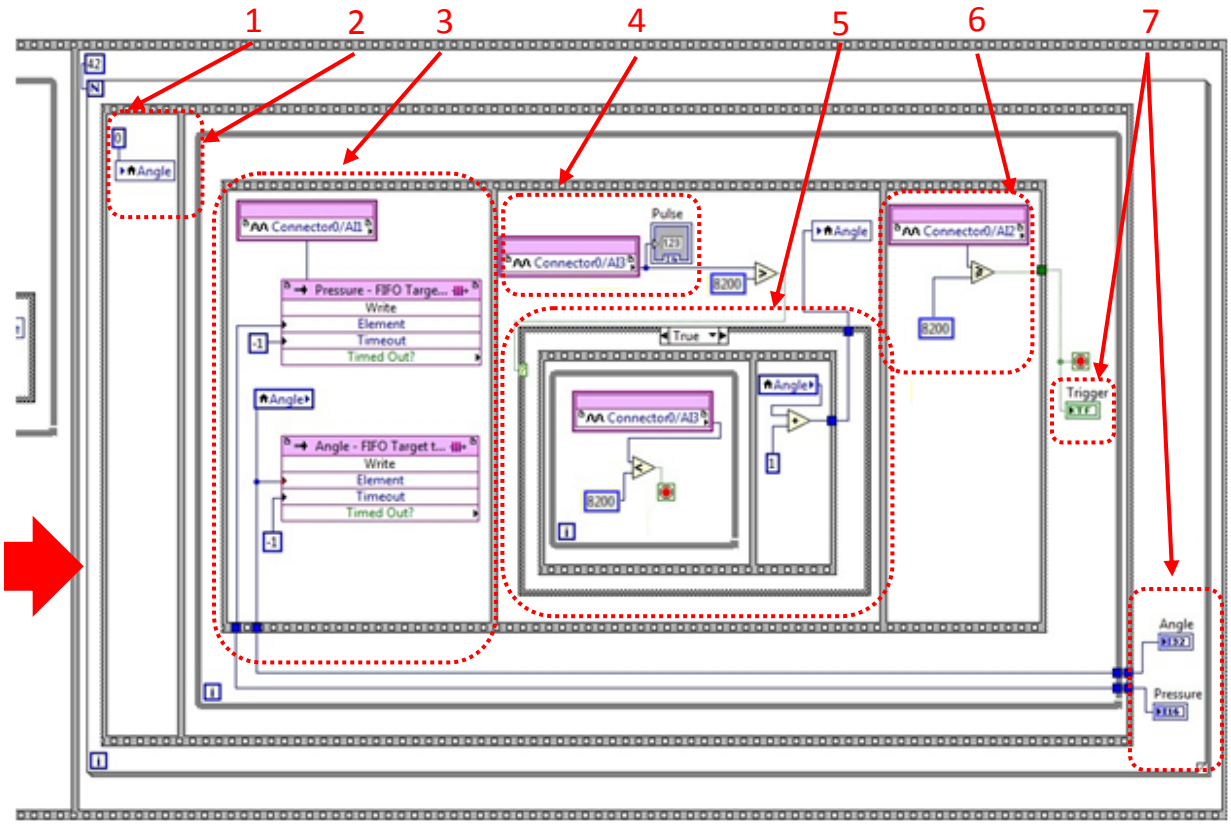

Figure 25. FPGA Block Diagram: Counts Angle Increments and Revolutions while Saving Signals

In the case of the second frame in the sequence, nested loops and sequence structures are needed in order to complete the counting, triggering, and saving process in the FPGA code. Following the completion of the second frame in this sequence, the FPGA code is complete and engine crank angle and pressure signals are stored to memory for convenient retrieval. The second frame works by:

1. Beginning with a for-loop that loops once per engine revolution. This loop is programmed to run for 42 engine revolutions as 40 complete engine cycles are desired for data. The two extra revolutions of data are needed as a buffer for the real-time code with the purpose of manipulating the data to always begin 180^{o} before TDC on the compression stroke.
2. The variable *Angle* is once again given a value of zero at the beginning of this small sequence. This is needed in order to indicate the beginning of a revolution at TDC. This point in the

program is first reached immediately following initial TDC reference from frame 1 in Figure 24 and is somewhat redundant as the variable's value does not change between the first and second frames in the FPGA code. However, after each revolution following initialization, this section of code is vital to ensure that the value stored to *Angle* is 0^{o} during the next engine revolution.

3. This frame is the beginning of a third nested sequence structure that executes once for every encoder signal rise or fall (once every 0.5^{o}) and is used to write the pressure signal from the charge amplifier and the corresponding value stored in *Angle* to specified memory locations using a First-In, First-Out (FIFO), Direct Memory Access (DMA) command. A similar command is used in the real-time code in order to retrieve this data.
4. Following the recording of the data for the current angle, the code moves to the middle frame in the sequence to wait for a rising or falling edge in the encoder's square-wave signal that is wired into Analog Input 3.
5. The current state of the signal (0VDC or 5VDC) is used to direct the case structure indicated by point 5. If the signal is above 8200 bits (~2.5VDC) then the case structure will run the code inside the "True" box. Otherwise, the code in the "False" box (Figure 26) will be executed. The true condition is designed to wait inside a while loop for the falling edge of the encoder signal that indicates a new angular position has been reached. Once a falling edge occurs, the while loop ends and the value stored in *Angle* is increased by one half-degree. Conversely, the false condition works in the opposite manner by waiting in a while loop for the rising edge of the encoder signal to increase the value in *Angle* by one half-degree increment.

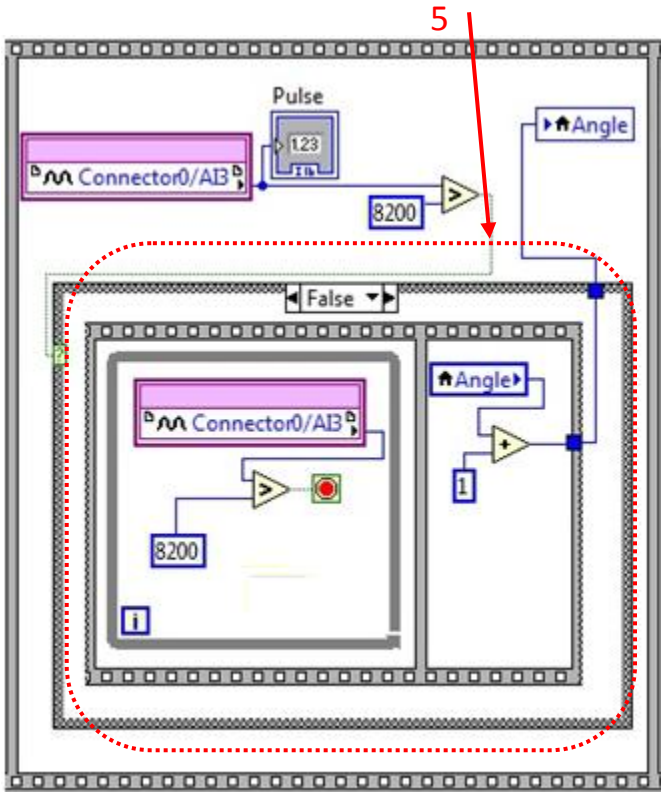

Figure 26. FPGA Block Diagram: False Case Structure

6. Now that the angle has increased, it is possible that the engine has once more reached TDC. The point of this frame of the sequence is to check the encoder TDC signal in Analog Input 2. If there is not any voltage, then the engine has not yet reached TDC and the sequence will restart to continue recording and counting angles. However, if the encoder signal is present to indicate engine TDC, then the while loop is stopped so that the sequence structure will return to point 2 in Figure 25 in order to begin recording a new engine revolution or end the program, depending on the current number of engine revolutions recorded.
7. To aid in program troubleshooting and for TDC alignment, the variable *Angle* and the pressure signal are wired into indicators to display these values on the FPGA front panel. In addition, the TDC signal is wired to a Boolean indicator light on the front panel that illuminates when the engine is at TDC. The code operates independently of engine speed since there are no timing

events. As a result, these indicators are useful for turning the engine by hand to check TDC (trigger light turns on) and for determining crank angles that correspond to important cycle events, such as the angles at which the Intake Valve Closes (IVC) and the Exhaust Valve Opens (EVO). The front panel for the FPGA code is shown in Figure 27.

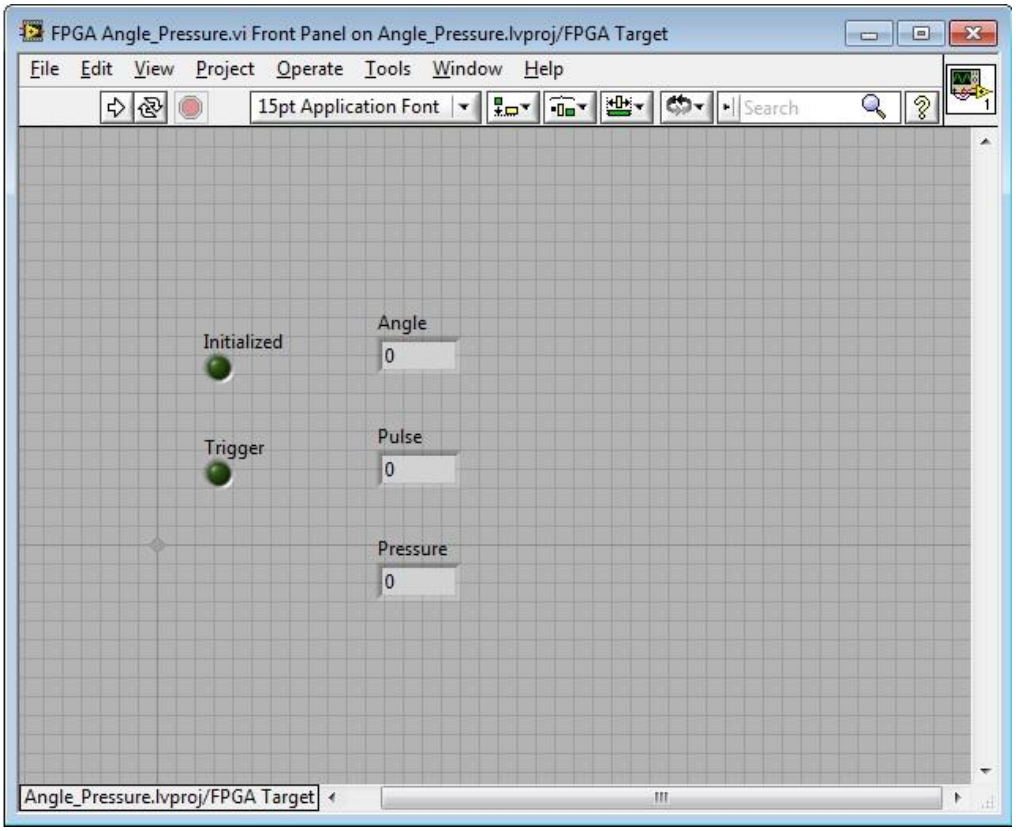

Figure 27. FPGA Front Panel: Indicators for Pressure and Angles

Once all of the frames of the FPGA code have finished running, the program has saved all engine crank angles and the corresponding pressure signals (as bits) to be read from memory. This is then converted into a pressure trace and subsequently available for saving to file by the LabVIEW program.

The real-time program contains the screen and controls used by the operator during execution. From the front panel, the user can watch live in-cylinder pressure traces along with IMEP and gross indicated work values. The front panel is shown in Figure 28 during operation with the pressure trace

plotted in red against an engine motoring curve in yellow. This curve indicates the pressure increase that occurs during compression and expansion in the absence of fuel injection and combustion.

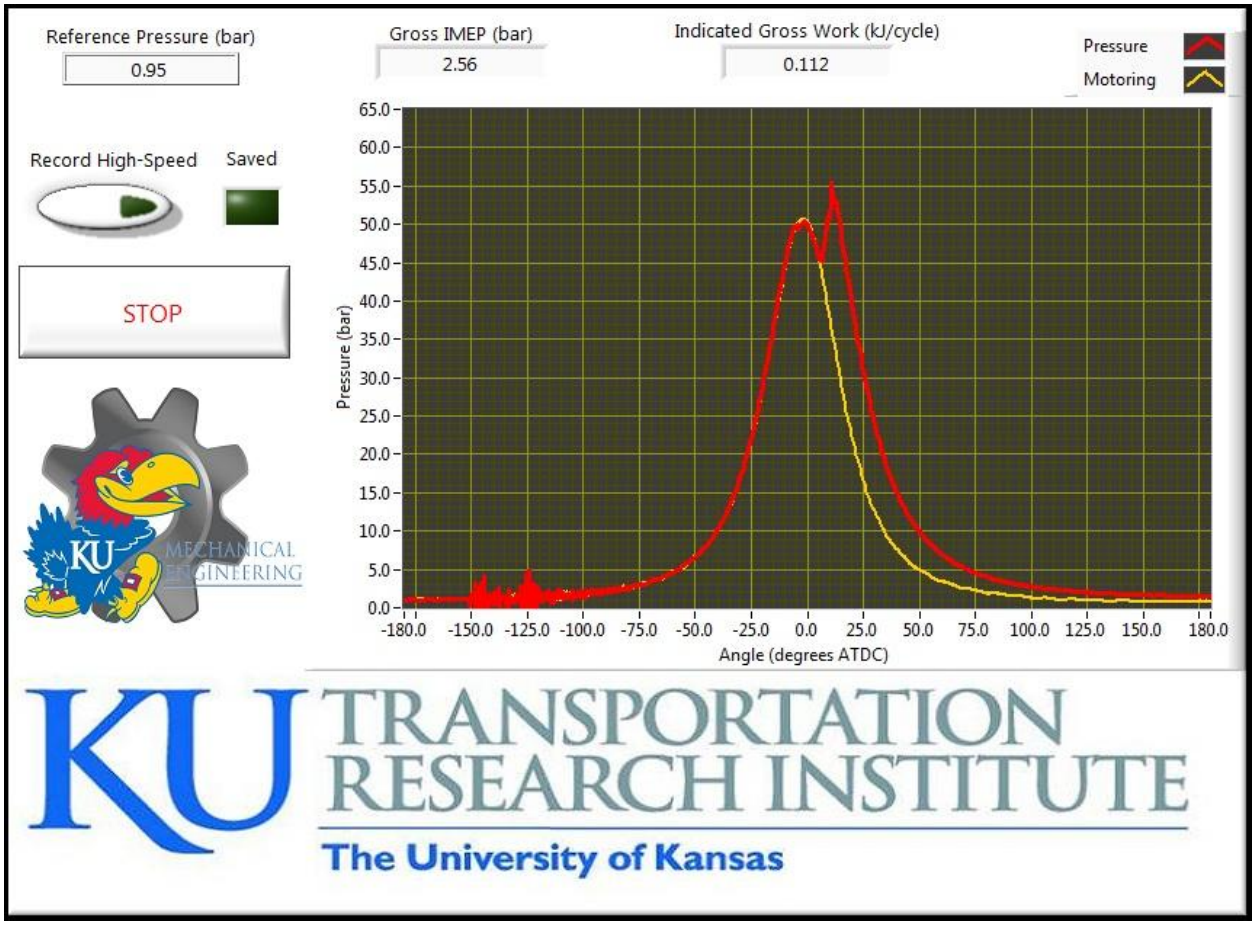

Figure 28. Real-Time Front Panel with Live Data during Test

The differences between the motoring and combustion curve (increases or decreases in pressure) can serve as visual indication of injection and combustion. For instance, the region of higher pressure for the combustion curve indicates that positive work is being done by hot gases on the piston. The motoring curve used in the display was taken by disarming the fuel pump while the engine was running and recording the pressure data. In order to look at specific points on the plot, it is possible to adjust the minimum and maximum values of the *x* and *y*-axis in order to zoom in on a specific area.

Pressing the switch labeled “Record High-Speed” on the front panel saves the angle-pressure data along with the gross IMEP and indicated gross work values. The user can elect to save the data to a file by specifying the file path and name (see ‘Choose or Enter Path of File’ dialog box in Figure 29).

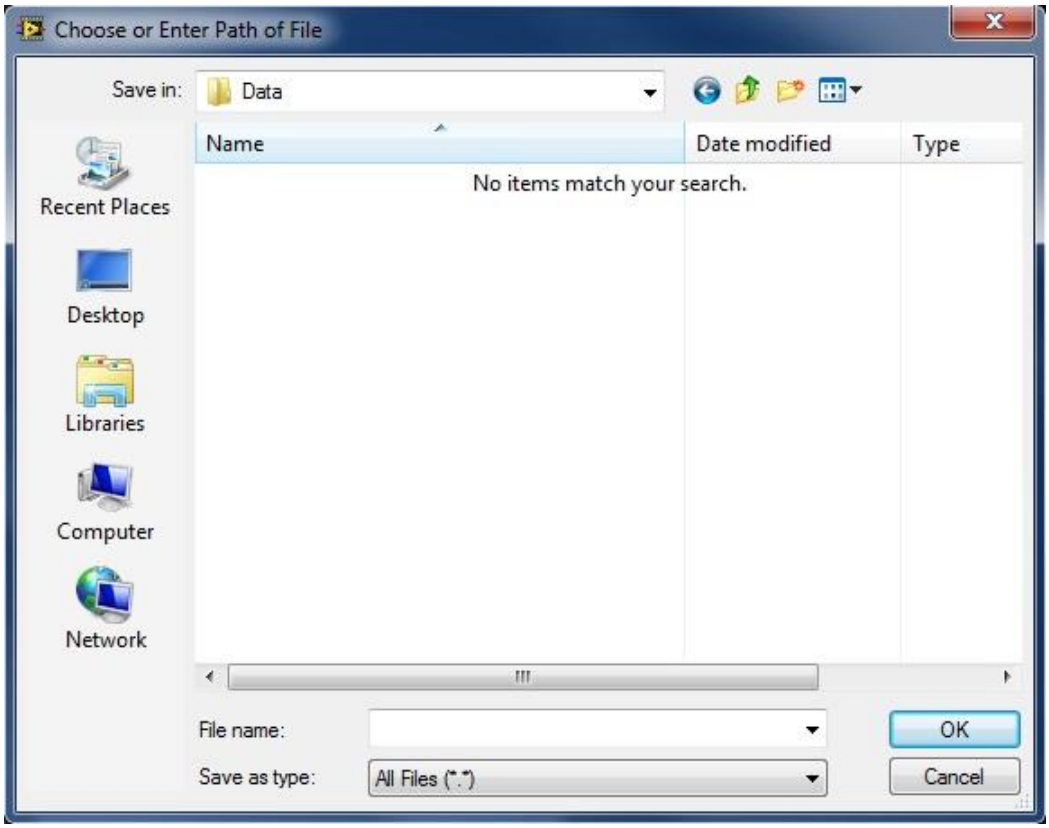

Figure 29. Choose or Enter Path of File, User-Defined Location and File Type for Data

The beginning of an output file in Figure 30 shows the indicated performance parameters and the beginning of the averaged crank angle, pressure, and volume data. Future upgrades will include the option of saving all data used to make the averages. Once a save is successful, the “Saved” indicator light will briefly blink. Pressing “STOP” will cause the program to shut down.

University of Kansas - Mechanical Engineering		
In-Cylinder Pressure System - 2011		
Gross Indicated Work (kJ/cycle)		
0.115		
Gross Indicated Mean Effective Pressure (bar)		
2.648		
Angle (degrees ATDC)	Pressure (bar)	Volume (m^3)
-180	0.950	4.573E-04
-179.5	0.938	4.573E-04
-179	0.947	4.572E-04
-178.5	0.926	4.572E-04
-178	1.112	4.572E-04
-177.5	1.118	4.571E-04
-177	1.124	4.571E-04
-176.5	1.090	4.570E-04
-176	1.139	4.569E-04
-175.5	1.173	4.568E-04
-175	1.173	4.567E-04
-174.5	1.167	4.566E-04
-174	1.035	4.565E-04
-173.5	1.002	4.563E-04
-173	1.026	4.562E-04
-172.5	0.974	4.560E-04
-172	0.965	4.558E-04

Figure 30. Real-Time Output File Sample

Similar to the FPGA efforts, the real-time code requires events and commands that happen in a specific order and, therefore, relies heavily on sequence structures. Due to this fact, the block diagram is wide and is best viewed in segments via Figures 31 through 39. The entire block diagram is contained within a while loop that is configured to keep running until the user presses the “STOP” button on the front panel. To aid in the understanding of the data manipulation, it is often helpful to refer back to the structure of the output file segment shown in Figure 30.

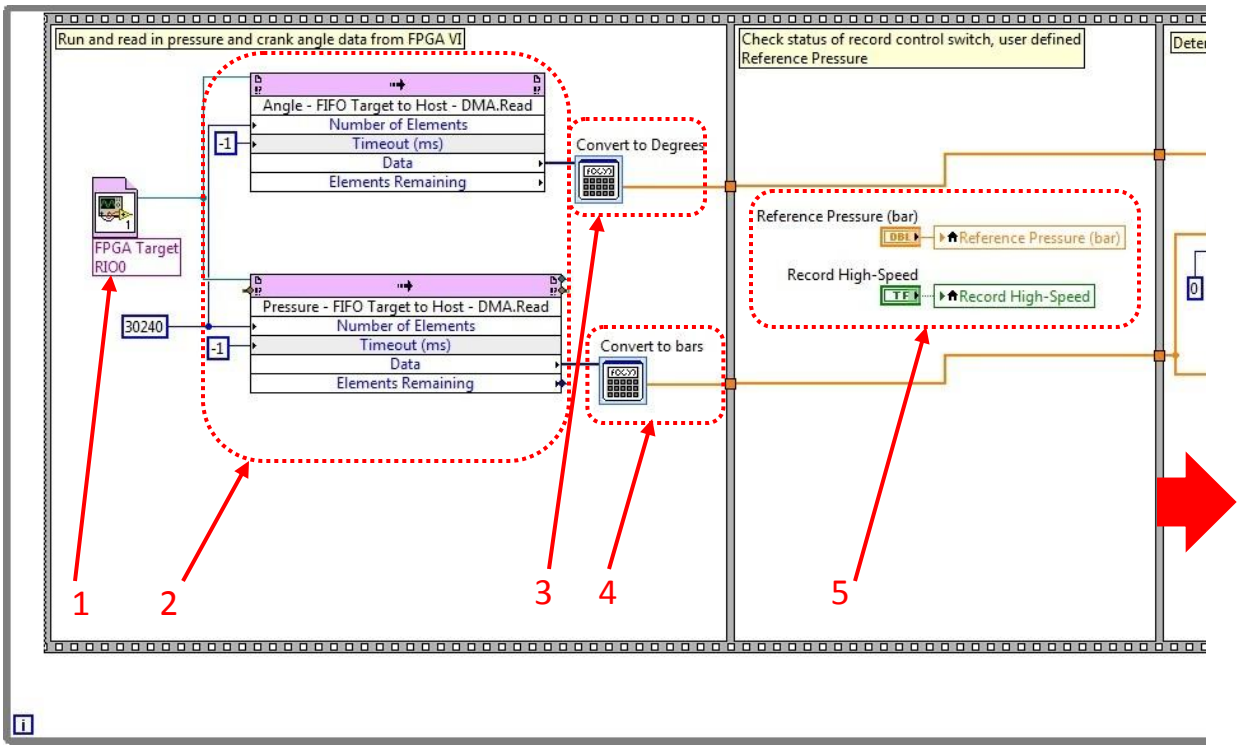

Figure 31. Real-Time Block Diagram: Read from Memory, Check Controls

In the first two frames of the real-time program, the code begins by running the FPGA code stored on the NI card (step 1). It then retrieves the recorded crank angle and pressure signals from their memory locations using the FIFO DMA. Read command (step 2). The values read from memory are immediately converted into numbers that are more useful. In particular, crank-angle values before conversion are indicated as half-degree integer values; e.g., Bottom Dead Center (BDC) of the piston corresponds to 360 half-degree increments with a full revolution equal to 720. In the "Convert to Degrees" *formula express* virtual instrument (VI) (step 3), the incoming angles are divided by two in order to depict the crank angle in actual degrees. Similarly, the pressure signal that was previously scaled from 0-32768 (2^{15}) and 0-10VDC is converted in another *formula express* VI (step 4) to bars using a collection of unit conversions and the Kistler pressure transducer calibration coefficients as follows:

Cylinder Pressure Conversion	$p(bar) = p(bits) \cdot 10\left(\frac{bar}{volt}\right) \cdot \frac{10}{32768}\left(\frac{volts}{bits}\right) = p(bits) \cdot \frac{100}{32768}\left(\frac{bar}{bits}\right)$	(6)

where p is in-cylinder pressure.

Then, the states of the user controls and inputs are checked following the first frame in the real-time sequence (step 5) and their values are stored to local variables to be used later in the program sequence. Specifically, the states checked are for the "Record High-Speed" button and "Reference Pressure" input. If the "Record High-Speed" button is pressed (true) the program will take action to prepare to save the data. If the save button is not pressed (false), the program will instead perform calculations to display the pressure trace data on the front panel.

The "Reference Pressure" input is required due to a fundamental characteristic of piezoelectric pressure transducers. This type of transducer can only be used to indicate a relative change in pressure. Since an absolute pressure is desired, a reference pressure is needed in order to compare and calibrate the relative pressure of the transducer. This can be done using two common methods [10, 11]. The first method of pressure referencing, or "pegging", is called inlet manifold referencing. To use this method, it is assumed that the pressure in the cylinder at piston BDC is equal to the intake pressure at that time. This requires the installation of a second pressure transducer in the engine intake and is a robust method for pressure referencing. The second method is called polytropic index pegging. In this method, a polytropic index (*n*) indicates an offset pressure that is believed to be the preferred method of calibration at high engine speeds where the cylinder pressure at bottom dead center may not equalize with the intake pressure [10, 11]:

Offset Pressure	$p_{off} = p_1 - \frac{(p_2 - p_1)}{\left[(V_1/V_2)^n - 1\right]}$	(7)

where p_{off} is the offset pressure, p_1, p_2, V_1, and V_2 are pressures and volumes at two known crank angles and *n* is the polytropic index.

In the future, additional studies for the determination of the preferable method for engine research at KU will be conducted. In the meantime, the Yanmar engine is already outfitted with an inlet pressure transducer that provides absolute pressures useful for inlet manifold pegging. Since engine

operation speed remains constant in the current setup, the user manually inputs the reference pressure by reading the information from the low-speed LabVIEW program. As advancements are made to the system and engine speed is allowed to change, it will become important for the LabVIEW code to read in the inlet pressure signal automatically. When this need arises, the code necessary to do so will go in this sequence frame and the pressure will be saved to the local variable *Reference Pressure* in the same fashion as the current user input. Now that the raw angle and pressure data has been read and user input states are known, the preparation of data for display and saving begins as illustrated in Figure 32.

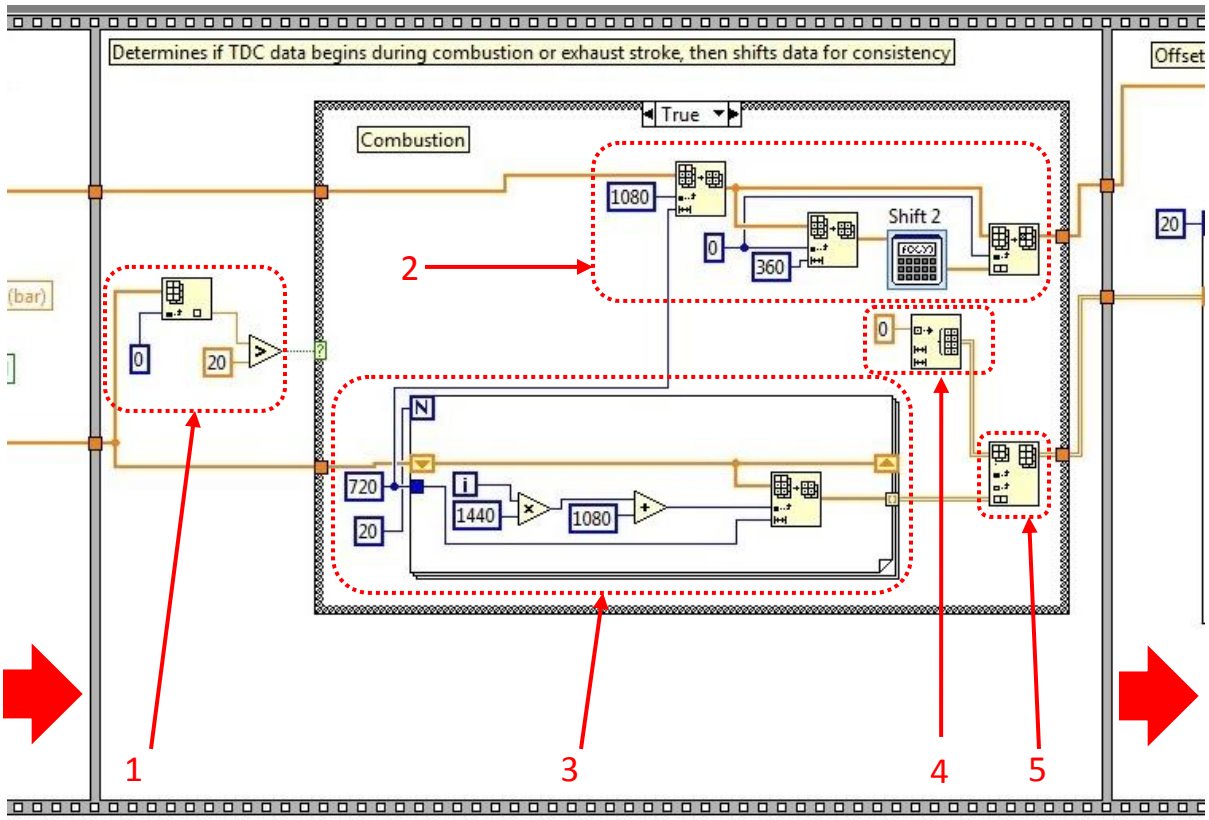

Figure 32. Real-Time Block Diagram: Angle and Pressure Data Shifting with True Case Specified

This frame of the real-time code is the first segment that begins performing the calculations using the two columns of measured angle and pressure data (degrees and bars, respectively) that each

contains 30,240 values. The purpose of this segment is to build a single column of 720 values for crank angle between -180^{o} to 180^{o} from TDC composed of only the compression and expansion strokes. For a non-turbocharged compression ignition engine, pumping losses are negligible[1] and are not measured in the program. However, once turbocharger installation is complete, it will be necessary to include the exhaust and intake strokes as pumping work becomes positive and is important to consider [1] . This data is already saved by the FPGA code discussed previously, and will be processed in much the same way as the compression/expansion data is currently. In addition to the column of crank angle, a two-dimensional array is constructed for each of the 20 compression and expansion strokes (recall that 40 complete engine revolutions are captured; hence, for a four-stroke engine this provides 20 combustion events from IVC to EVO) in a column of 720 pressure values to be used for combustion analysis in later frames. Each of the 20 pressure columns are aligned so that their rows correspond to the same crank angle. This segment operates by:

1. Removing the first value from the pressure column and performing a comparison between the measured pressure and an arbitrary cutoff pressure of 20 bars. This cutoff pressure is appropriate because the cylinder will not exceed this pressure during the exhaust and intake strokes, but will easily surpass this pressure during the data of interest (compression, combustion and expansion) where gross IMEP and gross indicated work are calculated. If the pressure is above 20 bars at TDC, then the engine has just finished the compression stroke of the cycle as the typical pressure at this point is approximately 50 bars (see Figure 28). If the pressure is below 20 bars at TDC, the engine is undergoing the exhaust-intake air exchange. The true or false Boolean value sent out by the “greater than” node determines how the case structure will function in order to shift the data so that future columns begin at the start of geometric compression at BDC (-180^{o}).

2. Utilizing an *array subset* function in order to pull data from the crank angle column at point 1080 that corresponds to 1.5 revolutions from the top of the data column. This was determined by comparing the pressure at TDC to the cutoff pressure of 20 bars and, therefore, to correspond to TDC in compression in the "True" case above. From this value at 1080, arrays of 720 values are removed in order to create a column that reads from 270^o to 180^o. The final column is desired to be from -180^o to 180^o (with TDC at 0^o) so the angles from 270 to 359.5 are removed using another *array subset* function in order to be subtracted by 360 and recombined with the 0^o to 180^o column to form a single column from -180^o to 180^o that is paired with the compression, combustion and expansion pressure data.
3. Containing a loop that runs 20 times for each thermodynamic cycle. As the loop runs, the loop counter "I" increases. This counter is used with an *array subset* function in order to break the long pressure data column into 20 segments that each represents the geometric compression (-180^o to 0^o) and expansion strokes (0^o to 180^o). The counter is multiplied by 1440 because each thermodynamic cycle includes two engine revolutions, or 1440 data points given the current half-angle encoder setting. For the "True" case in Figure 32, the appropriate data initially begins at the 1080^{th} value in the initial column. Since each of these 20 segments contains 720 values, this constant determines the length of the array segment removed in the loop. For the "False" case structure, pictured in Figure 33, the desired crank angle and pressure values begin at the 360^{th} point rather than the 1080^{th}. This is because the initial pressure was determined to be TDC just before the intake stroke, or only 180^o (360 data points) before the desired beginning of the compression stroke.

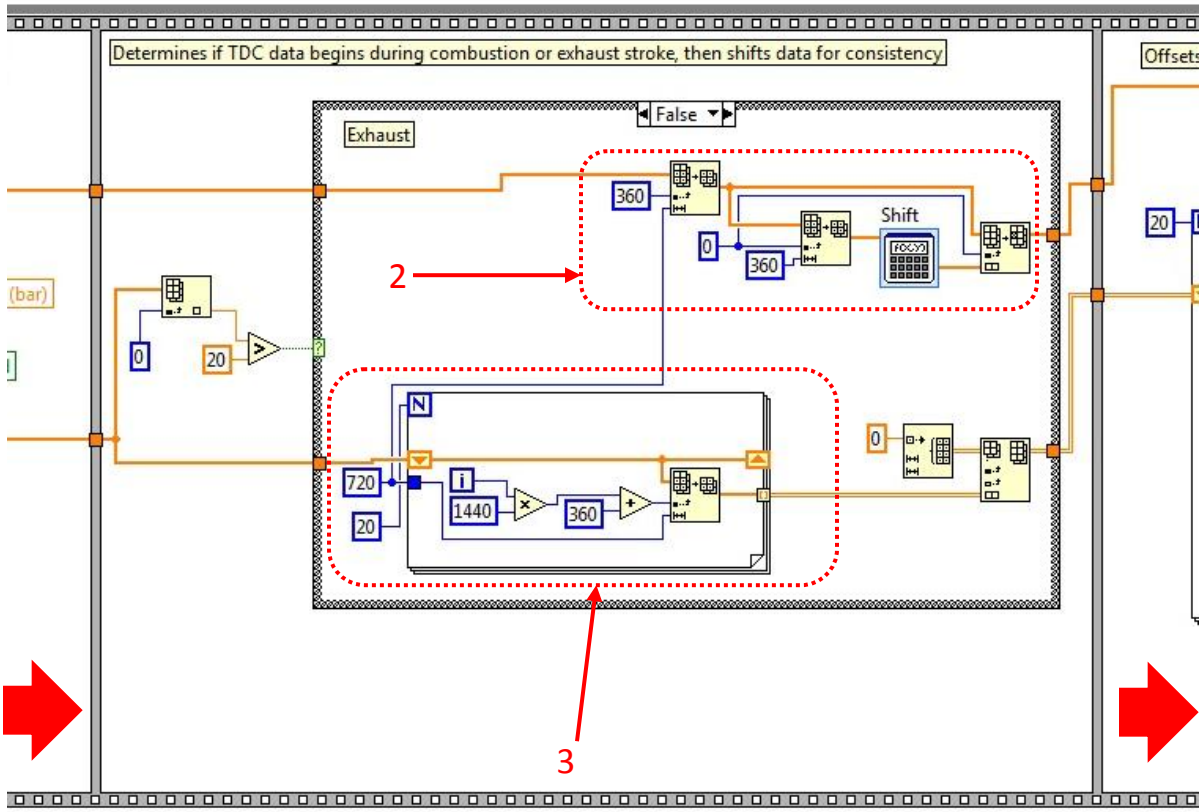

Figure 33. Real-Time Block Diagram: Angle and Pressure Data Shifting with False Case Specified

4. Utilizing an *initialize array* function in order to create a blank array that will store the 20 columns of pressure data points.
5. As a result, pressure data from the 20 thermodynamic cycles (four stroke: two revolutions equals one thermodynamic cycle) are stored in the newly created array using the insert into array function. The array is now 20 columns wide and 720 rows long and will be used later in order to determine a representative average pressure curve.

At this point, pressure data is still represented the relative pressures sent from the Kistler transducer and charge amplifier and have not been altered by pegging methodology discussed earlier. It is in the fourth segment of the real-time sequence structure, shown in Figure 34, where the reference pressure is applied to the recorded pressure data.

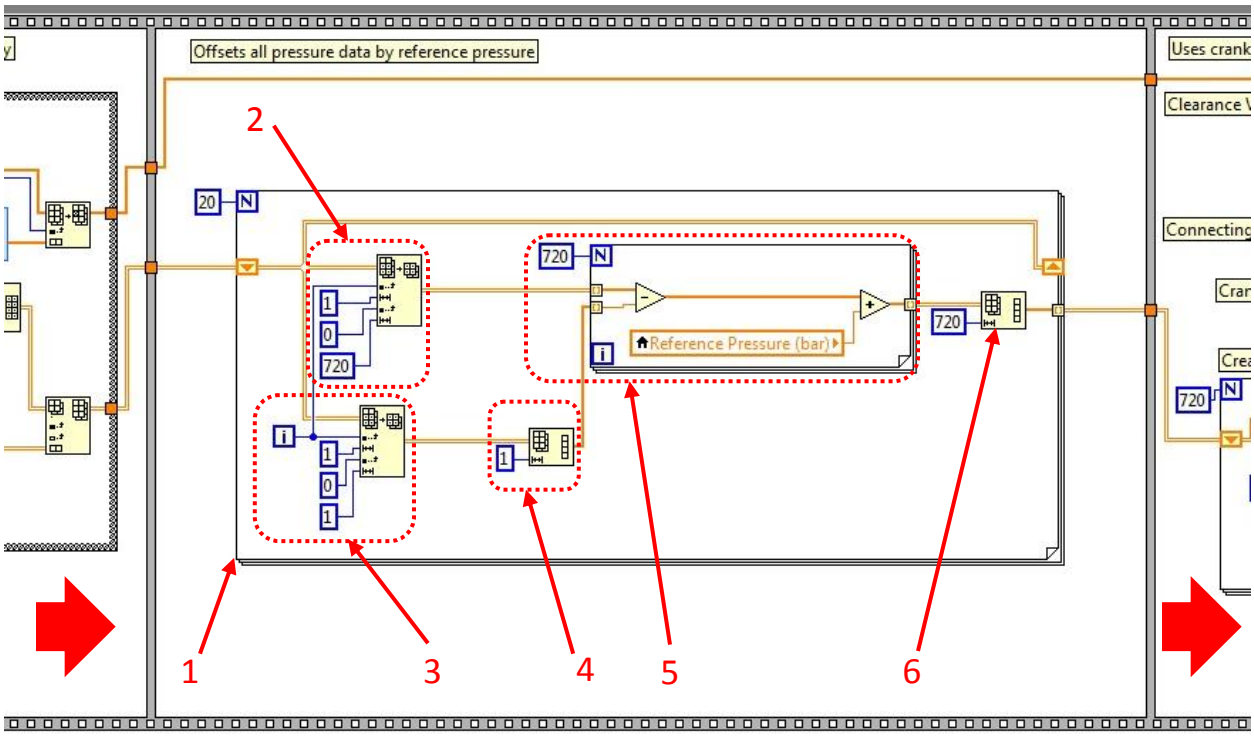

Figure 34. Real-Time Block Diagram: Offset Pressure Data by Reference Pressure

The reference pressure, as stated earlier, is necessary in order to create an absolute cylinder pressure for the in-cylinder pressure data. The frame in Figure 34 is where the reference pressure is read from the local, user defined variable and added to all of the pressure data. This is accomplished by:

1. Bringing the pressure array (20 columns of 720 values) into a loop in order to run 20 times, once for each column of data.
2. For each iteration inside the loop, the data values in each column are removed using an *array subset* function. The iteration counter is used to dictate which column of data is removed.
3. Similarly, the first data point of each column (corresponding to the pressure value at 180^{o} before TDC) is removed using a second *array subset* function. This value is typically negative as it is slightly lower pressure than ambient, where the crystal in the transducer is not exposed to

high pressure and outputs a negative value. Therefore, it is desired to offset the data to ensure that the relative pressure is 0 bar at BDC for every column of pressure data. This is important because the reference pressure (a positive value) will be added to this relative pressure (previously negative, now zero) to create the desired absolute pressure at BDC and have all other pressure values shifted accordingly.

4. Using the array received, a *reshape array* function is used to convert the two-dimensional array into a one-dimensional array of single length (aka a single value). This single value is the BDC pressure from the respective engine cycle dictated by the loop iteration counter (from pressure column 0-20). This value (a negative pressure) is then sent into the for-loop in order to be added to its respective pressure data column. The pressure at TDC must be removed from the array so that it can be applied to the entire pressure profile as an offset to each data point of each column, it is not possible to do this using the two-dimensional array.
5. In this loop, the negative relative pressure from the original BDC data is subtracted from the column of 720 data points. At this point, the pressure at BDC before compression reads zero bar. Immediately after the offset from the original BDC value, the reference pressure is read from the *Reference Pressure* local variable and added to the entire column in a similar fashion so that the column now indicates the reference pressure as the assumed pressure at BDC. This methodology repeats the description of the inlet manifold referencing method discussed previously.
6. As the data leaves the 720-iteration for-loop, it is automatically converted back into a two-dimensional array by the for-loop; however, this is not the desired structure, so the array is immediately sent through a *reshape array* function in order to create a single column of data for each individual cycle pressure curve. As the data leaves the 20-iteration for-loop, a two-dimensional array is automatically built by the loop that is composed of the 20 columns of the

720 pressure values from each compression and expansion event recorded. This is very similar to the array that entered the 20-iteration loop, except that all values at -180° (BDC) begin at the reference pressure. This is vital for the pressure averaging that occurs in the next frame of the real-time block diagram.

In addition to developing values for engine crank angle and pressure, it is useful to calculate instantaneous cylinder volume for calculation of gross indicated work and IMEP. Figure 35 depicts the method in which cylinder volume is calculated, and how the 20 columns of pressure data are averaged into a single pressure column with 720 averaged data points.

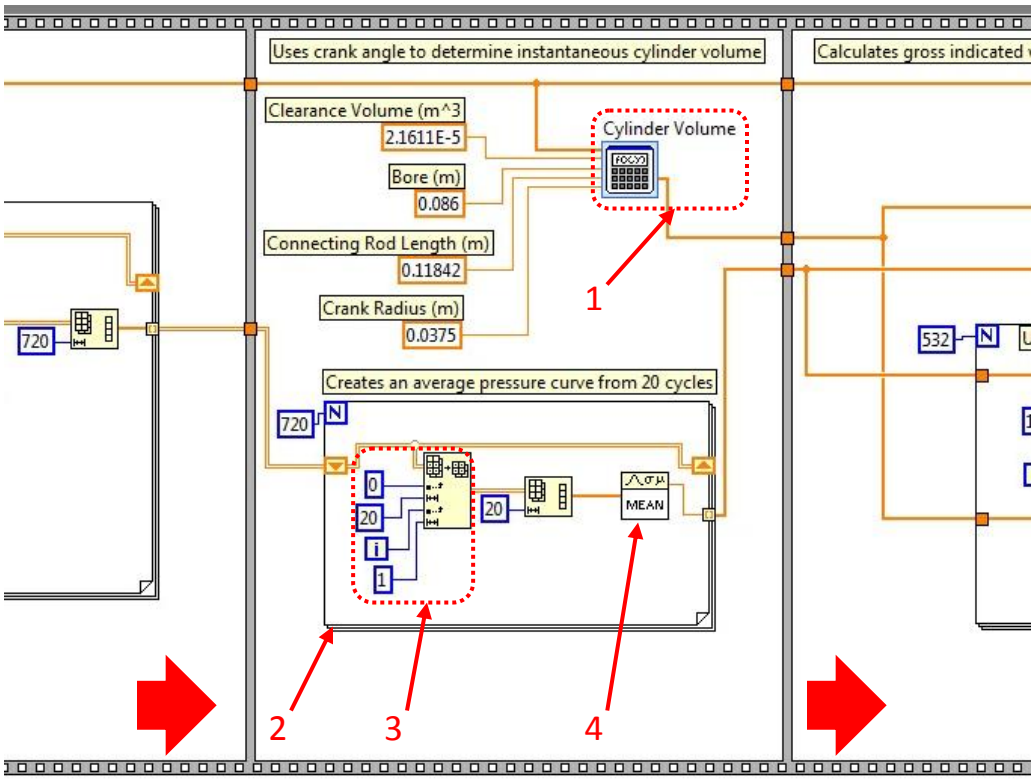

Figure 35. Real-Time Block Diagram: Instantaneous Cylinder Volume and Pressure Averaging

In this figure, the flow is as follows:

1. Instantaneous cylinder volume is dependent on geometric properties of the engine and the angle of the crankshaft. The properties needed are cylinder clearance volume, cylinder bore, connecting rod length, piston pin offset (zero for this engine), and crank radius. The incoming *crank angle* array, with its single column of 720 values, is input into an *express formula* VI along with the constant engine properties. The instantaneous cylinder volume is calculated using the following equation [1] and is output as an additional array with 720 volume calculations to correspond with the measured crank angles:

Instantaneous Cylinder Volume	$V = V_c + \left(\frac{\pi \cdot B^2}{4}\right)\left\{l_{cr} + r_c - \left[r_c \cdot \cos\left(\frac{\pi}{180} \cdot \theta\right) + \sqrt{l_{cr}^2 - r_c^2 \cdot \sin^2\left(\frac{\pi}{180} \cdot \theta\right)}\right]\right\}$	(8)

where V is instantaneous cylinder volume, V_c is cylinder clearance volume, B is cylinder bore diameter, l_{cr} is the length of the connecting rod, r_c is the crank radius, and θ is the crank angle.

2. In addition to calculating volume, this frame creates the average pressure profile corresponding to one compression, combustion, and expansion event using the 20 measured pressure curves (two-dimensional array, 20 columns wide by 720 rows long). This is accomplished in a 720-iteration for-loop that averages the 20 readings at each interval of crank angle.
3. An *array subset* function removes each of the individual rows and outputs a single row (converted into a one-dimensional array of 20 values in columns) as the for-loop continues. The iteration counter is used to control which row is removed.
4. The mean of each row of pressure readings that corresponds to each crank angle is calculated using an express subVI. The single mean value is wired out of the for-loop where a new array is automatically created for the averaged pressure profile.

At this point in the code, three single-column arrays exist. The first is a column of engine crank angles from -180° to 180°, separated by 0.5° increments. The second column is comprised of the average pressure profile, created by averaging 20 thermodynamic cycles to smooth out the curve and minimize uncertainty. Originally, the program calculated the average for ten cycles; however, changing the average to 20 cycles lowered the standard deviation by about 50%, to approximately 1 to 2% during the combustion process. The final column is the instantaneous cylinder volume that corresponds to the measured crank angles. This column is used for calculation of gross indicated work and gross IMEP. These calculations are performed in the real-time LabVIEW code segment shown in Figure 36.

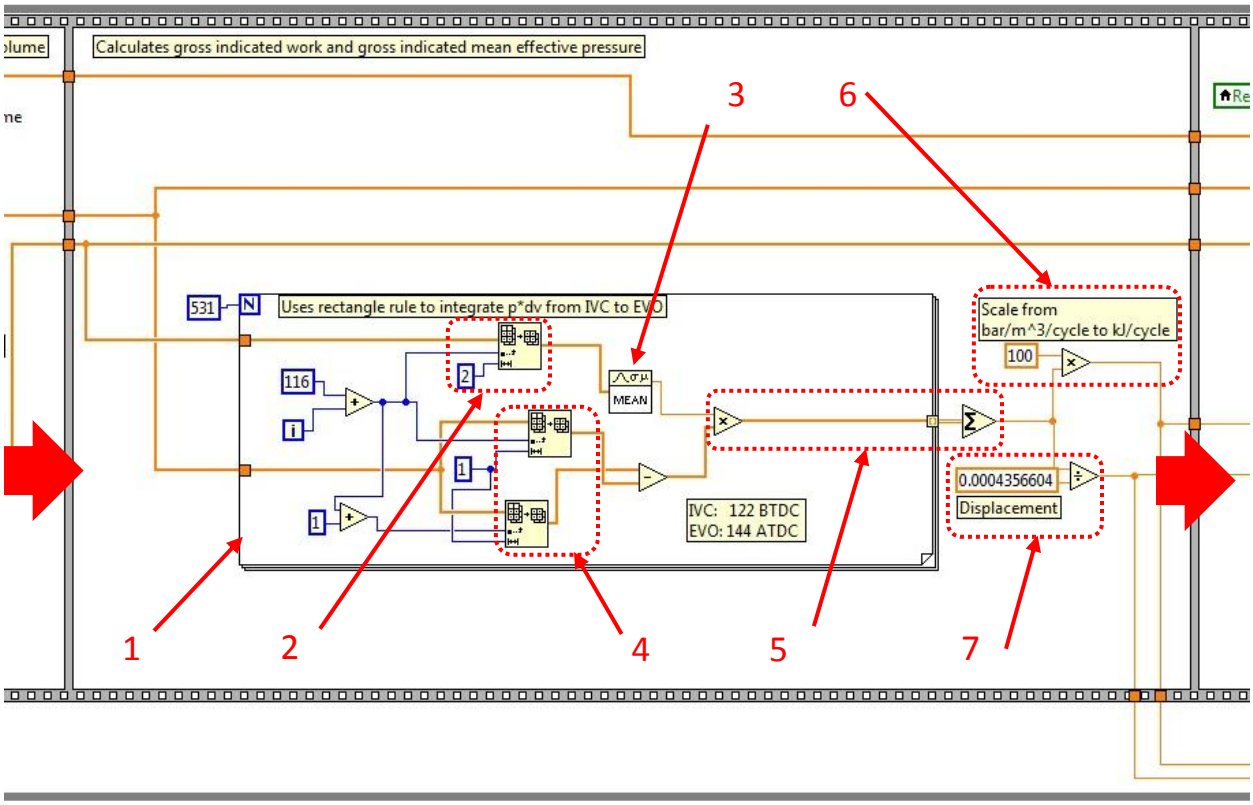

Figure 36. Real-Time Block Diagram: Calculating Gross Indicated Work and Gross IMEP

In order to perform the calculation of gross indicated work and gross IMEP, Equations 1 and 4 must be used. Even though LabVIEW contains integration express VI's, hard-coding of the integration

process is preferred in order to yield a complete understanding of the fundamentals taking place in the engine with regards to changing pressure and volume during combustion. While this adds in organizational complexity on the block diagram, only necessary calculations are performed. For many express VI's, there are additional functions that are not necessary in this case, and which could add to computational burden. The calculations for these two important performance parameters are performed using the rectangular rule [46]:

Rect. Rule	$W_{i,g} = \int_{V_{IVC}}^{V_{EVO}} p \cdot dV$ $\approx (V_2 - V_{IVC}) \cdot \frac{p(V_2) - p(V_{IVC})}{2} + (V_3 - V_2) \cdot \frac{p(V_3) - p(V_2)}{2} + \cdots + (V_{EVO} - V_{n-1}) \cdot \frac{p(V_{EVO}) - p(V_{n-1})}{2}$	(9)

where V_1, V_2, V_3, V_{n-1}, and V_{EVO} are volumes at intervals between IVC and EVO and $p(V_{IVC})$, $p(V_2)$, $p(V_3)$, $p(V_{n-1})$, and $p(V_{EVO})$ are corresponding pressures at those intervals.

The rectangular rule is constructed into the code as:

1. A for-loop calculates the area of each rectangle under the pressure curve from IVC (at 122° before TDC), to the angle at which the exhaust valve opens (EVO at 144° after TDC) as needed for Equation 1 and 4 in order to represent work done during the compression, combustion and expansion strokes (gross). For the crank angle, pressure, and volume arrays, these events are separated by 532 data points (266°); therefore, based on Equation 9, the for-loop runs for 531 iterations.
2. The pressure used to calculate the area of the trapezoids is comprised of an average between two points. This average is calculated each time the for-loop runs and is found by using an *array subset* function wired to the loop iteration counter in order to provide the pressures at the current and subsequent angles.
3. The two pressures from the *array subset* function are now averaged.

4. In addition to the average pressure, the change in volume is needed to compute the integral approximation. This is found using two *array subset* functions that return the volume for the current and following angles respectively. The volume from the current angle is subtracted from the next angle in order to determine the difference. During compression, this yields a negative value as the cylinder volume is getting smaller resulting in negative values for work and IMEP. This can be described as negative work that must be done to compress the inlet air mixture. During expansion, the difference in volume becomes positive indicating that the gas is now performing work on the piston as it combusts and expands. The fact that the pressure is higher during expansion makes the overall gross indicated work and gross IMEP values positive.
5. Using the pressure average derived from two readings at separate angles and the corresponding change in volume between those angles, the area of the trapezoid is calculated for each data point as the loop runs. Following completion of loop execution, the trapezoidal areas are summed up in order to complete the integration process.
6. The resulting value is scaled to output the gross indicated work in kJ/cycle and is both displayed and saved to a file.
7. In addition, this value is divided by the engine displacement volume and scaled in order to yield a gross IMEP value in bar for the engine. This value is also displayed and saved.

All of the desired crank angle, pressure, volume, and indicated performance parameters are now calculated. The remainder of the real-time LabVIEW code is devoted displaying the pressure versus crank angle plot, and the indicated performance parameters while saving the angle, pressure, volume, and performance parameters to a file. This process for saving the data is shown in Figure 37.

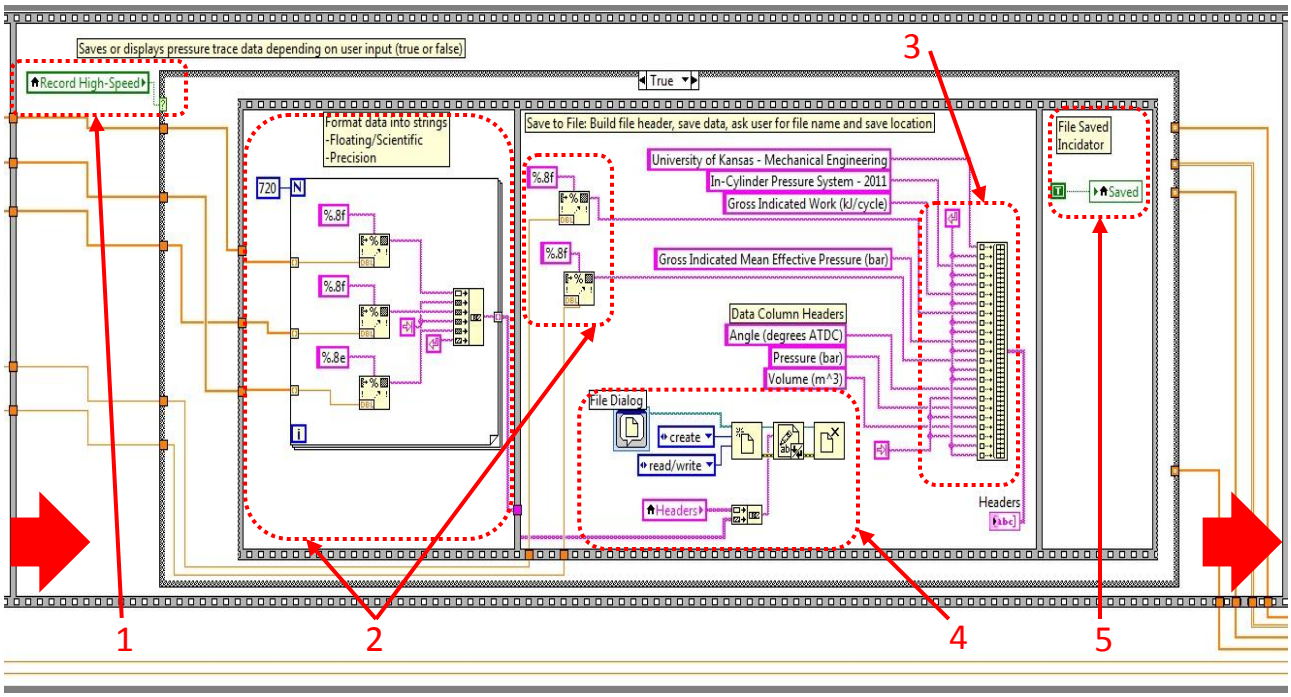

Figure 37. Real-Time Block Diagram: Save Data to a File

When the system operator wants to record data and presses the "Record High-Speed" switch, the local variable *Record High-Speed* receives a saved value of "True" (occurs earlier in the program shown in Figure 31). This causes the code to reach the segment shown in Figure 37:

1. The value saved to *Record High-Speed* is read every time the program repeats (every 42 rotations). If the value is "True", then the code in the "True" case structure is executed.
2. The incoming data is converted into strings and formatted for saving in the output file. The crank angle, pressure, gross indicated work, and gross IMEP are saved as floating point data with eight decimals of precision, while the instantaneous volume is saved in scientific format. Each have eight digits of precision because of relatively small values and truncation is possible during post processing with Microsoft Excel. The strings of angle, pressure, and volume are concatenated into a single array of strings that is three columns wide and 720 rows long.
3. A header is created to be written to the top of the output file using string constants. These constants are divided by return characters and tab characters for separation in the output file.

Included in the header are the calculated values for gross indicated work and gross IMEP. The bottom of the file header includes column names that will be above the angle, pressure, and volume columns in the output file. The header is written to local variable, called *Headers.* Future upgrades to the program will include calculated values for net IMEP and net indicated work, to be used to calculate net engine efficiency parameters.

4. The *File Dialog* asks the user what path and filename to save the new file under. *The create file, write to file, and close file* functions create the file, write the header and three data columns, and close the file, respectively.
5. Following a successful save, the "Saved" indicator light blinks once. The saved file can now be opened to access the results.

The default action of the program is to display the data and indicated parameters on the main screen until the "Record High-Speed" button is pressed. Therefore, a value of "False" is stored to *Record High-Speed* with the associated case structure shown in Figure 38 executed.

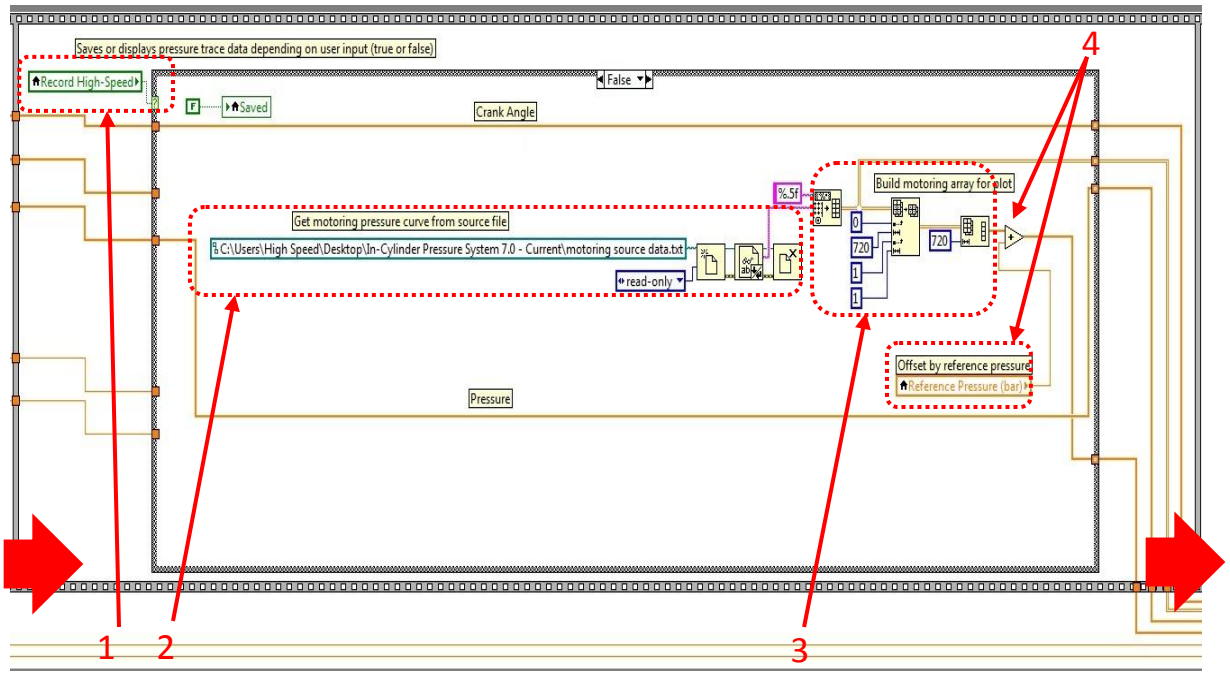

Figure 38. Real-Time Block Diagram: Display Pressure Profile and Indicated Performance Parameters

This segment of code retrieves a previous set of motoring curve pressures to plot alongside the active combustion data to serve as visual comparison between combustion and non-combustion (motoring) behavior. This data was recorded using this program and was collected by selecting save immediately after the engine's fuel pump was disarmed while the engine was running at full speed. It prepares this data by:

1. First, the "Record High-Speed" switch must be inactive so that the "False" case structure code executes.
2. The *open file, read file,* and *close file* functions are used with the motoring source code path selected. To aid in the calculation within this frame, the BDC offset value was performed in the creation of this source file in order to set the pressure at the beginning of the compression event to zero bar. This will be used to better synchronize the pressures of the motoring and combustion traces for display.
3. The data is passed to a *spreadsheet string to array* function that converts the individual spreadsheet values for crank angle and pressure into a two-dimensional array formatted as floating point with five digits of precision. The pressure data is removed from the motoring data array using an *array subset* function and formatted into a single column of data that is 720 values long.
4. The *Reference Pressure* is added to the column so that compression stroke of the motoring curve and the real-time combustion curve will coincide.

Finally, the code performed in the while loop in the real-time block diagram ends with the last frame in the sequence structure and the plotting of calculated data. The code for this section is shown in Figure 39.

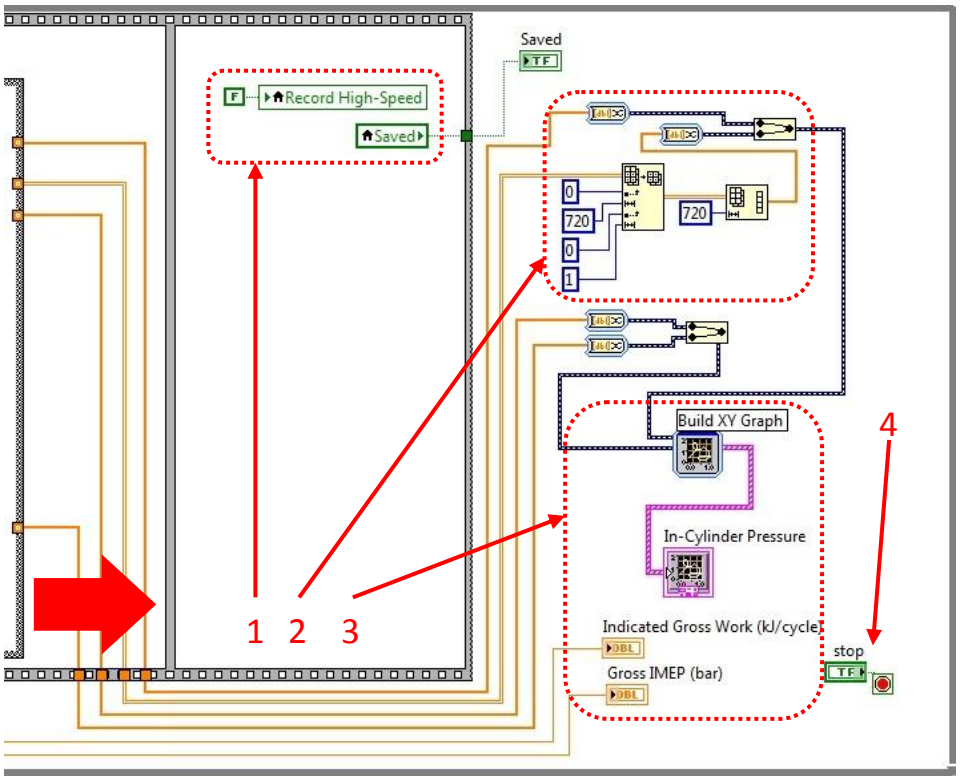

Figure 39. Real-Time Block Diagram: Displaying Pressure and Indicated Performance Data

The code in this segment resets the local variable for the save function and, if the user has not elected to save the data, takes the pressure and crank angle arrays and formats them for plotting in an XY graph while displaying the gross indicated work and gross IMEP values. In the future, net indicated work and net IMEP will be included. This occurs in the code as follows:

1. The end of the sequence has been reached so the local variable *Record High-Speed* is reset to a "False" value in order for the program to automatically display data. In addition, if the data was saved during this iteration of the main while-loop, the "Saved" indicator light is wired to blink via a connection with the *Saved* local variable.
2. The crank angle data from the motoring curve source code is selected from the associated array and resized using the *array subset and reshape array* functions in order to combine it with the measured crank angle data. This is then wired into the X-input of the XY graph creator.

3. The arrays for motoring curve pressure and real-time pressure data are combined and wired into the Y-input of the XY graph creator.
4. The stop button on the front panel is wired in order to stop the all-encompassing while loop. Pressing the stop button will shut down the program.

After reaching this point in the code, the program returns to the beginning of the sequence structure and continues displaying and saving data until the program is stopped by the operator. Program speed is dependent on engine speed as 42 revolutions must occur before enough data is available for averaging. Therefore, at 3600 RPM the engine rotates at 60 Hz, meaning that 42 revolutions occur in 0.7 seconds. Due to this fact, the fastest possible iteration speed is once every 0.7 seconds. This may seem slow, until considering that during this time frame over 32,000 measurements are taken for both engine crank angle and pressure while the calculations in the real-time VI are performed.

3.3 System Validation

In order validate the effectiveness of the system, three different fuels were tested in the single-cylinder test cell. They include ULSD, Used Cooking Oil (UCO) biodiesel produced by the KU chemical and petroleum engineering department, and jet propellant number 8 (JP-8). ULSD serves as a control fuel for the test since the engine and injector is designed to utilize this specific fuel. The choice of UCO biodiesel revisits the work presented in Chapter 2 in order to obtain a better insight into fuel properties on performance and emissions. JP-8 is added to the mix in order to investigate the feasibility of using this fuel in diesel engines as a part of the United States military's Single Fuel Forward policy. This policy involves a simplification of battlefield logistics through use of a single fuel across all combustion platforms [16, 18]. Fuel chemistry differences between JP-8, biodiesel, and ULSD will result in different combustion characteristics affecting both performance and emissions. Measured and literature properties for these different fuels are indicated in Table 10 [47].

Table 10. Measured and Found Literature* Fuel Physical Properties [47]

	ULSD	UCO Biodiesel	JP-8
Density (298.15K) (kg/m^3)	831	878	801
Kinematic Viscosity (cSt)	2.268	4.845	1.288
Dynamic Viscosity (cP)	1.885	4.251	1.031
Cetane Number	42.3*	52.8	44.5*
Energy Content (kJ/kg)	41530*	36210*	42700*

In the following sections, the resulting differences in fuel consumption, emissions, and most-importantly, in-cylinder pressure traces along with indicated performance parameters will be directly compared with expected trends present in literature.

3.3.1 Test Methodology

In a manner similar to the biodiesel tests in Chapter 2, the Yanmar engine is subjected to five different loadings; from 0% to 100% of generator rated loading for each fuel. Since the rated capacity of the electric generator is around 80% of the rated power output of the engine, the five load settings roughly correspond to 0%, 20%, 40%, 60%, and 80% of rated engine load. Data for each point was taken following ample time for the engine's downstream exhaust temperature to reach steady state conditions defined by a stabilized exhaust temperature (less than 1% change in measured reading over a minute). Once steady state conditions are reached, five minutes of emissions of CO, CO_2, NO, NO_2, and HC data are recorded using a Sensors, Incorporated Semtech-DS Mobile Emissions Analyzer at a frequency of one sample per second. Midway through the recording of the emission data, two minutes of performance data is taken at a frequency of ten readings per second. Concurrently, the in-cylinder pressure data is recorded that is composed of an average of 20 thermodynamic cycles, or 40 engine revolutions.

3.3.2 Results and Discussion

As shown in Figure 30, the output file for each cylinder-pressure data point lists gross IMEP and gross indicated work. These values represent parameters that are measured inside the engine cylinder and,

therefore, cannot be directly compared to other measured values. However, it is possible to check their magnitude with measured power, brake work, and Brake Mean Effective Pressure (BMEP) to ensure fundamentally reasonable values. Gross indicated performance parameters only depict the work or pressure applied on the engine piston during compression, combustion and expansion; whereas, brake parameters depict the performance at the driveshaft or useful work from the engine. As a result, indicated performance parameters are higher because they do not take mechanical and pumping losses into account [1]. The addition of net IMEP in the future will provide the opportunity to calculated net performance parameters that will be important after adding a turbocharger. The brake parameters were previously available in the Yanmar test cell and used extensively for the biodiesel study in Chapter 2. Specifically, by using data for engine speed and torque, engine brake power, work per cycle, and BMEP can be determined respectively:

Engine Brake Power	$P = 2\pi \cdot N \cdot T$	(10)
Work per Cycle	$W_b / cycle = \frac{P \cdot n_R}{N}$	(11)
BMEP	$bmep = \frac{P \cdot n_R}{V_d \cdot N}$	(12)

where P is engine brake power, N is engine speed, T is engine brake torque, $W_b/cycle$ is engine brake work per engine cycle, n_R is number of engine cycles to thermodynamic cycles, and $bmep$ is brake mean effective pressure. Using measured values for speed and torque, the brake performance parameters are compared to the gross indicated work and gross IMEP in Table 11.

Table 11. Measured Brake and Indicated Performance Parameters with Standard Deviation in Measurements Provided

Generator Load %	Speed	Torque	Power	Brake Work	Gross Indicated Work	BMEP	$IMEP_g$
	RPM	N-m	kW	kJ/cycle	kJ/cycle	bar	Bar
ULSD							
0	3600±2	0.63±0.10	0.24±3E-05	0.008±0.001	0.079	0.18±0.03	1.83
25	3565±2	4.48±0.39	1.67±9E-05	0.056±0.005	0.119	1.29±0.11	2.73
50	3545±2	8.60±0.22	3.19±4E-05	0.108±0.003	0.163	2.48±0.06	3.75
75	3528±2	12.27±0.27	4.53±6E-05	0.154±0.003	0.204	3.54±0.08	4.68
100	3509±2	15.70±0.30	5.77±7E-05	0.197±0.004	0.244	4.53±0.09	5.60
UCO Biodiesel							
0	3588±2	0.73±0.09	0.28±2E-05	0.009±0.001	0.079	0.21±0.03	1.80
25	3560±2	4.48±0.47	1.67±1E-04	0.056±0.006	0.117	1.29±0.14	2.68
50	3541±2	8.62±0.20	3.20±4E-05	0.108±0.003	0.163	2.49±0.06	3.73
75	3529±3	12.35±0.26	4.57±7E-05	0.155±0.003	0.204	3.56±0.07	4.69
100	3507±2	15.71±0.30	5.77±6E-05	0.197±0.004	0.245	4.53±0.09	5.61
JP-8							
0	3583±2	0.65±0.10	0.24±2E-05	0.008±0.001	0.076	0.19±0.03	1.74
25	3552±2	4.40±0.38	1.64±9E-05	0.055±0.005	0.118	1.27±0.11	2.71
50	3548±2	8.64±0.21	3.21±4E-05	0.109±0.003	0.163	2.49±0.06	3.73
75	3534±2	12.32±0.27	4.56±6E-05	0.155±0.003	0.206	3.55±0.08	4.74
100	3494±4	15.56±0.29	5.69±1E-04	0.195±0.004	0.244	4.49±0.08	5.59

It is worth noting that the relative differences between the indicated and brake parameters stay approximately constant across all fuels and loads and represents the mechanical efficiency of the engine [1]. This is to be expected for an engine running at a nearly constant speed across various loads because pumping and frictional losses should be similar; e.g. Heywood explains that mechanical efficiency is largely variable with engine speed [1]. Furthermore, normal mechanical efficiencies under full load are in the range from 75% to just under 90% [45]. Based on the data in Table 6 for 100% generator load (80% engine load), the mechanical efficiency at is approximately 80% as calculated [1]:

Mechanical Efficiency	$\eta_m = \frac{P}{P_{i,g}} = \frac{W_b}{W_{i,g}}$	(13)

where η_m is mechanical efficiency, and $P_{i,g}$ is indicated gross power. Though pumping losses are both negative and negligible for a naturally-aspirated compression ignition engine, eventual turbocharging

will require the net indicated work and imep to be calculated. When the engine is turbocharged, the brake output work will be greater as the turbocharger creates additional output during the pumping loop (increased intake and exhaust pressures), meaning that mechanical efficiency will increase and need to be calculated using net indicated work instead of gross indicated work, once the turbocharger is installed.

By considering the mechanical efficiency calculated using measured data with expected values from literature, it becomes apparent that the indicated parameters determined by the LabVIEW program are appropriate. This finding demonstrates proper coding across different fuels via the correct relative magnitude as compared to recorded brake values.

3.3.2.1 Determining Start of Injection, Start of Combustion, and Ignition Delay

As shown in Figure 30, the output file provides engine crank angle, instantaneous pressure, and instantaneous volume. By comparing the instantaneous pressure for combustion (aka firing curve) with the motoring curve at corresponding crank angles, one can roughly estimate the start of injection, start of combustion, and corresponding ignition delay. During the compression stroke, the pressure of both the firing and motoring profiles will nearly coincide since the engine is only compressing air and, if the engine is firing, a small amount of residual exhaust (est. 1-2% of mass) that did not escape the engine during the previous exhaust stroke. However, the pressure in the cylinder will decrease slightly when liquid fuel is injected, causing the firing curve to diverge from the motoring curve pressure profile as energy is transferred from the compressed gas to vaporize the fuel; via the ideal gas law, when temperature decreases, so will the pressure. Additionally, the net heat release at this point becomes negative [1]. The point at which this occurs marks an estimated start of injection. Furthermore, the point at which pressure begins to rapidly increase beyond the motoring curve, and net heat release becomes positive, for the combustion data is considered the point when combustion occurs. With these

angles known, the ignition delay is then defined as the duration between the beginning of injection and start of combustion.

Some discrepancies do exist between the motoring and firing curve data as the current motoring curve data reflects a relatively cool cylinder wall. When the system to dynamically control fuel injection timing is operational, it will be possible to stop injection while motoring the engine using the dynamometer. By firing the engine first, the cylinder walls will be hotter to more accurately mimic the firing curve when motoring data is taken. The start of injection and combustion can be seen in the pressure profiles of Figure 40.

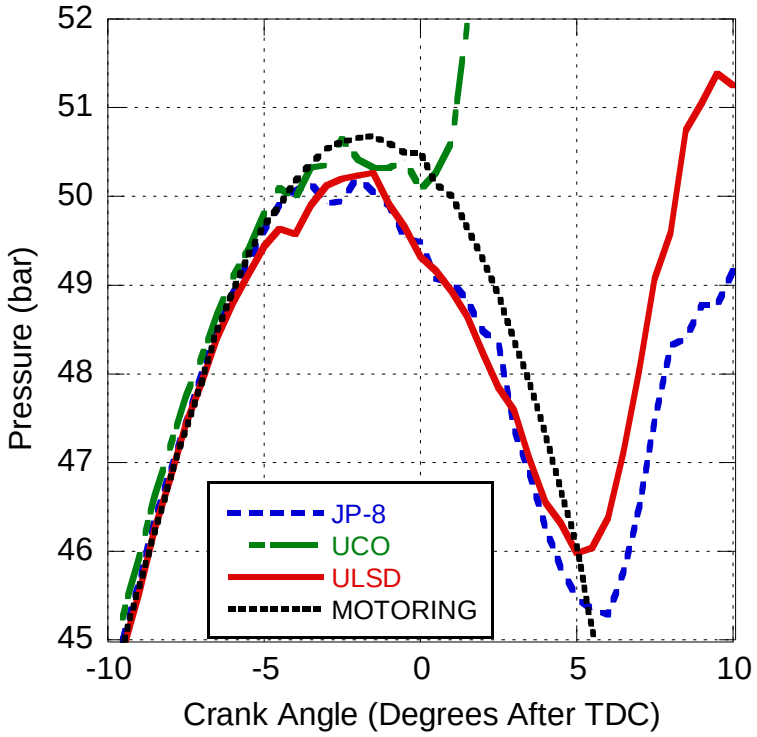

Figure 40. Pressure vs. Engine Crank Angle for Motoring Curve, JP-8, UCO Biodiesel, and ULSD

A more widely accepted method of determining the start of combustion is to perform a heat release analysis to yield data similar to that for Figure 9 [1, 48]. In this plot, the crank angle 'b' represents when combustion begins and the heat release rate becomes positive inside the engine as the fuel is oxidized. By using the heat release code developed by Depcik et al. [48], it is possible to find the engine crank angle when this occurs; i.e. combustion begins and is releasing energy. The program is

operated by inputting engine geometry and operational parameters of speed, fuel flow, air flow, EGR percentage (0% as passage blocked), and an estimated cylinder wall temperature. The default settings for heat transfer and the equilibrium properties package for diesel fuel were used to complete the calculations while adjusting the cylinder wall temperature to normalize the fuel mass fraction burned with the combustion efficiency calculated later in this discussion. The program output yields the rate of heat release versus crank angle values, from which the corresponding calculated crank angles for start of combustion are found when the heat release rate becomes positive [1]. It is theoretically possible to detect start of injection in a similar method by finding the crank angle where heat release becomes negative [1]. The point when the heat release rate became negative (indicating injection) was not apparent from the program output due to signal noise. Table 12 includes the remainder of the performance data needed for the heat release analysis (rest shown in Table 11) and the crank angles found for start of combustion. Also included in Table 12 are the crank angles for start of injection, start of combustion, and ignition delay determined by comparing the combustion and motoring pressure data. Figure 41 depicts a sample output from the heat release code [48] based on recorded data for UCO biodiesel shows many similarities to the example heat release profile discussed by Heywood in Figure 9 with respect to ignition delay, combustion peaks, and overall heat release behavior.

Table 12. Calculated and Measured Start of Injection, Start of Combustion, and Ignition Delay

Fuel/ Gen. Load	Speed	Air Flow Rate	Measured Start of Injection	Calculated Start of Combustion	Measured Start of Combustion	Measured Ignition Delay
%	RPM	g/s	degrees after TDC	degrees after TDC	degrees after TDC	degrees
ULSD						
0	3600	11.42	-9.5	4.0	5.5	15.0
25	3565	11.37	-4.0	3.5	4.5	8.5
50	3545	11.29	-3.5	3.5	3.5	7.0
75	3528	11.16	-1.5	3.5	3.5	5.0
100	3509	10.98	-1.0	4.0	3.0	4.0
UCO Biodiesel						
0	3588	11.35	-9.5	0.5	0.5	10.0
25	3560	11.32	-4.5	-0.5	-0.5	4.0
50	3541	11.26	-4.0	0.0	0.5	4.5
75	3529	11.16	-2.5	0.5	0.5	3.0
100	3507	10.96	-1.5	1.0	1.5	3.0
JP-8						
0	3583	11.40	-9.5	5.0	5.5	15.0
25	3552	11.37	-3.5	4.0	5.5	9.0
50	3548	11.32	-3.0	5.0	5.5	8.5
75	3534	11.18	-1.0	5.5	5.5	6.5
100	3494	10.93	-1.0	6.0	6.0	7.0

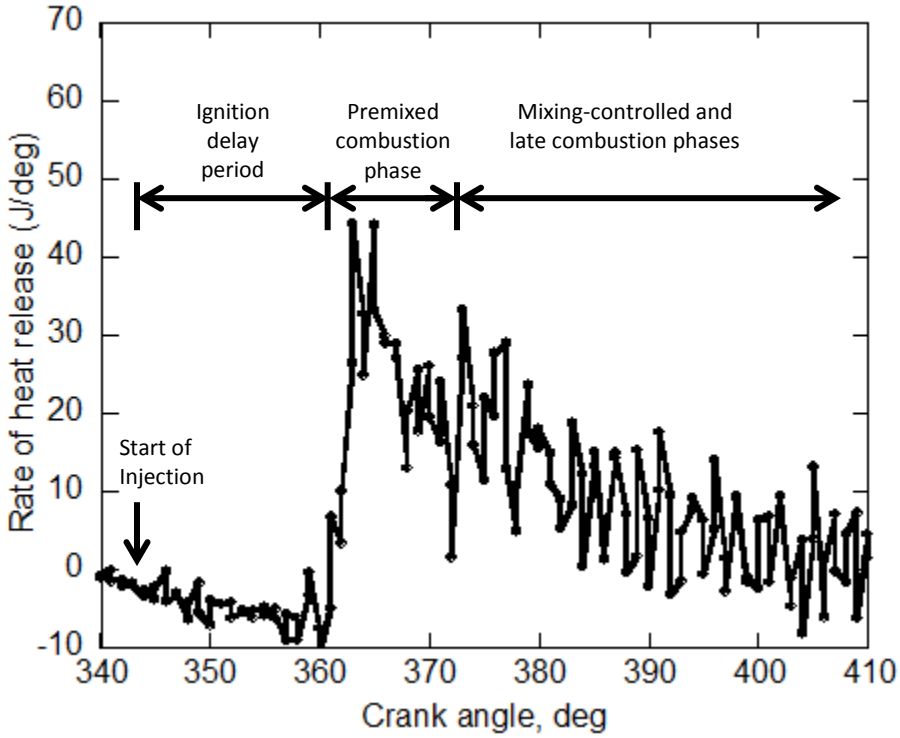

Figure 41. Heat Release Rate for UCO Biodiesel From Heat Release Code[48].

The crank angles found to correspond to the start of injection are later than the 15.5^{o} before TDC (-15.5^{o}) as stated by the Yanmar manual. This could be because enough fuel has to be injected, atomized and vaporized before showing up on the in-cylinder pressure trace (un-atomized and un-vaporized fuel does not affect gas pressure). However, the measured start of injection occurs at about the same crank angle regardless of the fuel being tested. This is in disagreement with results in literature and it is suspected that estimating injection may not be as rigorous as necessary to precisely determine the start of injection. In addition, this injection is found to occur earlier at low loads, and progressively occur later as the engine load increases across all fuels. This is likely not indicating a change in injection timing, but rather an effect of higher cylinder wall temperatures at high loads leading to increased heat transfer to the gas before injection occurs and partially obscuring the effects of injection on pressure [1]. The higher pressure of the gas at high loads leads to larger pressure differences between the motoring and combustion curves, and makes determination of injection timing more difficult. This is further compounded by the fact that the cylinder walls of the engine during the collection of motoring data were not as hot and, therefore, will not transfer as much heat to the gas during compression, leading to slightly lower pressures as not as much heat transfer is occurring. As a result, the pressure of the motoring curve used may be slightly lower than it needs to be to accurately determine injection. In the future, using the new dynamometer to record motoring data will improve the accuracy of this data as a constant motoring speed will be utilized, rather than the gradual slowing of the engine during the recording of the motoring curve used here. Moreover, the upgrade of the fuel injection process to a rail pressure system where the user specifies the injection timing will provide the needed knowledge of actual injection timing.

Comparison of the start of combustion values determined by observing measured pressures with those calculated from the heat release analysis demonstrates general agreement with both methods; however, the use of heat release rate is stated to be the more accurate method for

determining the start of combustion. Differences between the two methods may be the result of the fact that heat release is a rate that needs a positive change in pressure to indicate the release of energy, whereas pressure is a direct measurement.

Observation of the ignition delay for each fuel shows that as load increases, the ignition delay decreases. This is caused by higher cylinder wall temperatures and hotter residual gases that did not escape the engine during the previous exhaust cycle [1]. As a result, the gas in the cylinder is hotter upon injection and more effectively vaporizes and ignites the fuel. Despite apparently being injected at nearly the same crank angle, UCO biodiesel has the shortest ignition delay across all loads, followed by ULSD, then JP-8, which has longer ignition delays than ULSD at loads other than 0%. Reviewing the fuel properties in Table 10 illustrates that the Cetane Number for UCO biodiesel was the highest at 52.8, followed by JP-8 at 42.5, and ULSD at 42.3. As stated in Chapter 2, CN is a dimensionless parameter that characterizes ignition delay relative to cetane. Since these values are often directly related to ignition delay in an engine, the results in Table 12 are feasible as a direct relationship between fuel ignition delay and CN exists as biodiesel's ignition delay was considerably shorter, whereas UCO biodiesel and JP-8 delays were similar.

3.3.2.2 In-Cylinder Pressure Plots

To assist in the discussion of fuel economy and engine emissions, the in-cylinder pressure versus crank angle plots for the fuels at each load are depicted in Figures 42 through 47. In Figure 42, the pressure profile is shown for each of the three fuels from -180^{o} to +180^{o} at zero load. Observation of the pressure profile in Figure 42 indicates that there is oscillation from about 150^{o} before TDC to 120^{o} before TDC. This is caused by the closing of the intake valve, which ends at 122^{o} before TDC, but is not instantaneous. For a combustion analysis, it is helpful to investigate the pressures and time-shifting that occurs closer to TDC from just before the injection event (approximately 15^{o} before TDC) to where combustion pressures become approximately equal to the exhaust manifold pressure (180^{o} after TDC).

The same pressure profile from Figure 42 is shown in Figure 43 for only the crank angles around TDC. As a result, more information can be gleamed from this figure due to the finer detail presented. The pressure profiles for each fuel at 25%, 50%, 75%, and 100% of generator load are shown in a similar fashion, from Figure 44 to Figure 47.

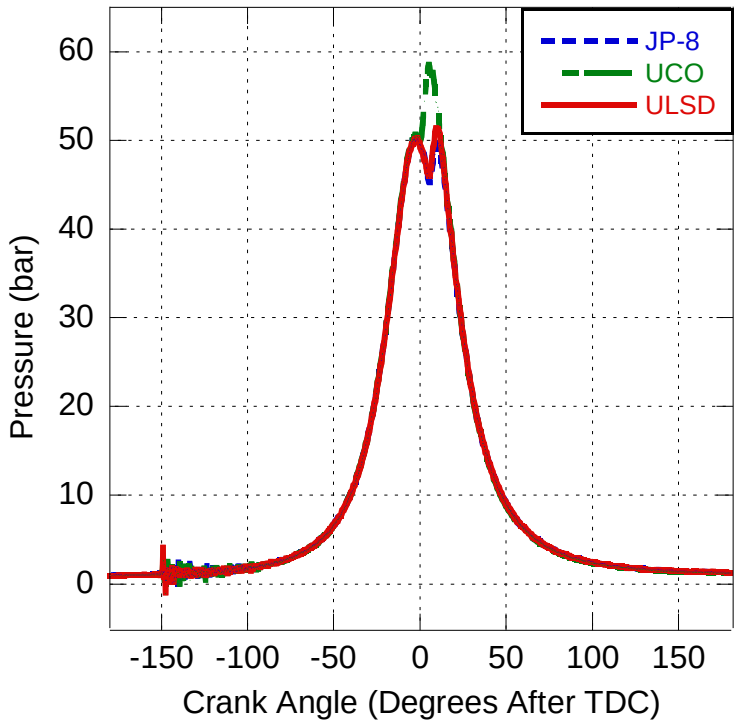

Figure 42. Pressure (bar) vs. Crank Angle (deg) for 0%-Load over One Revolution

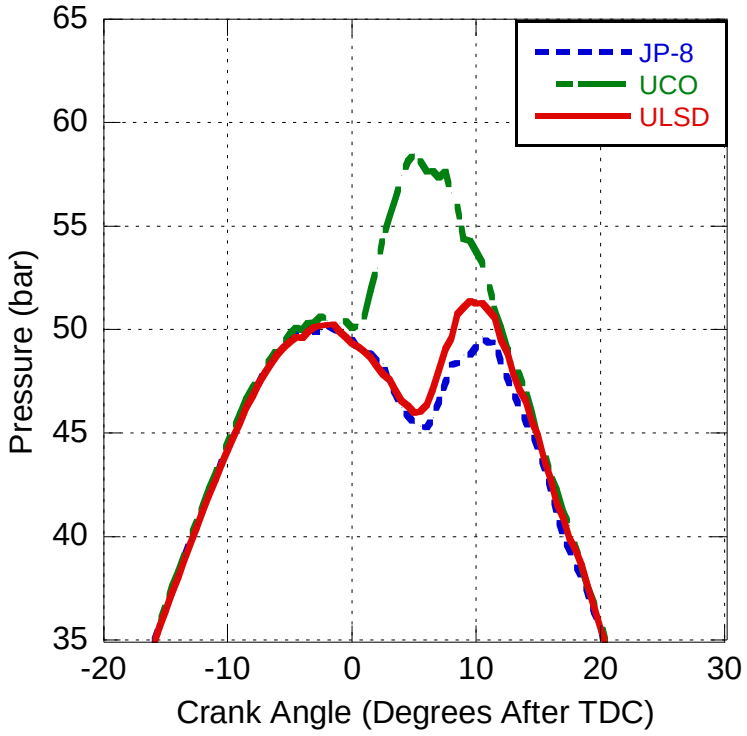

Figure 43. Pressure (bar) vs. Crank Angle (deg) for 0%-load

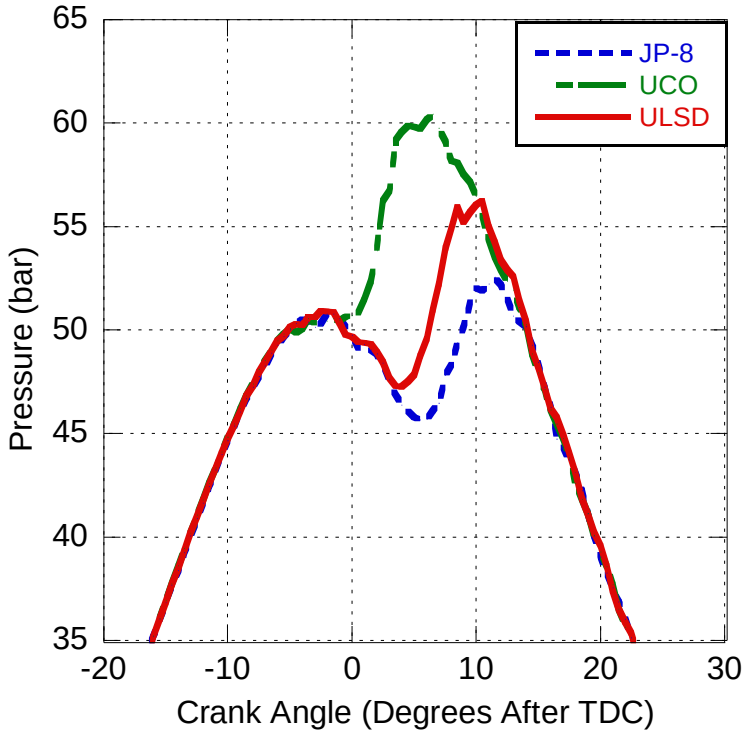

Figure 44. Pressure (bar) vs. Crank Angle (deg) for 25%-load

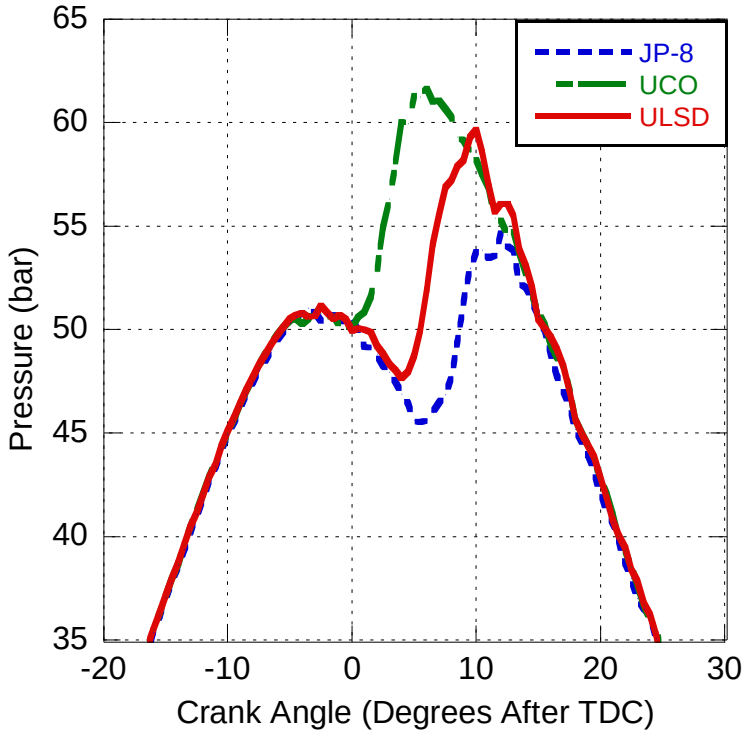

Figure 45. Pressure (bar) vs. Crank Angle (deg) for 50%-load

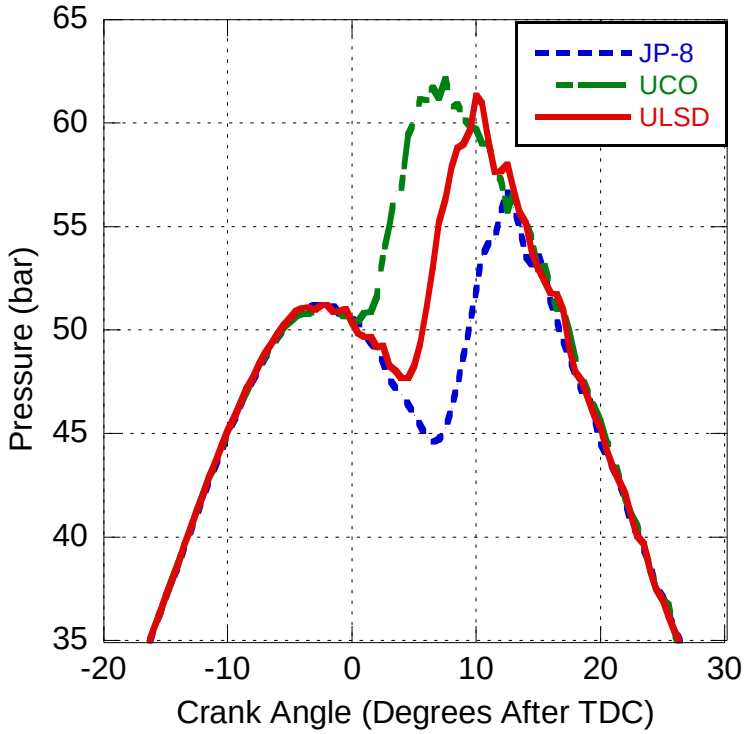

Figure 46. Pressure (bar) vs. Crank Angle (deg) for 75%-load

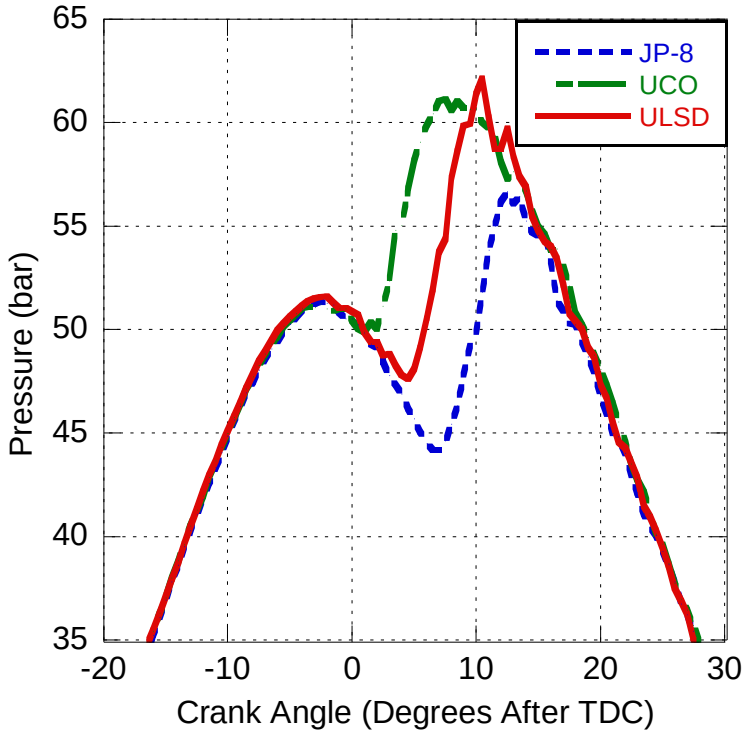

Figure 47. Pressure (bar) vs. Crank Angle (deg) for 100%-load

From Table 10, it is shown that JP-8 has a Cetane Number between ULSD and UCO biodiesel [9, 47] indicating that if all other fuel properties were held constant, ignition of JP-8 would happen after UCO biodiesel, but before ULSD; however, its ignition is significantly delayed in comparison to both fuels through the pressure traces observed in the Yanmar engine. For example, it can be seen in Figures 43 through 47 that combustion of JP-8 occurs later than both ULSD and UCO as supported through the heat release analysis. This is likely due to the lower density and viscosity of JP-8 as indicated in Table 10. In a manner similar, but reversed to the biodiesel fuels studied in Chapter 2, a lower viscosity fuel (biodiesel has a higher viscosity) is able to leak through clearance volumes in the mechanical fuel pump. This leakage results in a slower pressure rise in the pump and results in a later injection [9, 47]. Furthermore, a less dense fuel typically has a lower bulk modulus resulting in a slower pressure wave speed in the injection line [3]. As a result, injection will occur later still as the effects of pump leakage and slower pressure waves combine. As stated above, the results found from a pressure curve comparison and

heat release analysis were in disagreement with literature, indicating a more advanced method may be necessary for determining injection timing such as an increased number of pressure profiles used in averaging, or by using a proximity sensor to measure fuel injector needle lift as done by Szybist et al.[31]. However, the lower viscosity of a fuel such as JP-8, will also promote finer atomization of the fuel spray upon entering the cylinder. This spray behavior, in addition to the increased volatility of JP-8, can result in faster combustion once injection does occur [1, 49, 50].

Hence, the in-cylinder pressure study reinforces the discussions of the previous fuel study regarding Cetane Number, density, and viscosity, while partially explaining why combustion of UCO biodiesel (density = 0.878 kg/m^3) occurs slightly earlier than ULSD (density = 0.831 kg/m^3) and significantly earlier than JP-8 (density = 0.801 kg/m^3). However, inspection of the resulting pressure plots indicates that the density (and bulk modulus) plays a more significant role in combustion phasing than does viscosity and volatility because combustion of the lower-density JP-8 occurs later than ULSD despite its reduced viscosity and higher volatility.

3.3.2.3 Brake-Specific Fuel Consumption

Due to the rising costs of fuel, fuel consumption plays a critical role in the evaluation of the performance of a fuel. This is especially true of the military as fuel may cost up to $400/gallon; a price several orders of magnitude larger than domestic prices due to the cost of procurement and transport to remote locations [51]. In order to include this performance metric, the system validation tests included measurement of Brake Specific Fuel Consumption (BSFC) with the results found in Table 13.

Table 13. BSFC for ULSD, UCO Biodiesel, and JP-8

BSFC (g/kW-hr)	Generator Loading Percentage				
Fuel	0%	25%	50%	75%	100%
ULSD	3198±266	548±24	366±4.9	313±3.6	293±2.9
UCO Biodiesel	2880±186	618±33	416±5.0	355±3.8	335±3.5
JP-8	2819±212	550±24	365±4.7	315±3.5	294±2.8

It is claimed in Chapter 2, and supported here, that density influences fuel consumption since the mechanical fuel pump injects a constant-volume of fuel each thermodynamic cycle. Hence, a lower density fuel may result in less fuel mass injected. This is found to be a reasonable conclusion as ULSD has a lower density than UCO Biodiesel (831 and 878 kg/m^3, respectively) and a lower BSFC at all loads other than 0%. When comparing JP-8 to ULSD, this relationship is not as evident, although JP-8 is less dense (801 kg/m^3) than ULSD, it has very similar fuel consumption all loads other than 0%. This indicates that while density plays a role in fuel consumption, and less mass is injected when burning JP-8, other factors such as the delayed injection of JP-8 may have a greater influence.

A fuel with high energy content, such as ULSD and JP-8 (Table 10) will likely have lower fuel consumption than a fuel with relatively low energy content (UCO biodiesel). This is indeed the case as shown through the BSFC results found in Table 13. When considering the higher energy content, low viscosity (for improved atomization), and high volatility of JP-8, it appears that the only reason that JP-8 did not have a lower BSFC than ULSD is due to its late combustion. This finding supports the argument that advancing the injection of JP-8 will result in lower fuel consumption that ULSD [47, 52].

Finally, it is important to compare combustion, thermal, and fuel conversion efficiencies when each fuel is used. These efficiencies help explain why using UCO biodiesel results in fuel consumption (Table 13) that is relatively close to that of ULSD and JP-8, despite its much lower fuel energy content as seen in Table 10. The combustion efficiency is the fraction of the fuel energy that is released in the combustion process as denoted by Equation 14 [15]. It is composed of both the heating value of the fuel and the energy remaining in the exhaust constituents, such as CO and HC. As was done similarly to the work of Cecrle et al., the lower heating value of the hydrocarbons was assumed to be 44,700 kJ/kg [15]:

Combustion Efficiency	$\eta_c = 1 - \frac{\sum_{j=1}^{n} \dot{m}_j \cdot Q_{lhv,j}}{\dot{m}_f \cdot Q_{lhv,f}}$	(14)

where η_c is combustion efficiency, $\dot{m}_j$ is exhaust constituent mass flow rate, $\dot{m}_f$ is fuel mass flow rate, and $Q_{lhv,j}$ is fuel lower heating value. A common exhaust constituent is diatomic hydrogen, which was not measured in these tests, but is important to consider due to its potent lower heating value (120 MJ/kg). It can be estimated by assuming a similar molar ratio of H_2:CO as that of H_2O:CO_2 based on the general lean combustion reaction and the typical product species of H_2O and CO_2 [15]. Similar to the work of Cecrle et al., the H_2O emissions were not measured either, but can be assumed based on a generalized lean combustion reaction normalized to one mole of fuel [15]:

General Lean Combustion Reaction	$\mathrm{C}_x\mathrm{H}_y\mathrm{O}_z + a\left(\mathrm{O}_2 + 3.76\mathrm{N}_2\right) \rightarrow b\mathrm{CO}_2 + c\mathrm{H}_2\mathrm{O} + d\mathrm{O}_2 + e\mathrm{N}_2$	(15)

where the carbon constituents of ULSD and UCO biodiesel are from measurements of an independent lab for the biodiesel study in Chapter 2 and the carbon constituent of JP-8 is based on literature [53]. With the necessary x ,y, and z coefficients, the H_2O:CO_2 and H_2:CO molar ratios are estimated. By converting the molar H_2:CO ratio to a mass ratio, the mass flow rate of H_2 is estimated using measured CO flow rates. For a diesel engine, which operates in lean regimes, the combustion efficiency is normally about 98% [1], so these assumptions are applicable.

In addition, fuel conversion efficiency (η_f) is a measure of the efficiency of useful work coming from added fuel energy [15]:

Fuel Conversion Efficiency	$\eta_f = \dfrac{P}{\dot{m}_f \cdot Q_{lhv,f}}$	(16)

Higher fuel conversion efficiency means that more useful power is being created from supplied fuel energy. Finally, the thermal conversion efficiency (η_t) is an indicator of how effectively fuel is creating actual work and is a combination of the combustion and fuel conversion efficiencies, related by [15]:

Thermal Conversion Efficiency	$\eta_t = \dfrac{\eta_f}{\eta_c}$	(17)

Using these three efficiency equations and the necessary measured parameters of fuel flow rates, fuel properties, and brake performance, the efficiencies are plotted in Figures 48 through 50 for different engine loads applied to the Yanmar engine.

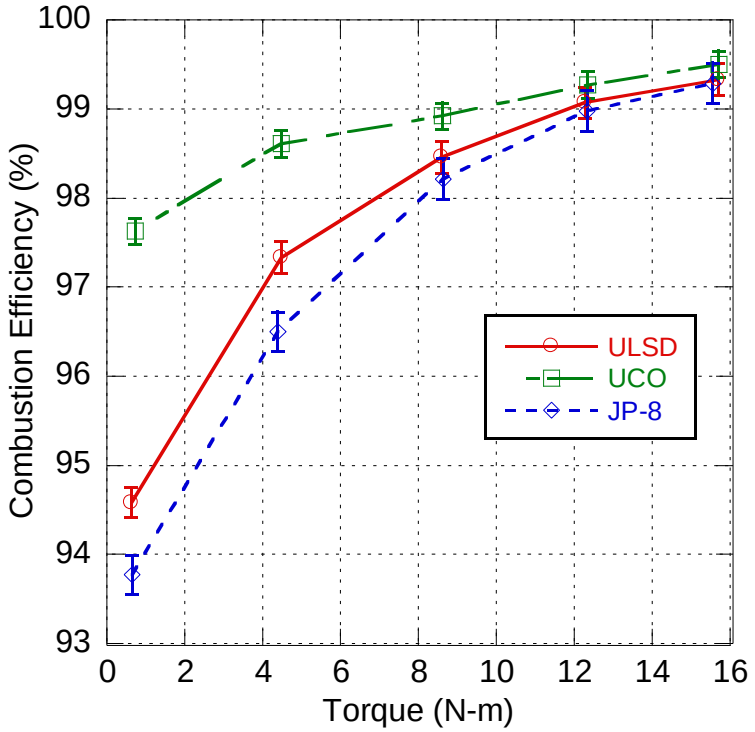

Figure 48. Combustion Efficiency vs. Torque for ULSD, UCO Biodiesel, and JP-8

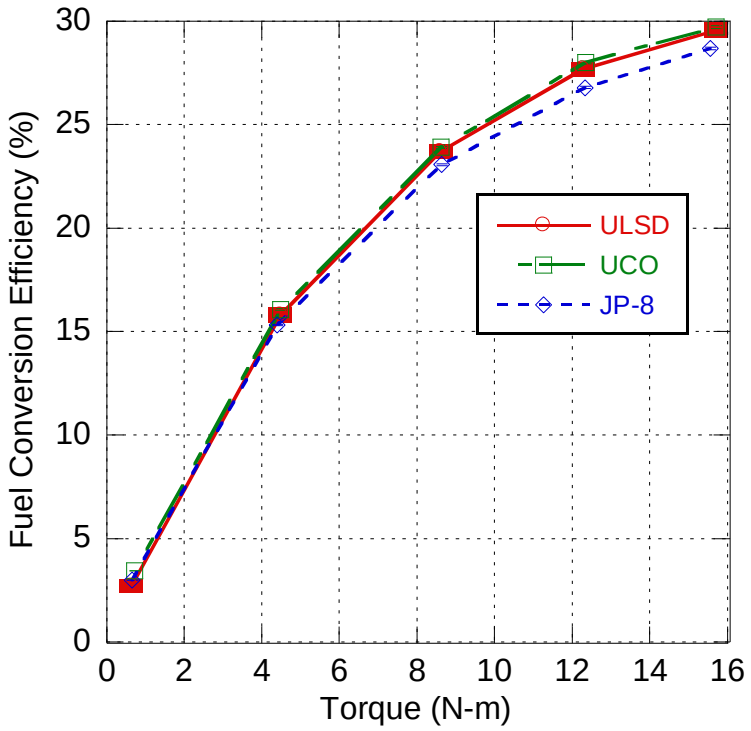

Figure 49. Fuel Conversion Efficiency vs. Torque for ULSD, UCO Biodiesel, and JP-8

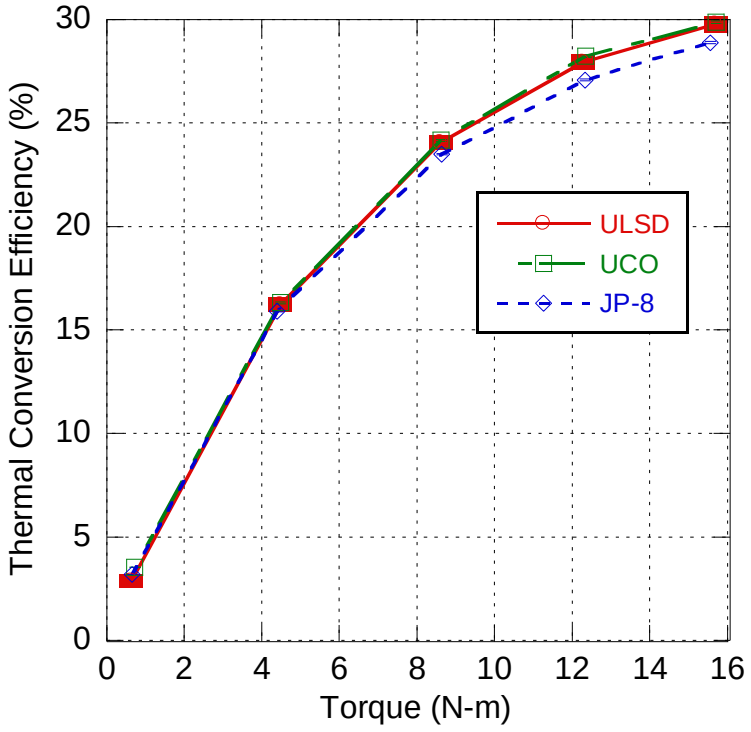

Figure 50. Thermal Conversion Efficiency vs. Torque for ULSD, UCO Biodiesel, and JP-8

Combustion that occurs earlier takes advantage of higher in-cylinder pressures resulting in more work being done on the piston. This statement is supported by the findings displayed in Figure 47 as biodiesel, with higher in-cylinder pressures than both ULSD and JP-8, has noticeably higher combustion efficiency than the other two fuels, due in large part to the hotter temperatures, longer duration, and oxygen quantity present in the fuel. This effectively helps to offset the lower energy content of biodiesel and improve its fuel economy. Furthermore, since JP-8 combustion begins later in the cycle than either ULSD or UCO biodiesel, its combustion efficiency is lower because cylinder temperatures are not as hot, and the combustion event does not last as long. Similar trends for these fuels are apparent in both the fuel conversion and thermal conversion efficiencies shown in Figures 48 and 49, respectively. Specifically, UCO biodiesel has the highest conversion efficiencies, followed by ULSD and JP-8. This means that more useful work is being produced from a given quantity of biodiesel than for the other fuels. The higher energy content and lower density and viscosity of JP-8 explains why the conversion efficiency of JP-8 is only slightly lower than that of ULSD, as these factors have been shown to improve combustion. As a result, it stands to reason that it may be possible to achieve a lower BSFC of JP-8 than that of ULSD through advancing injection timing, promoting better fuel economy for the military, as stated previously [47, 52].

3.3.2.4 Emissions

In addition to considering fuel consumption, measuring the emissions of an engine running on each fuel is important due to negative environmental and health effects. Therefore, the resulting brake-specific emissions measured by the Semtech emissions analyzer (similar to the efforts of Chapter 2) are provided in Table 14 for comparison.

Table 14. Emissions for ULSD, UCO Biodiesel, and JP-8

Fuel	Generator Loading Percentage				
	0%	25%	50%	75%	100%
CO_2 (g/kW-hr)					
ULSD	9909±210	1735±112	1165±34.6	1000±30.0	937±25.5
UCO Biodiesel	9149±167	1971±137	1325±31.4	1132±27.8	1068±27.4
JP-8	8710±189	1728±111	1159±33.2	1003±28.9	938±25.2
CO (g/kW-hr)					
ULSD	192±4.2	17.2±1.29	6.85±0.43	3.87±0.38	3.13±0.34
UCO Biodiesel	83.6±1.8	10.5±0.83	5.56±0.35	3.77±0.30	2.97±0.27
JP-8	171±3.8	20.0±1.45	8.18±0.45	4.66±0.32	3.66±0.30
NO (g/kW-hr)					
ULSD	24.6±0.55	8.33±0.55	7.13±0.24	6.84±0.29	6.60±0.26
UCO Biodiesel	39.1±0.74	10.76±0.76	7.86±0.23	7.28±0.22	6.80±0.20
JP-8	14.6±0.47	6.06±0.40	5.82±0.20	5.91±0.20	5.70±0.19
NO_2 (g/kW-hr)					
ULSD	26.26±0.57	3.27±0.22	1.29±0.05	0.57±0.03	0.20±0.02
UCO Biodiesel	17.92±0.34	2.17±0.15	0.86±0.03	0.38±0.01	0.13±0.01
JP-8	22.58±0.50	3.32±0.22	1.21±0.05	0.42±0.02	0.15±0.01
NO_x (g/kW-hr)					
ULSD	50.84±1.09	11.60±0.76	8.42±0.28	7.41±0.31	6.80±0.27
UCO Biodiesel	57.02±1.06	12.93±0.91	8.72±0.25	7.66±0.23	6.93±0.20
JP-8	37.19±0.85	9.38±0.61	7.04±0.24	6.33±0.21	5.84±0.19
HC (g/kW-hr)					
ULSD	60.6±1.4	4.52±0.50	1.87±0.19	1.00±0.05	0.72±0.03
UCO Biodiesel	15.4±0.4	2.19±0.16	1.38±0.07	0.80±0.04	0.48±0.03
JP-8	60.3±1.4	6.86±0.49	2.32±0.24	1.18±0.06	0.73±0.03

For compression ignition engines, the NO_x emissions are of particular concern as aftertreatment conversion of these species is difficult and, as discussed previously, are more actively created at high temperatures due to the chemical kinetics of the Thermal NO_x mechanism [1]. During combustion, high pressures and temperatures lead to NO and NO_2 formation. Traditionally, this is understood to be an especially big obstacle for biodiesel use [2, 3, 9, 12, 17, 36, 43]. Inspecting the in-cylinder pressure profiles in Figures 42 through 47 indicates the cause as there is a direct correlation between combustion phasing and NO_x emissions. The pressure profile figures illustrate that combustion of UCO biodiesel is advanced in comparison to the other fuels and reaches the highest pressures (and temperatures via the ideal gas law) for the longest durations. This is followed by ULSD and then JP-8, with later injection and combustion causing lower cylinder pressures and temperatures. The earlier combustion of biodiesel

leads to higher in-cylinder temperatures that lead to increased thermal NO formation and the highest measured NO emissions across all engine loads. Furthermore, since these higher temperatures are experienced earlier in the engine cycle, this results in a longer time of a relatively hot combustion chamber yielding even more opportunity for NO to form.

By contrast, UCO biodiesel was found to have the lowest NO_2 emissions that is formed in the flame zone through oxidation of NO. Normally, NO_2 is converted relatively quickly back to NO in a hot combustion process; however, it may be quenched by mixing with cooler gases first, thereby stopping the NO_2 to NO conversion process and leading to NO_2 in the exhaust [1]. For this reason, diesel engines at low loads will tend to have increased NO_2 emissions since there are ample cool regions of the cylinder where NO_2 can be quenched (validated via Table 14). As a result, biodiesel has the lowest NO_2 emissions because of earlier combustion, where higher cylinder temperatures allow fewer cool regions to quench the NO_2 to NO conversion process. By contrast, ULSD and JP-8 have higher NO_2 emissions because of reduced temperatures due to a later phased combustion.

In addition to the influence of combustion timing, the properties of the fuels tested will have some impact on emissions as discussed in Chapter 2. Since UCO biodiesel is an oxygenated fuel, fuel-rich regions near the nozzle may combust earlier because the fuel also contains oxygen, effectively making the mixture less rich. Increased regions near stoichiometry can lead to increased NO formation [1]. The influence of density and bulk modulus on NO_2 emissions are likely overshadowed by energy content of the fuel. Simply stated, a more energy-dense fuel will require less fuel to be injected into the cylinder per cycle. This will result in more fuel-lean regions in the engine, allowing many opportunities to create NO_2. Due to the strong correlation between NO_x emissions and combustion timing, it is challenging to say with exact certainty which fuel properties directly affect emissions.

In addition to NO_x emissions, products of partial combustion, such as CO, HCs, and PM must be analyzed as well due to their negative environmental and health effects. These emissions typically occur

in rich regions of the cylinder; i.e., near the injector nozzles during the injection process. In the spray of the injector, equivalence ratios go from lean near the edges to extremely rich very near the injector holes. As a result, species of partial combustion products can form. Under loaded conditions, high pressures and temperatures help oxidize these species into complete products of combustion; e.g., CO_2 and H_2O. As a result, partial combustion product (CO, HCs, and PM) emissions actually decrease with increased load despite the increased fuel (carbon) available in the engine to create these products. The effect of combustion timing also plays a critical role in the emission of these products. For example, the combustion of UCO biodiesel is known (and found) to occur earlier than ULSD and JP-8. While this early combustion leads to higher pressures and temperatures, the cylinder is also exposed to high temperatures for longer durations (see Figures 42 through 47) before the exhaust valve opens. This allows partial combustion products more time to oxidize and for this reason, emissions of CO, HC, and PM are lower for biodiesel than for ULSD [9]. These trends can clearly be seen the emission results in Table 14 ending in a higher combustion efficiency (Figure 48). In addition, since JP-8 combustion occurs later in the cycle with lower cylinder pressures and temperatures than the other fuels, it has higher CO and HC emissions (less time for combustion and lower temperatures reducing thermal oxidation). Finally, it should be noted that the CO_2 emissions for UCO were higher than those for ULSD and JP-8. This is due to the increased fuel consumption of biodiesel and, though less significantly, improved combustion where partial combustion products are fully oxidized.

As discussed for NO_x, fuel properties will play a role in the emissions of CO, HC, PM, and, indirectly, CO_2. As discussed previously, the density (and therefore bulk modulus [3]) will have an impact on injection timing and combustion timing. In addition, viscosity affects the injector's ability to atomize the fuel. As a result, a more viscous fuel such as the UCO biodiesel will have poor vaporization as compared to JP-8, which is less viscous. Due to this relationship, it is expected that UCO biodiesel would have higher BSFC and CO, CO_2, HC, and PM emissions than ULSD and JP-8. Since this is not the

case (Table 14), it is apparent that other factors have a more direct effect on these emissions; e.g., when combustion begins (Figures 42 through 47) and the impact of an oxygenated fuel.

Furthermore, at 0% load, where there are ample cool regions, CO emissions are increased for ULSD as compared to JP-8, likely due to poor fuel atomization and increased fuel consumption of ULSD as compared to JP-8. At other loads, CO, HC, and likely PM, emissions are higher for JP-8 than for ULSD, pointing to other factors impacting these emissions. Due to cross-sensitivity with other factors such as injection time, it is difficult to make direct comparisons between JP-8 and ULSD in this specific case. Future upgrades, mentioned in the Introduction of this thesis, include installation of dynamic control of fuel injection. This system will provide the needed flexibility that will allow for direct comparison of fuels when combustion occurs at the same engine crank angle. This ability will yield a more thorough understanding of individual fuel characteristics and their impact on engine performance and emissions.

Table 15. Estimated influence on fuel consumption and emissions based on literature [1-5] and experimental discussion

Increasing Property	NO	NO_2	NO_x	CO	CO_2	HC	PM	BSFC
Density (increases bulk modulus)	↑	↑	↑	↓	↓	↓	↓	↓
Viscosity (decreases atomization)	↓	↓	↓	↑	↑	↑	↑	↑
Cetane Number	↓	↓	↓	↓	↓	↓	↓	↓
Start of Injection(advanced via bulk modulus)	↑	↑	↑	↓	↓	↓	↓	↓
Energy Content	↑	↑	↑	↓	↓	↓	↓	↓
Oxygen Content	↓	↓	↓	↓	↑	↓	↓	↑

3.4 Conclusion

With the rapid growth of biodiesel production, it is prudent to research ways to improve its operation and performance in an engine, especially concerning fuel economy and exhaust emissions. Chapter 2 of this work discussed the search for important biodiesel fuel properties using a collection of feedstocks specifically chosen to provide a chemically diverse set of fuels. These fuels were tested in a single-cylinder engine test cell built by graduate students at KU. It was found that biodiesel's molecular

unsaturation, density, hydrogen to carbon molar ratio, energy content, oxygen content, and viscosity all play measureable roles in engine fuel consumption and emissions. These trends will prove to be very valuable in feedstock studies and for predicting future fuel performance in a search for a biodiesel that performs similarly to ULSD. However, there existed some trends that were not completely verified due to system limitations such as the effects of fuel CN on BSFC, NO, and CO_2 and the effect of bulk modulus on injection timing. For these reasons, it became necessary to construct an in-cylinder pressure recording system in order to analyze the effects of fuel properties on injection timing and combustion phasing.

The construction of this system required equipment specifically designed for the relatively harsh engine cylinder environment and rapid sampling speed. Using the proper Kistler pressure transducer and engine crankshaft encoder, pressure measurements are sent to a dedicated computer utilizing National Instruments hardware and software custom-programmed to measure, analyze, and record the pressure and crank angle signals. The operational cylinder-pressure system was verified by testing ULSD, Used Cooking Oil biodiesel, and Jet Propellant number 8 fuels. The resulting pressure profiles for each fuel were used in conjunction with measurements of engine fuel consumption, power, and exhaust emissions in order to analyze trends based on fuel properties. The results of Chapter 3 were found to be in agreement with expected trends established in the literature for mechanical and combustion efficiency, start of combustion, and ignition delay. These findings validated the accuracy, practicality, and importance of the in-cylinder pressure system. The ambiguity of the findings of Chapter 2 with respect to biodiesel fuel properties such as Cetane Number, rate of heat release, and start of combustion are better understood when utilizing by this in-cylinder pressure system. As a result, future works expanding on the biodiesel research of Chapter 2 will be much stronger as more definitive results will be found.

This system will be a vital instrument in upcoming studies and improvements to the biodiesel test cell. For instance, there will be a study to investigate how different cylinder pressure referencing techniques might result in different values for indicated engine performance parameters. In addition, the system will become an integral part of the upcoming dynamic injection timing system, as the pressure profile and combustion phasing will be important factors to consider when making injection timing changes. Furthermore, as additional engine test cells come on-line, plans exist for additional in-cylinder pressure systems to be installed on these engines. The knowledge gained with respect to the equipment, software programming, and fuel characteristics will prove to be essential for the successful implementation of these systems. It is the hope of this author that the knowledge shared here will be used as a foundation upon which future graduate students build their research with fuels and engine technology.

3.5 Acknowledgments

It was the guidance of Dr. Christopher Depcik of Mechanical Engineering and the financial support of the University of Kansas Transportation Research Institute that made this work possible. Furthermore, measurements of emissions were completed with the assistance of Dr. Edward Peltier and Yue Zhong of Civil, Environmental, and Architectural Engineering and fuel analysis was performed by Andrew Duncan of Chemical and Petroleum Engineering. Additional assistance included efforts by Eric Cecrle and J. C. Ragone of Mechanical Engineering.

References

1. Heywood, J.B., *Internal combustion engine fundamentals.* 1988.
2. McCormick, R., et al., *Impact of biodiesel source material and chemical structure on emissions of criteria pollutants from a heavy-duty engine.* Environ. Sci. Technol, 2001. **35**(9): p. 1742-1747.
3. Boehman, A., et al., *The impact of the bulk modulus of diesel fuels on fuel injection timing.* Energy Fuels, 2004. **18**(6): p. 1877-1882.
4. Graboski, M.S. and R.L. McCormick, *Combustion of fat and vegetable oil derived fuels in diesel engines.* Progress in Energy and Combustion Science, 1998. **24**(2): p. 125-164.
5. McCormick, R.L., et al., *Fuel additive and blending approaches to reducing NOx emissions from biodiesel.* SAE Tech. Pap, 2002(2002-01): p. 1658.
6. Tyson, K.S., et al., *Biodiesel handling and use guidelines.* 2006.
7. *Alternatives to Traditional Transportation Fuels 2008.* Energy Information and Administration: Washington, D.C.
8. *International Energy Outlook 2010.* DOE/EIA; Energy Information and Administration: Washington, D.C.
9. Knothe, G., et al., *The biodiesel handbook*. 2005: AOCS press Champaign, IL.
10. Brunt, D.M. and C.R. Pond, *Evaluation of techniques for absolute cylinder pressure correction.* 1997.
11. Randolph, A.L., *Methods of processing cylinder-pressure transducer signals to maximize data accuracy*. 1990, Society of Automotive Engineers, 400 Commonwealth Dr, Warrendale, PA, 15096, USA.
12. Benjumea, P., J. Agudelo, and A. Agudelo, *Effect of the Degree of Unsaturation of Biodiesel Fuels on Engine Performance, Combustion Characteristics, and Emissions.* Energy & Fuels: p. 125-164.
13. Nam, G., et al., *The effect of an external fuel injection on the control of LNT system; the diesel NOx reduction system.* 2007.
14. *Summary of Current and Historical Light-Duty Vehicle Emission Standards.* United States Environmental Protection Agency - Office of Transportation and Air Quality. **April 2007**: p. http://www.epa.gov/greenvehicles/detailedchart.pdf.
15. Cecrle, E.D., *Controls and Measurements of KU Engine Test Cells for Biodiesel, SynGas, and Assisted Biodiesel Combustion*, in *Mechanical Engineering*. 2011, University of Kansas: Lawrence, Kansas. p. 146.
16. Moran, T., *THE LOGISTICS BATTLE: US WAGES A ONE-FUEL WAR.* Automotive News, 2003. **77**(6031): p. 42.
17. Mueller, C., A. Boehman, and G. Martin, *An Experimental Investigation of the Origin of Increased NOx Emissions When Fueling a Heavy-Duty Compression-Ignition Engine with Soy Biodiesel.* SAE International Journal of Fuels and Lubricants, 2009. **2**(1): p. 789.
18. Le Pera, M., *The reality of the single-fuel concept.* Army Logistician, 2005. **37**(2): p. 41-43.
19. Balat, M., *Potential alternatives to edible oils for biodiesel production-A review of current work.* Energy Conversion and Management, 2010.
20. Pinto, A., et al., *Biodiesel: an overview.* Journal of the Brazilian Chemical Society, 2005. **16**: p. 1313-1330.
21. Duncan, A., et al., *High-Pressure Viscosity of Biodiesel from Soybean, Canola, and Coconut Oils.* Energy & Fuels: p. 125-164.
22. Adi, G., et al., *Soy-Biodiesel Impact on NO x Emissions and Fuel Economy for Diffusion-Dominated Combustion in a Turbo- Diesel Engine Incorporating Exhaust Gas Recirculation and Common Rail Fuel Injection.* Energy & Fuels, 2009. **23**(12): p. 5821-5829.

23. Knothe, G., *"Designer" Biodiesel: Optimizing Fatty Ester Composition to Improve Fuel Properties†.* Energy & Fuels, 2008. **22**(2): p. 1358-1364.
24. McCormick, R., et al., *Effects of biodiesel blends on vehicle emissions.* Milestone Report. National Renewable Energy Laboratory, NREL/MP-540-40554, 2006.
25. Enweremadu, C. and H. Rutto, *Combustion, emission and engine performance characteristics of used cooking oil biodiesel--A review.* Renewable and Sustainable Energy Reviews, 2010.
26. Ban-Weiss, G., et al., *A numerical investigation into the anomalous slight NOx increase when burning biodiesel; a new (old) theory.* Fuel Processing Technology, 2007. **88**(7): p. 659-667.
27. Ye, P. and A.L. Boehman, *Investigation of the Impact of Engine Injection Strategy on the Biodiesel NOx Effect with a Common-Rail Turbocharged Direct Injection Diesel Engine.* Energy & Fuels, 2010. **24**: p. 4215-4225.
28. United States Environmental Protection Agency, *A Comprehensive Analysis of Biodiesel Impacts on Exhaust Emissions*. 2002, Assessment and Standard Division, Office of Transportation and Air Quality, USEPA: Washington, DC.
29. Perry, R. and D. Siebers, *Rapid reduction of nitrogen oxides in exhaust gas streams.* 1986.
30. Zhang, Y. and A.L. Boehman, *Impact of biodiesel on NO x emissions in a common rail direct injection diesel engine.* Energy & fuels, 2007. **21**(4): p. 2003-2012.
31. Szybist, J.P., et al., *Evaluation of formulation strategies to eliminate the biodiesel NOx effect.* Fuel Processing Technology, 2005. **86**(10): p. 1109-1126.
32. Monyem, A., J.H. Van Gerpen, and M. Canacki, *The Effect of Timing and Oxidation on Emissions from Biodiesel-fueled Engines.* Transactions of the ASAE, 2001. **44**: p. 35-42.
33. Garner, S., R. Sivaramakrishnan, and K. Brezinsky, *The high-pressure pyrolysis of saturated and unsaturated C7 hydrocarbons.* Proceedings of the Combustion Institute, 2009. **32**(1): p. 461-467.
34. Garner, S. and K. Brezinsky, *Biologically derived diesel fuel and NO formaiton: An experimental and chemical kinetic study, Part 1.* Combustion and Flame, 2011. **158**: p. 2289-2301.
35. Agarwal, A. and L. Das, *Biodiesel development and characterization for use as a fuel in compression ignition engines.* Journal of engineering for gas turbines and power, 2001. **123**: p. 440.
36. Knothe, G., *Dependence of biodiesel fuel properties on the structure of fatty acid alkyl esters.* Fuel Processing Technology, 2005. **86**(10): p. 1059-1070.
37. Girard, J., et al., *Technical advantages of vanadium SCR systems for diesel NOx control in emerging markets.* SAE International Journal of Fuels and Lubricants, 2009. **1**(1): p. 488.
38. García, M., et al., *Prediction of normalized biodiesel properties by simulation of multiple feedstock blends.* Bioresource technology, 2010. **101**(12): p. 4431-4439.
39. Ramos, M.J., et al., *Influence of fatty acid composition of raw materials on biodiesel properties.* Bioresource technology, 2009. **100**(1): p. 261-268.
40. Lapuerta, M., J. Rodríguez-Fernández, and O. Armas, *Correlation for the estimation of the density of fatty acid esters fuels and its implications. A proposed Biodiesel Cetane Index.* Chemistry and physics of lipids, 2010. **163**(7): p. 720-727.
41. *Standard Specification for Diesel Fuel Oils.* ASTM International Specification: ASTM D975-10c, 2010.
42. Anslyn, E.V. and D.A. Dougherty, *Modern Physical Organic Chemistry*. 2006, Sausalito, CA: University Science Books.
43. Harrington, K., *Chemical and physical properties of vegetable oil esters and their effect on diesel fuel performance.* Biomass, 1986. **9**(1): p. 1-17.
44. Plint, M. and A. Martyr, *Engine testing: theory and practice*. 2007, Elsevier Ltd.: Burlington, MA. p. 442.
45. *Bosch Automotive Handbook*. 8th ed. 2011, Plochingen, Germany: Bosch, R.

46. Kreyszig, E., *Advanced Engineering Mathematics*. 10 ed. 2011, Hoboken, NJ: John Wiley & Sons, Inc. 1113.
47. Wadumesthrige, K., et al., *Performance, Durability, and Stability of a Power Generator Fueled with ULSD, S-8, JP-8, and Biodiesel.* SAE Technical Paper, 2010: p. 01-0636.
48. Depcik, C., et al., *Instructional use of a single-zone, premixed charge, spark-ignition engine heat release simulation.* International Journal of Mechanical Engineering Education, 2007. **35**(1): p. 1-31.
49. Ireland, J., et al., *Improving Biodiesel Emissions and Fuel Efficiency with Fuel-Specific Engine Calibration.* SAE Technical Paper, 2009: p. 01-0492.
50. Korres, D.M., et al., *Aviation fuel JP-5 and biodiesel on a diesel engine.* Fuel, 2008. **87**(1): p. 70-78.
51. Tiron, R., *$400 per gallon gas to drive debate over cost of war in Afghanistan.* The Hill.
52. Fernandes, G., et al., *Impact of military JP-8 fuel on heavy-duty diesel engine performance and emissions.* Proceedings of the Institution of Mechanical Engineers, Part D: Journal of Automobile Engineering, 2007. **221**(8): p. 957.
53. Topal, M.H., et al., *PAH and other emissions from burning of JP-8 and diesel fuels in diffusion flames.* Fuel, 2004. **83**(17-18): p. 2357-2368.